

Expanding Computational Infrastructure:

The First 5 Years of CIG



1200 E. California Blvd., 252-12,
Pasadena, CA 91125
(626) 395-1699
Fax (626) 296-9080

CIG is supported by the U.S. National Science Foundation



The content herein is based upon work supported by the National Science Foundation under Grant No. EAR-0406751. Any opinions, findings, and conclusions or recommendations expressed in this material are those of the authors and do not necessarily reflect the views of the National Science Foundation.

Table of Contents

Part A: CIG Abstracts

Computational Seismology

Bozdag, E. and J. Trampert, Testing seismic tomography models using numerical simulation of wave propagation.....	9
Carrington, L., D. Komatitsch, M. Laurenzano, M.M. Tikir, D. Michéa, N. Le Goff, A. Snively, and J. Tromp, High-Frequency Simulations of Global Seismic Wave Propagation Using SPECFEM3D_GLOBE.....	10
Chen, M., et al., Adjoint Tomography of the 3D Seismic Velocity Structure in the Japan Subduction Zone.....	11
Kirkby, A., and P. Cummins, Evaluating the effectiveness of current 3-D earth models for use in rapid earthquake source characterisation.....	12
Lee, S.J., H.W. Chen, Q. Liu, D. Komatitsch, B.S. Huang, and J. Tromp, Three-Dimensional Simulations of Seismic-Wave Propagation in the Taipei Basin with Realistic Topography Based upon the Spectral-Element Method.....	13
Liu, Q., C. Tape, A. Maggi, and J. Tromp, Automatic 3D Moment-tensor Inversions for Southern California Earthquakes.....	14
Maggi, A., C. Tape, M. Chen, D. Chao, and J. Tromp, An automated time-window selection algorithm for seismic tomography.....	15
Martin, R., and D. Komatitsch, An unsplit convolutional Perfectly Matched Layer improved at grazing incidence for the seismic wave equation.....	16
Martin, R., D. Komatitsch, and J. Labarta, Simulation of seismic wave propagation in a 3D asteroid model using an unstructured MPI spectral-element method and non-blocking communications.....	17
Mikesell, D., K. van Wijk, A. Calvert, and M. Haney, The virtual refraction: Useful spurious energy in seismic interferometry.....	18
Peter, D., A. Rodgers, B. Savage, and J. Tromp, Adjoint tomography for the Middle East.....	19
Ruan, Y. and Y. Zhou, Investigating the effects of 3-D anelasticity (Q) structure in global surface-wave propagation using the Spectral Element Method (SEM).....	20
Tape, C., Q. Liu, A. Maggi, and J. Tromp, Adjoint tomography of the southern California crust.....	21

Geodynamo

Driscoll, P., and P. Olson, Geodynamo Models with Core Evolution.....	22
Olson, P., P. Driscoll, and H. Amit, Dipole collapse and reversal precursors in a numerical dynamo.....	23

Long-Term Tectonics

Choi, E., and R. Buck, Reproducing Observed Fault Statistics in 3D Numerical Models.....	24
Duclaux, G., and T. Rawling, Application of Long-term Tectonic Simulations to Predictive Mineral Exploration.....	25

Fay, N., Mantle flow and crustal dynamics in southern California and the Pacific Northwest	26
Harry, D.L., Geodynamic Models of Extension in West Antarctica	27
Harry, D.L., Geodynamic Models of Opening of the Gulf of Mexico	28
Ito, G. and M. Behn, 3-D Faulting and Magmatism at Mid-Ocean Ridges	29
O'Dwyer Brown, L., L.H. Kellogg, and C.E. Lesher, Numerical Simulations of High Pressure Falling Sphere Experiments	30
Quenette, S., and L. Moresi, Collaborative Code Development with CIG: AuScope Simulation & Modelling Victoria – Monash University and VPAC.....	31
Lev, E., and B.H. Hager, The effect of anisotropic viscosity on mantle dynamics	32
Rey, P., and R.D. Müller, Active Plate Margin Fragmentation: Some Ellipsis Experiments....	33
Rey, P., C. Teyssier, and D.L. Whitney, Extension Rates, Crustal Melting, and Core Complex Dynamics	34
Rey, P., C. Teyssier, and D.L. Whitney, The Fate of Continental Slabs	35
Rey, P., C. Teyssier, and D.L. Whitney, How far can the plateau lower crust flow? Ask Ellipsis!	36
Sheehan, J., B. O'Reilly, and D. Sokoutis, A comparison between lithospheric scale numerical and analogue models.....	37
Stark, C., E. Choi, and M. Convertino, 3D simulation of landslide failure and incipient runout	38

Magma Dynamics

Montési, L.G.J., MultiMaDDS – Implementing Magma dynamics with the commercial software COMSOL Multiphysics[tm]	39
Quenette, S., M. Spiegelman, and D. Lee, The development of stgMaDDS – the Magma Dynamics Demonstration Suite on StGermain	40
Spiegelman, M., P. van Keken, and B. Hacker, ArcFlow: Advanced models of fluid flow in subduction zones	41
Spiegelman, M., MADDs-FP – Flexible multi-physics models for Magma Dynamics using advanced computational libraries.....	42

Mantle Convection

Ballmer, M., J. van Hunen, G. Ito, P.J. Tackley, and T.A. Bianco, Small-scale sublithospheric convection, a mechanism for non-hotspot volcanism	44
Bianco, T., G. Ito, J. van Hunen, M. Ballmer, and J. Mahoney, Geochemical variations at intraplate hotspots caused by variable melting of a veined mantle plume.....	45
Bower, D.J., M. Gurnis, J.M. Jackson, and W. Sturhahn, Enhanced Convection and Fast Plumes in the Lower Mantle Induced by the Spin Transition in Ferropericlase.....	47
Bull, A., A. McNamara, and J. Ritsema, Synthetic tomography of plume clusters and thermochemical piles.....	48
Burkett, E., and M. Billen, 2D Dynamics of Slab Detachment Due to Ridge-Trench Collision	49
Conrad, C., and M. Behn, Global Mantle Flow and the Development of Seismic Anisotropy.	50
Conrad, C., and L. Husson, Influence of Dynamic Topography on Sea Level and its Rate of Change	51
Conrad, C., and C. Lithgow-Bertelloni, Influence of Continental Roots and Asthenosphere on Plate-Mantle Coupling	52

DiCaprio, L., M. Gurnis, R.D. Müller, and E. Tan, History of the Australian region since the Cretaceous: Assimilating plate tectonic data into a regionally-globally coupled geodynamic model	53
Foley, B.J., and T.W. Becker, Generation of Plate Tectonics and Mantle Heterogeneity from a Spherical, Visco-plastic Convection Model.....	54
Garnero, E., T. Lay, and A. McNamara, Implications of lower mantle structural heterogeneity for existence and nature of whole mantle plumes	55
Ghosh, A., T. Becker, and S. Zhong, Effect of lateral viscosity variations on mantle flow and the geoid	56
Höink, T., and A. Lenardic, Three-dimensional mantle convection simulations with a low-viscosity asthenosphere	57
Jadamec, M., and M. Billen, Mantle Flow at a Subduction-Transform Plate Boundary.....	58
King, S.D., More Thoughts on Tharsis Rise Mars and Small-Scale Convection.....	59
King, S.D., Unusual Pattern of Convection in a Thin Mantle Shell and the Connection to Tectonics on Mercury	60
Liu, L., and M. Gurnis, Simultaneous inversion of mantle properties and initial conditions using an adjoint of mantle convection.....	61
Liu, L., S. Spasojevic, and M. Gurnis, Reconstructing Farallon Plate Subduction beneath North America back to the Late Cretaceous.....	62
Manea, V., and M. Gurnis, Reconstructing of Flat Slab Subduction and Detachment beneath Central Mexico	63
Métivier, L., and C. Conrad, Body Tides of a Convecting, Laterally Heterogeneous, and Aspherical Earth.....	64
Roberts, J.H., R.J. Lillis, and M. Manga, Giant impacts on early Mars and the cessation of the Martian dynamo	65
Spasojević, S., L. Liu, and M. Gurnis, North America regional sea level since the Late Cretaceous from adjoint convection models	66
Spasojević, S., M. Gurnis, and R. Sutherland, Inference of mantle properties with an evolving dynamics model of the Antarctica-New Zealand region.....	67
Tan, E., W. Leng, S. Zhong, and M. Gurnis, The convection planform of a dense chemical layer with higher bulk modulus	68
Zhong, S.J., Migration of Tharsis volcanism on Mars caused by differential rotation of the lithosphere.....	69
Zhong, S.J. and W. Leng, Constraints on thermochemical convection of the mantle from plume heat flux, plume excess temperature and upper mantle temperature.....	70
Zhong, S.J., Z.X. Li, and J.H. Roberts, Very Long-wavelength Convection, True Polar Wander and Supercontinent Cycles	71

Short-Term Crustal Dynamics

Buck, W.R., and S. Nooner, Post-rifting relaxation at a subaerial spreading center.....	72
Currenti, G., C. Del Negro, G. Ganci, and C.A. Williams, Modeling of Coulomb Stress Changes During the 2002-03 Etna Eruption	73
Freed, A., T. Ali, and J. Freymueller, Contemporary strain and stressing rates across Alaska from interseismic and postseismic processes.....	74

Hsu, Y-J., M. Simons, C. Williams, and E. Casarotti, 3-D FEM derived elastic Green's functions for the coseismic deformation of the 2005 Mw 8.7 Nias-Simeuleu, Sumatra earthquake	75
Lohman, R., and C. Williams, Assessing the effects of rigidity contrasts on earthquake source inversions using PyLith.....	76
Lü, J., C.W. Gable, C.A. Williams, and B.H. Hager, Effects of 3-D Variations in Fault Geometry and Slastic Structure on Geodetic Velocities, Ventura Basin Region, CA.....	77
Scandura, D., G. Currenti, and C. Del Negro, Viscoelastic Modeling of Ground Deformation During the 1993-97 Inflation Period at Etna Volcano	78
Williams, C., C.W. Gable, B.H. Hager, B.J. Meade, B. Aagaard, and M. Knepley, Modeling of Multiple Earthquake Cycles in Southern California Using the SCEC Community Fault Model.....	79

Part B: CIG Software

Section I: Infrastructure

Software Policies	83
CIG Web Site	84
Buildbot.....	85
Cigma.....	86

Section II: CIG Software Packages

CitcomS.....	87
Gale.....	89
PyLith	91
SPECFEM3D_GLOBE	93
SPECFEM3D.....	94
CIG Seismology Web Portal	96
Other Software Maintained by CIG	98

Part C: CIG Workshops 103

Part D: Governance 111

Part E: Publications and Abstracts Resulting from CIG 119

Part A: CIG Abstracts

The following abstracts each describe an exciting piece of science that has been enabled by CIG or is contributing to the overall CIG effort.

Testing seismic tomography models using numerical simulation of wave propagation

Ebru Bozdağ & Jeannot Trampert

Department of Earth Sciences, Utrecht University, Utrecht, the Netherlands

It is very well known that Earth's crust has a very strong influence on surface waves. Therefore, crustal corrections are a crucial step in surface wave tomography to enhance mantle structures. In Bozdağ & Trampert [2008], we investigated crustal effects on tomographic mantle images. We estimated crustal corrections using first order ray theoretical and finite frequency approximations and compared them to those obtained from full 3-D wave simulations with the spectral element method. We observed that crustal effects cannot be completely removed from seismograms and produce errors larger than those in phase velocity measurements at periods shorter than 60 and 80 s for Rayleigh and Love waves, respectively. In addition, Rayleigh and Love waves are affected by the crust in a different way. As a consequence, our observations indicate that imperfect crustal corrections could have a large impact on inferences of radial mantle anisotropy. Part of mantle anisotropy could be uncorrected crustal signal. Possible solutions are to use 3-D reference models or to invert crust and mantle together instead of applying crustal corrections.

In Bozdağ & Trampert [2009], we investigated to what extent current tomographic mantle images represent the real Earth's mantle. For this purpose, we compared real seismograms to those computed by the spectral element method in some 3-D mantle models. In particular, we examined the effect of damping on our interpretation of the mantle by choosing differently damped mantle models. Surprisingly, synthetic seismograms are statistically insensitive to differently damped models. These observations point to a crustal signal which could not be properly removed from the data by corrections. In addition, we observed a large amplitude signal which is usually ignored in classical mantle tomography. The amplitude mismatches are most likely due to our ignorance in attenuation. Body wave amplitudes however are more sensitive to focusing/defocusing effects than surface waves.

The computation of synthetic seismograms in these studies was performed by SPEC-FEM3D_GLOBE package that we obtained from CIG.

References

- Bozdağ, E. and J. Trampert (2008), On crustal corrections in surface wave tomography, *Geophysical Journal International*, 172, 1066-1082.
- Bozdağ, E. and J. Trampert (2009), Assessment of tomographic mantle models using spectral element seismograms, *Geophysical Journal International*, under revision.

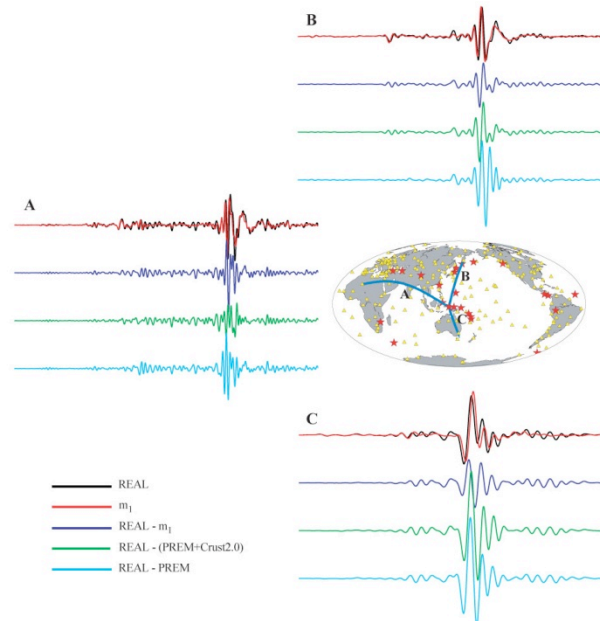


Figure An example for comparison of real seismograms with the synthetic ones computed in 1D (PREM) and 3D crust (Crust2.0) and mantle (m_1) models by SPEC-FEM3D. Blue, green and cyan seismograms show the waveform differences.

High-Frequency Simulations of Global Seismic Wave Propagation Using SPECFEM3D_GLOBE

Laura Carrington^a, Dimitri Komatitsch^{b,c}, Michael Laurenzano^a, Mustafa M Tikir^a, David Michéa^b, Nicolas Le Goff^b, Allan Snively^a, Jeroen Tromp^d

^a Performance Modeling and Characterization Lab, San Diego Supercomputer Center, La Jolla, CA, USA

^b University of Pau, France

^c Institut universitaire de France, Paris, France

^d Seismological Laboratory, California Institute of Technology, Pasadena, CA, USA

SPECFEM3D_GLOBE is a spectral-element application enabling the simulation of global seismic wave propagation in 3D anelastic, anisotropic, rotating and self-gravitating Earth models at unprecedented resolution. A fundamental challenge in global seismology is to model the propagation of waves with periods between 1 and 2 seconds, the highest frequency signals that can propagate clear across the Earth. These waves help reveal the 3D structure of the Earth's deep interior and can be compared to seismographic recordings. We broke the 2 second barrier using the 62K processor Ranger system at TACC. Indeed we broke the barrier using just half of Ranger, by reaching a period of 1.84 seconds with sustained 28.7 Tflops on 32K processors. We obtained similar results on the XT4 Franklin system at NERSC and the XT4 Kraken system at University of Tennessee Knoxville, while a similar run on the 28K processor Jaguar system at ORNL, which has more memory per processor, sustained 35.7 Tflops (a higher flops rate) with a 1.94 shortest period. For the final run we obtained access to the ORNL Petaflop System, a new very large XT5 just coming online, and achieved 1.72 shortest period and 161 Tflops using 149,784 cores.

With this landmark calculation we have enabled a powerful new tool for seismic wave simulation, one that operates in the same frequency regimes as nature; in seismology there is no need to pursue periods much smaller because higher frequency signals do not propagate across the entire globe.

We employed performance modeling methods to identify performance bottlenecks and worked through issues of parallel I/O and scalability. Improved mesh design and numbering results in excellent load balancing and few cache misses. The primary achievements are not just the scalability and high teraflops number, but a historic step towards understanding the physics and chemistry of the Earth's interior at unprecedented resolution.

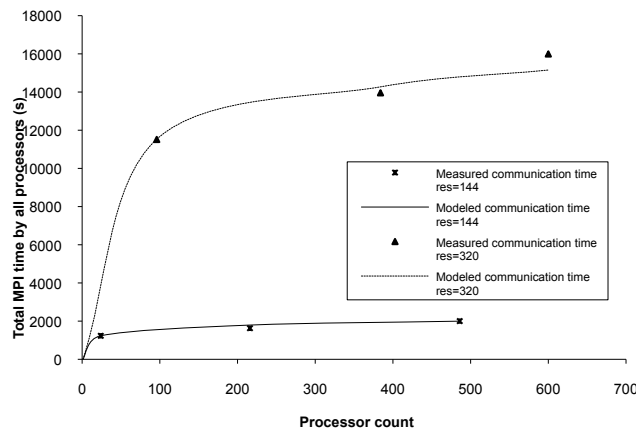


Figure: Fitted curves for total communication time (in seconds) for all cores for different resolutions.

Adjoint Tomography of the 3D Seismic Velocity Structure in the Japan Subduction Zone

Min Chen¹, Qinya Liu², Alessia Maggi³, Jeroen Tromp⁴, Robert van der Hilst¹, Hiroo Kanamori⁵, Takuto Maeda⁶, and Kazushige Obara⁶

¹ Department of Earth, Atmospheric, and Planetary Sciences, Massachusetts Institute of Technology, Cambridge, MA, USA

² Department of Physics, University of Toronto, Ontario, Canada

³ CNRS (UMR 7516) and Université Louis Pasteur, Strasbourg, France

⁴ Department of Geosciences, Princeton University, Princeton, NJ, USA

⁵ Seismological Laboratory, California Institute of Technology, Pasadena, CA, USA

⁶ NIED, National Research Institute for Earth Science and Disaster Prevention, Tsukuba, Ibaraki, Japan

Both forward modeling and adjoint tomography techniques based on spectral-element method (SEM) are used to investigate the 3D velocity structure in the Japan subduction zone. From our previous study (Chen et al., 2007), a very low velocity layer (LVL) on top of the slab beneath NE Japan has been revealed and modeled using complex waveforms. LVL plays a very important role in subduction zone water transportation and the dynamic evolution of the slab. However it's still unclear whether the LVL is a general feature in the entire subduction zone, which can only be resolved by high-resolution seismic tomographic images. Adjoint tomography technique is an effective tool for using 3-D models as initial models and refining them by iteratively minimizing the misfit between synthetics and data (Tromp et al., 2005). For more detailed images of the mantle beneath Japan we can exploit the dense data coverage provided by a total of 818 stations and 206 earthquakes (Figure 1). According to finite-frequency theory, the sensitive region along the ray path is given by a 3-D ‘banana-doughnut’ kernel. The weighted sums of the banana-doughnut kernels for all event-station pairs, with weights determined by the traveltimes measurements, are used to construct misfit kernels (Figure 2). These gradients are then used in a non-linear conjugate gradient algorithm to further improve the existing 3-D models.

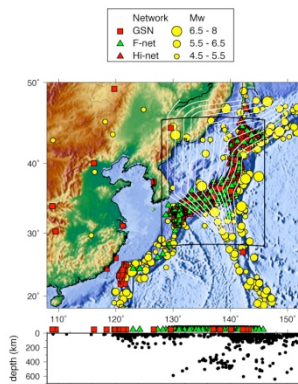
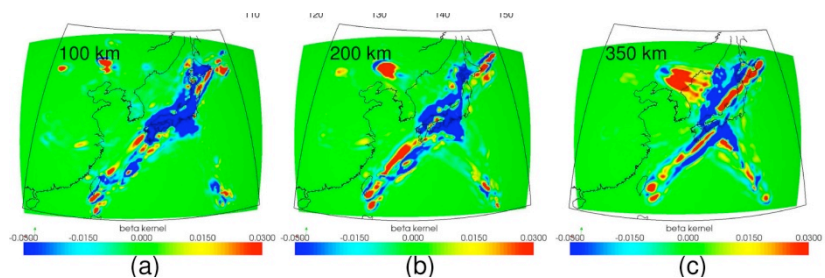


Figure 1: Map of the event and station distribution in the study area. 206 events occurring between 2000 and 2006 with M_w in the range of 4.5–8 (yellow circles) are selected for tomographic inversion. There are a total of 818 stations from three different networks located in this area: GSN (red squares), F-net (green triangles), and Hi-net (red triangles), amongst which GSN and F-net provide broadband records, whereas Hi-net only provides high-frequency records. The bottom plot shows the distribution of all the events and stations projected onto a WE striking vertical plane. The region of the high-resolution Japan model is identified by the black box on the map. Inside the box, the white lines indicate the contours of the upper boundary of the Pacific plate with a 50 km contour interval.

Figure 2: Map view of the spherical cross-sections of the misfit kernels, summation of 206 event kernels, for shear-wave velocity (β) at depths of (a) 100 km, (b) 200 km, and (c) 350 km. The spatial distribution of these 206 events is shown in Figure 1.



References

- Chen, M., J. Tromp, D. Helmberger, and H. Kanamori (2007), Waveform modeling of the slab beneath Japan, *J. Geophys. Res.*, *112*, doi:10.1029/2006JB004394.
- Tromp, J., C. H. Tape, and Q. Liu (2005), Seismic tomography, adjoint methods, time reversal, and banana-doughnut kernels, *Geophys. J. Int.*, *160*, 195–216.

Evaluating the effectiveness of current 3-D earth models for use in rapid earthquake source characterisation

Alison Kirkby and Phil Cummins, *Geoscience Australia*

Tsunami warning systems typically use only magnitude and location to identify potentially tsunamigenic earthquakes, but slip distribution may also have an influence if the fault rupture length is comparable to the tsunami propagation distance. For example, the MW 9.3 Sumatra-Andaman earthquake in 2004 had a rupture length of >1200km, so that even coastlines 1000s of km distant from the source could experience tsunami heights sensitive to details of the fault slip. Slip model inversions typically use waveform calculations that only approximately account for 3D structure, and these often involve a minimum distance for their application, delaying the time in which data can be used to produce a slip model. The purpose of this project is to explore whether this distance threshold can be reduced by using seismograms accurately calculated for 3D earth structure. We compared synthetic surface wave seismograms calculated for a point source representation of the 12 September, 2007 Mw=8.5 earthquake off Sumatra using (a) an asymptotic method accounting for 3D structure via a global phase velocity map, and (b) calculations using SPEC-FEM3D via the CIG portal. The calculated waveforms were compared with each other via cross-correlation (Figure 1.).

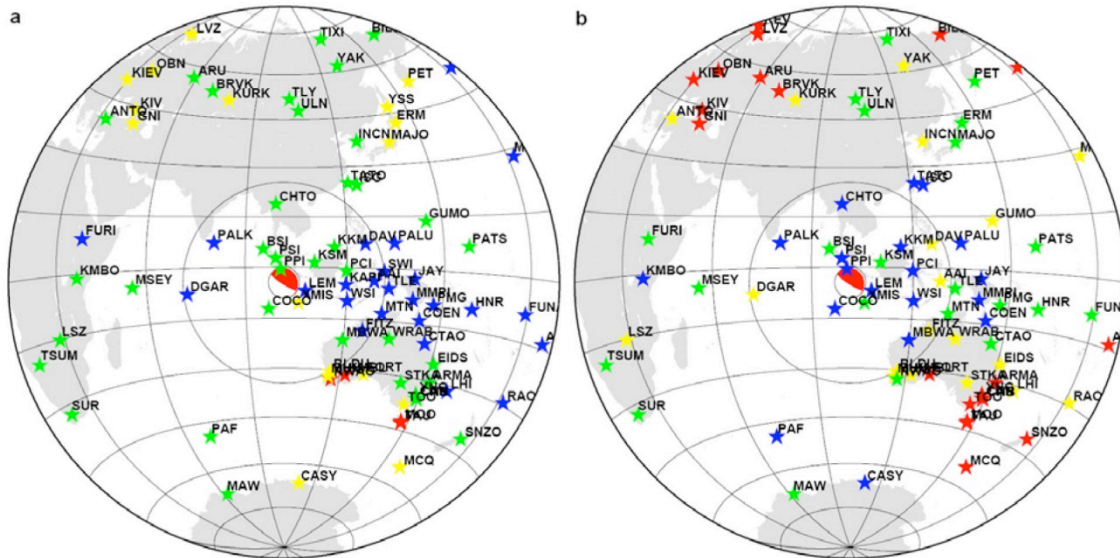


Figure 1. Results of cross correlating point source synthetics from 1D and 3D earth models for the Sumatra event, plotted according to: (a) correlation coefficients (vertical component) of <0.85 (red), 0.85 – 0.90 (yellow), 0.90 – 0.95 (green), 0.95 – 1.00 (blue), (b) correlation coefficients (transverse component).

The results, and similar ones for the 2007 Solomon Islands earthquake, show geographically coherent patterns of low and high correlation. Most of the correlations within the 30° distance threshold, where we expected our use of a phase velocity map might break down, are high. The regions of poorly correlated synthetics are generally at large distance from the source and exhibit some similarity for the two events studied – in particular, some correlations were poor in southern Australia, particularly for the transverse component synthetics.

The results suggest that the effects of 3D structure on the seismic waveform data used for finite fault rupture modelling should be further investigated, especially if its use is to be considered for the Australian stations important for the Australian Tsunami Warning System. Future work will focus on comparing synthetics computed for finite fault models with actual data.

Three-Dimensional Simulations of Seismic-Wave Propagation in the Taipei Basin with Realistic Topography Based upon the Spectral-Element Method

Shiann-Jong Lee¹, How-Wei Chen², Qinya Liu³, Dimitri Komatitsch^{4,5}, Bor-Shouh Huang¹ and Jeroen Tromp⁶

¹ Institute of Earth Sciences, Academia Sinica, Taipei, Taiwan, ROC

² Institute of Geophysics, National Central University, Jung-Li, Taiwan, ROC

³ Seismological Laboratory, California Institute of Technology, Pasadena, California, USA

⁴ Institut universitaire de France, Paris, France

⁵ Department of Modeling and Imaging in Geosciences, CNRS UMR 5212 and INRIA Magique3D, University of Pau, France

⁶ Department of Geosciences, Princeton University, Princeton, USA

We use the spectral-element method to simulate strong ground motion throughout the Taipei metropolitan area. Mesh generation for the Taipei basin poses two main challenges: 1) the basin is surrounded by steep mountains, and 2) the city is located on top of a shallow, low wave-speed sedimentary basin. To accommodate the steep and rapidly varying topography, we introduce a thin high-resolution mesh layer near the surface. The mesh for the shallow sedimentary basin is adjusted to honor its complex geometry and sharp lateral wave-speed contrasts. Variations in Moho thickness beneath Northern Taiwan are also incorporated in the mesh. Spectral-element simulations show that ground motion in the Taipei metropolitan region is strongly affected by the geometry of the basin and the surrounding mountains. The amplification of ground motion is mainly controlled by basin depth and shallow shear-wave speeds, although surface topography also serves to amplify and prolong seismic shaking.

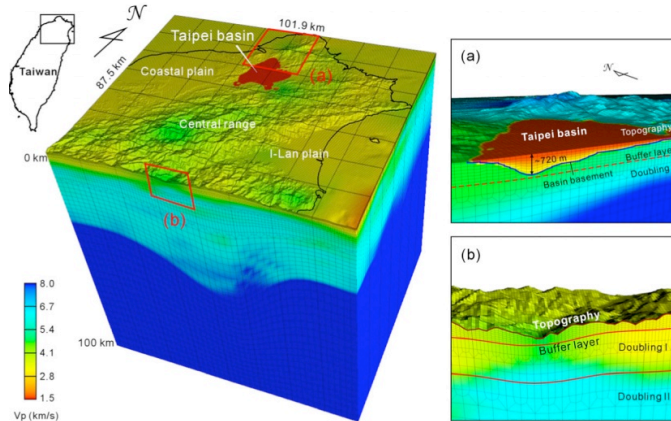


Fig.1 Spectral-element mesh for northern Taiwan. (a) Mesh implementation for the Taipei basin. (b) Mesh that incorporates realistic topography.



Fig.2 3-D SEM simulation and visualization of March 6, 2005 I-lan earthquake doublet. The amplification due to soft materials in the Taipei basin as well as the reflected and refracted waves generated by scattering from the mountains are clearly observed in these visual images.

Reference

Lee, S. J., H. W. Chen, Q. Liu, D. Komatitsch, B. S. Huang, and J. Tromp (2008), Three-dimensional simulations of seismic wave propagation in the Taipei basin with realistic topography based upon the spectral-element method, *Bull. Seism. Soc. Am.*, 98, 253-264, doi:10.1785/0120070033.

Automatic 3D Moment-tensor Inversions for Southern California Earthquakes

Qinya Liu¹, Carl Tape², Alessia Maggi³, and Jeroen Tromp⁴

¹ Department of Physics, University of Toronto, Ontario, Canada

² Seismological Laboratory, California Institute of Technology, Pasadena, California, USA

³ Institut de Physique du Globe, Université de Strasbourg, Strasbourg, France

⁴ Department of Geosciences, Princeton University, Princeton, New Jersey, USA

We present a new source mechanism (moment-tensor and depth) catalog for about 200 recent southern California earthquake with $M_w \geq 3.5$. We carefully select the initial solutions from a few available earthquake catalogs as well as our preliminary 3D moment tensor inversion results. We pick useful data windows by assessing the quality of fits between data and synthetics using an automatic windowing scheme FLEXWIN (Maggi et al., 2008). We compute the source Fréchet derivatives of moment-tensor elements and depth for a recent 3D southern California velocity model inverted based upon finite-frequency event kernels calculated by the adjoint methods and a nonlinear conjugate gradient technique with subspace preconditioning (Tape et al., 2009). We then invert for the source mechanisms and event depths with the 3D CMT inversion techniques introduced by Liu et al. (2004). We assess the quality of this new catalog, as well as other existing ones by computing the 3D synthetics for the updated 3D southern California model. We also plan to implement the moment-tensor inversion methods to automatically determine the source mechanisms for earthquakes with $M_w \geq 3.5$ in southern California.

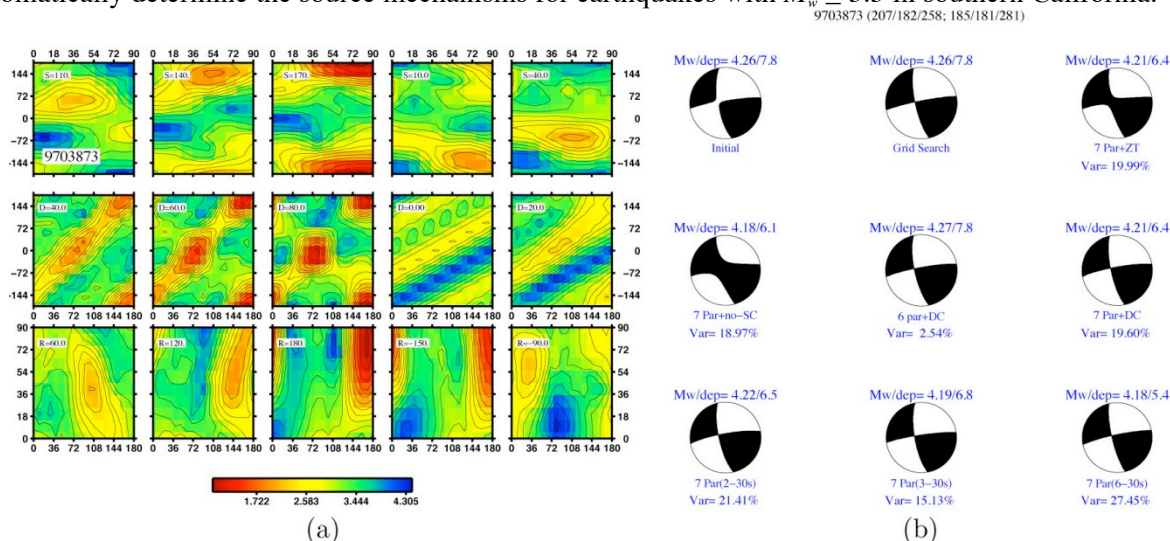


Figure 1: (a) Grid-search the full range of strike, dip and rake for the 2001 Hollywood earthquake to obtain the source mechanism corresponding to the minimum misfit function value, as well as the uncertainties associated with these parameters. (b) Moment-tensor solutions obtained by combinations of different inversion control parameters, including number of source parameters, moment-tensor type, different filter bands, station corrections, etc.

References

- Liu, Q., J. Polet, D. Komatitsch, and J. Tromp (2004), Spectral-element moment tensor inversions for earthquakes in southern California, *Bull. Seism. Soc. Am.*, *94*, 1748–1761.
- Maggi, A., C. Tape, M. Chen, D. Chao, and J. Tromp (2008), An automated data-window selection algorithm for adjoint tomography, *Geophys. J. Int.*, submitted.
- Tape, C., Q. Liu, A. Maggi, and J. Tromp (2009), Adjoint tomography of the southern California crust, *Nature Geoscience*, Submitted.

An automated time-window selection algorithm for seismic tomography

Alessia Maggi¹, Carl Tape², Min Chen³, Daniel Chao², and Jeroen Tromp⁴

¹ Institut de Physique du Globe, Université de Strasbourg, Strasbourg, France

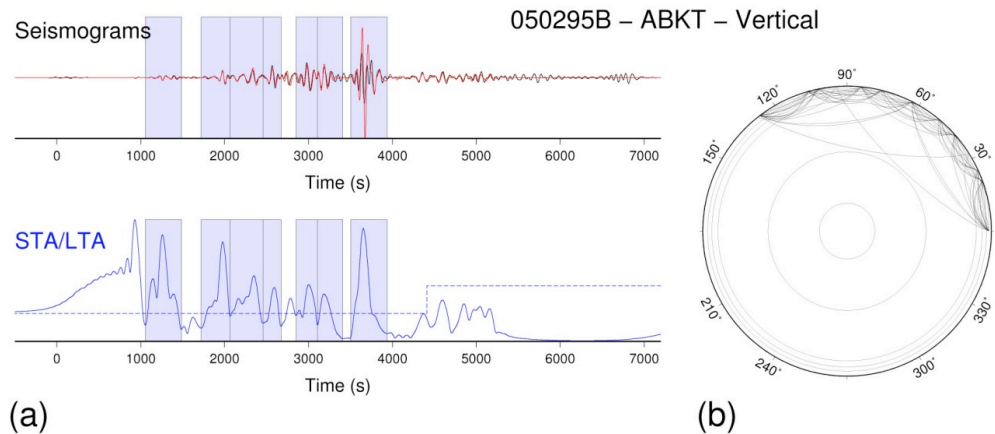
² Seismological Laboratory, California Institute of Technology, Pasadena, CA, USA

³ Department of Earth, Atmospheric and Planetary Sciences, Massachusetts Institute of Technology, Cambridge, MA, USA

⁴ Department of Geosciences, Princeton University, Princeton, NJ, USA

We have developed an open source algorithm FLEXWIN (Maggi et al., 2009) to automatically select time windows on pairs of observed and synthetic seismograms. The algorithm was designed specifically to accommodate synthetic seismograms produced from 3D wavefield simulations such as SPEC-FEM3D (Komatitsch et al., 2002), which capture complex phases that do not necessarily exist in 1D simulations. Our motivation is to use the algorithm for iterative tomographic inversions, in which the synthetic seismograms change from one iteration to the next, and contain more and more 3D-specific phases (Tape et al., 2007). Our strategy is to select time windows on the synthetic seismogram within which the waveform contains a distinct arrival, then require an adequate correspondence between observed and synthetic waveforms within these windows. This selection paradigm is general, and can be applied to synthetic seismograms regardless of how they have been obtained. It is clear, however, that a synthetic seismogram obtained by 3D propagation (using, e.g., SPEC-FEM3D) through a good 3D Earth model will provide a better fit to the observed seismogram over a greater proportion of its length than will be the case for a more approximate synthetic seismogram. In order to isolate changes in amplitude or frequency content potentially associated with distinct seismic arrivals, we have chosen a tool used in automated phase detection for earthquake location, the short-term average / long-term average ratio, and we have adapted it to define time windows around distinct seismic phases (see Figure 1).

Figure 1: Window selection results on the vertical component for an intermediate-depth event in Northern Peru recorded at station ABKT ($\Delta = 127^\circ$). (a) Top: observed and synthetic seismograms (black and red traces); bottom: STA/LTA timeseries. Windows chosen by the algorithm are shown using light blue shading. The phases contained in these windows are: (1) P P, (2) P S + S P, (3) S S, (4) S S S, (5) S S, (6) S 6, (7) fundamental mode Rayleigh wave. (b) Ray paths corresponding to the body-wave phases present in the data windows in (a).



We have successfully applied our windowing algorithm to diverse seismological scenarios: local and near regional tomography in Southern California, regional subduction-zone tomography in Japan, and global tomography (Maggi et al., 2009).

References

- D. Komatitsch, J. Ritsema, and J. Tromp (2002), The spectral-element method, Beowulf computing, and global seismology, *Science*, 298, 1737–1742.
- A. Maggi, C. Tape, M. Chen, D. Chao, and J. Tromp (2009), An automated time-window selection algorithm for seismic tomography, *Geophys. J. Int.*, doi:10.1111/j.1365-246X.2009.04099.x, in press.
- C. Tape, Q. Liu, and J. Tromp (2007), Finite-frequency tomography using adjoint methods—Methodology and examples using membrane surface waves, *Geophys. J. Int.*, 168, 1105–1129.

An unsplit convolutional Perfectly Matched Layer improved at grazing incidence for the seismic wave equation

R. Martin, *University of Pau, France*

D. Komatitsch, *University of Pau, France; Institut universitaire de France, Paris, France*

The Perfectly Matched Layer absorbing boundary condition has proven to be very efficient from a numerical point of view for the elastic wave equation to absorb both body waves with non-grazing incidence and surface waves. However, at grazing incidence the classical discrete Perfectly Matched Layer method suffers from large spurious reflections that make it less efficient for instance in the case of very thin mesh slices, in the case of sources located close to the edge of the mesh, and/or in the case of receivers located at very large offset. We demonstrate how to improve the Perfectly Matched Layer at grazing incidence for the differential seismic wave equation based on an unsplit convolution technique. The improved PML has a cost that is similar in terms of memory storage to that of the classical PML. We illustrate the efficiency of this improved Convolutional Perfectly Matched Layer based on numerical benchmarks using a finite-difference method on a thin mesh slice for an isotropic material and show that results are significantly improved compared with the classical Perfectly Matched Layer technique. We also show that, as the classical model, the technique is intrinsically unstable in the case of some anisotropic materials.

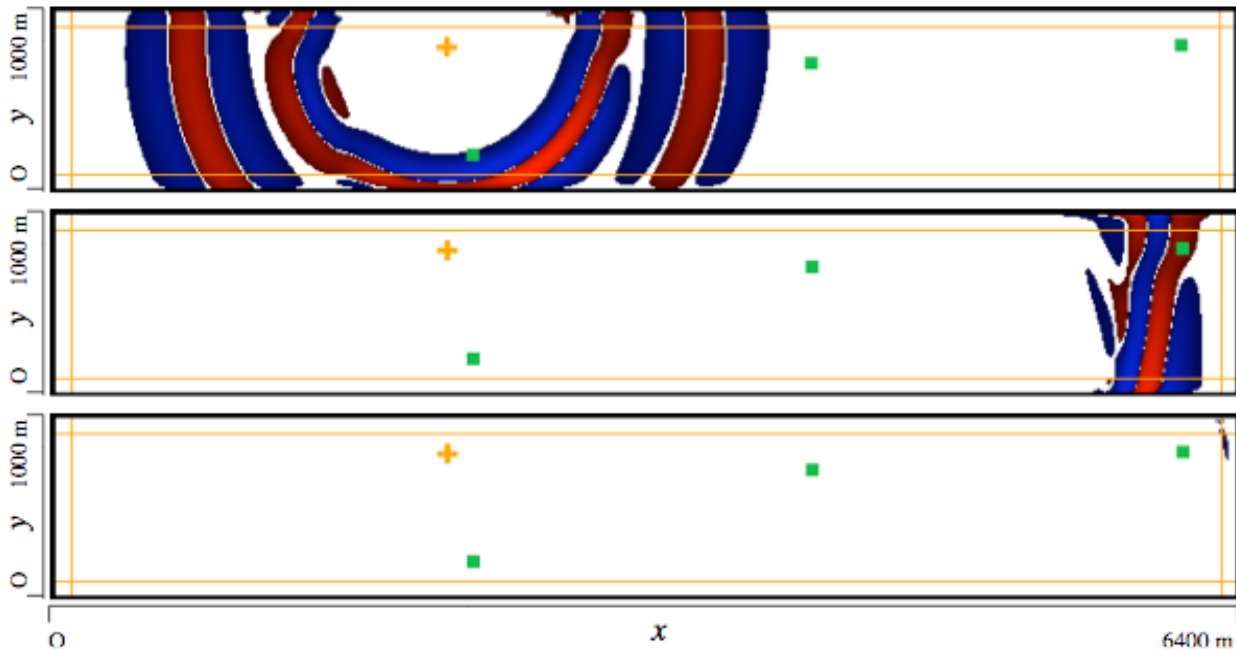


Figure 1: Snapshots in a (x,y) plane of the v_y component of the three-dimensional velocity vector for a model corresponding to a thin slice with C-PML conditions implemented on the six sides. We represent the component in red (positive) or blue (negative) at each grid point. The orange cross indicates the position of the source. The four vertical or horizontal orange lines represent the edge of each layer PML. No spurious wave of significant amplitude is visible, even at grazing incidence.

Simulation of seismic wave propagation in a 3D asteroid model using an unstructured MPI spectral-element method and non-blocking communications

R. Martin, *University of Pau, France*

D. Komatitsch, *University of Pau, France; Institut universitaire de France, Paris, France*

J. Labarta, *Barcelona Supercomputing Center, Spain*

We implement spectral-element calculations in parallel in an asteroid based upon MPI. Homogeneous and fractured models are meshed using the CUBIT mesh generator developed at Sandia National Laboratories (USA) and the unstructured meshes are partitioned using the SCOTCH graph partitioning library, which focuses on balancing the size of the different domains and minimizing the edge cut to optimize load balancing in our parallel non-blocking MPI implementations. Balancing the size of the domains ensures that no processor core remains idle for a significant amount of time while others are still running at each iteration of the time loop, while a small edge cut reduces the number and the size of the communications. Contributions between neighboring elements that are located on different processor cores are added using non-blocking MPI sends and receives. Internal force contributions from the outer elements of a given mesh partition are computed first and sent to the neighbors of that mesh slice using a non-blocking MPI send. Similarly, each processor core issues non-blocking MPI receives. Communications are then overlapped by the calculations.

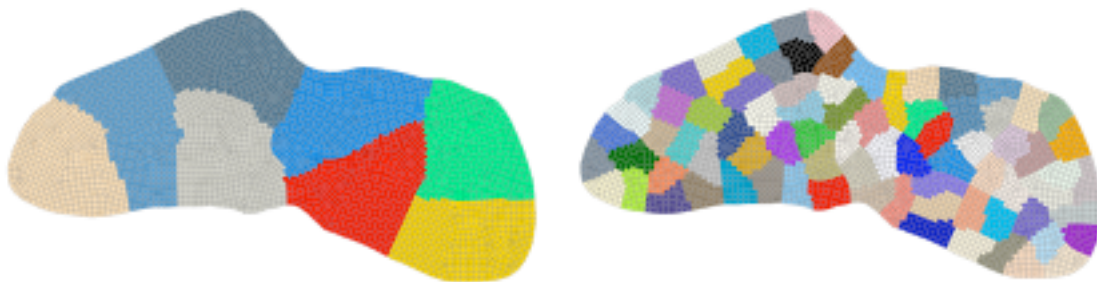


Figure 1: Partitioning of a homogeneous model mesh obtained in the case of 8 (left) and 80 (right) domains. The number of elements along the interface of the partitions is small compared to the number of elements inside each partition in the case of 8 domains and overlapping of communications with calculations works fine. But for 80 domains, this number becomes comparable or even higher than the number of inner elements and overlapping tends to fail with poor performances.

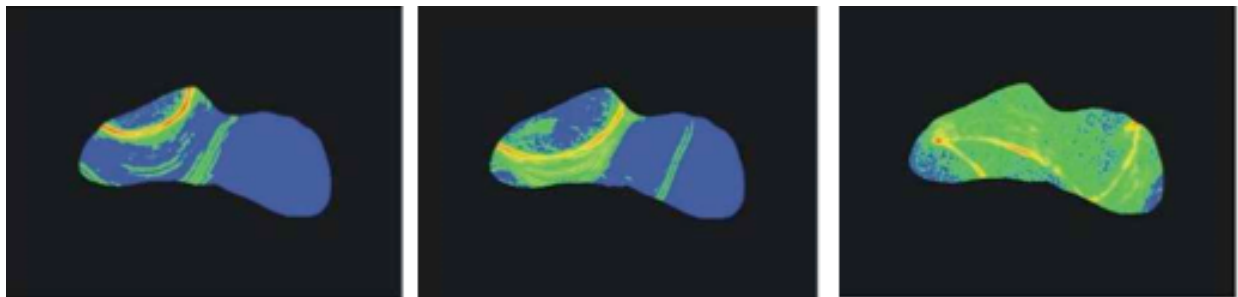


Figure 2: Snapshots of the propagation of simulated 3D seismic waves in the geological model for a total duration of 20 seconds in the case of a 3D asteroid model with a regolith layer. Snapshots are shown at 4-s, 6-s and 15-s on the 3D surface. We represent the vertical component of the displacement vector.

The virtual refraction: Useful spurious energy in seismic interferometry

Dylan Mikesell and Kasper van Wijk, *Physical Acoustics Lab and Department of Geosciences, Boise State University*

Alexander Calvert, *ION - GX Technology, Denver, CO*

Matt Haney, *USGS Alaska Volcano Observatory, Anchorage, AK*

Seismic Interferometry is rapidly becoming an established technique to recover the Green's function between receivers, but practical limitations in the source energy distribution inevitably lead to spurious energy in the results. Instead of attempting to suppress all such energy, we use a spurious wave associated with the crosscorrelation of refracted energy at both receivers to infer estimates of subsurface parameters. We name this spurious event the virtual refraction. Illustrated by a numerical two-layer example, we find that the slope of the virtual refraction defines the velocity of the faster medium and the stationary phase point in the correlation gather provides the critical offset. With the associated critical time derived from the real shot record, this approach includes all the necessary information to estimate wave speeds and interface depth without the need of inferences from other wave types.

Consider the two-layer acoustic model shown in the left of Figure 1. We place an explosive seismic source (with a dominant wavelength of ~ 30 m) at the first receiver location (r_1) and model the wavefield for 0.8 s after the explosion on 101 receivers evenly spaced on a 400 m line, 52 m above the interface. We use the SPECFEM2D seismic wave propagation code to model the wavefield. The middle left panel of Figure 1 shows three coherent events: 1) the direct wave, 2) the reflected wave from the interface, and 3) the refracted wave at offsets greater than 300 m. Now, using seismic interferometry, we attempt to recover the wavefield between two receiver positions based on equation 19 from Wapenaar and Fokkema, which represents the exact acoustic Green's function:

$$\hat{G}(\mathbf{x}_A, \mathbf{x}_B, \omega) + \hat{G}^*(\mathbf{x}_A, \mathbf{x}_B, \omega) = \oint_S \frac{-1}{j\omega\rho(\mathbf{x})} (\hat{G}^*(\mathbf{x}_A, \mathbf{x}, \omega) \partial_i(\hat{G}(\mathbf{x}_B, \mathbf{x}, \omega)) - \partial_i(\hat{G}^*(\mathbf{x}_A, \mathbf{x}, \omega)) \hat{G}(\mathbf{x}_B, \mathbf{x}, \omega)) n_i dS,$$

After summing the crosscorrelations for all sources on the circle in the acoustic model we obtain the virtual shot record shown in the middle right panel of Figure 1. We simplify equation 1 by making a far-field approximation and obtain the wavefield in the right plot of Figure 1. Again we recover the correct direct, reflected, and refracted waves. However, we also observe a spurious linear event traveling at $v_1 = 1750$ m/s going through the origin. We call this spurious wave the virtual refraction.

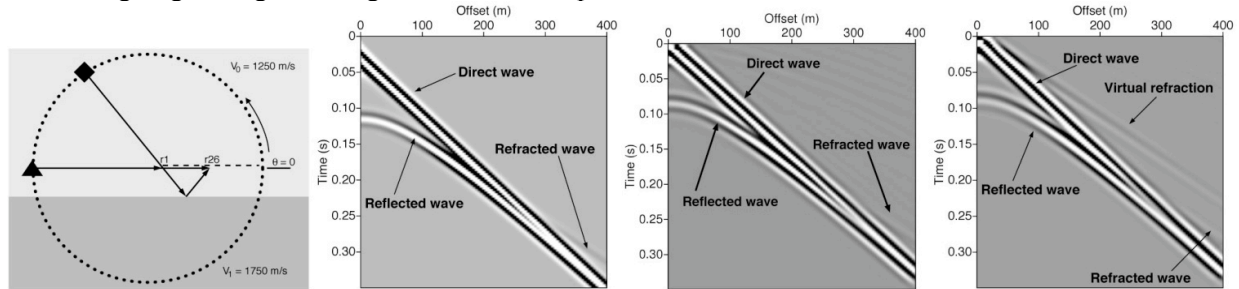


Figure 1: Left: Layout of the acoustic numerical model with 2880 sources on a circle with radius 475 m. Receiver r_1 is located 75 m to the right of the circle center. The diamond and square infer stationary phase points, important in the stationary-phase analysis. Middle left: shot record from an explosive source placed at receiver r_1 showing the direct, reflected, and refracted waves. Middle right: virtual shot record based on an exact seismic interferometry equation. Right: virtual shot record using only monopole sources on the circle. In addition to the real events, we observe a linear spurious event: the virtual refraction.

Reference

Wapenaar, K. and J. Fokkema (2006), Green's function representations for seismic interferometry, *Geophysics*, 71, S133–S146.

Adjoint tomography for the Middle East

Daniel Peter¹, Arthur Rodgers², Brian Savage³, Jeroen Tromp¹

¹ Princeton University

² Lawrence Livermore National Laboratory

³ University of Rhode Island

Using *SPECFEM3D_GLOBE*, we evaluate 3D models of the Middle East by computing full waveforms for several regional earthquakes. We measure travel-time shifts between observed broadband data and synthetic seismograms for distinct seismic phases within selected time windows using a recently developed automated measurement algorithm, FLEXWIN. We take advantage of *SPECFEM3D_GLOBE* together with the package *ADJOINT_TOMO* in order to calculate the sensitivity to seismic structure of the travel-time measurements for all available seismic network recordings for a fully numerical 3D seismic tomography approach.

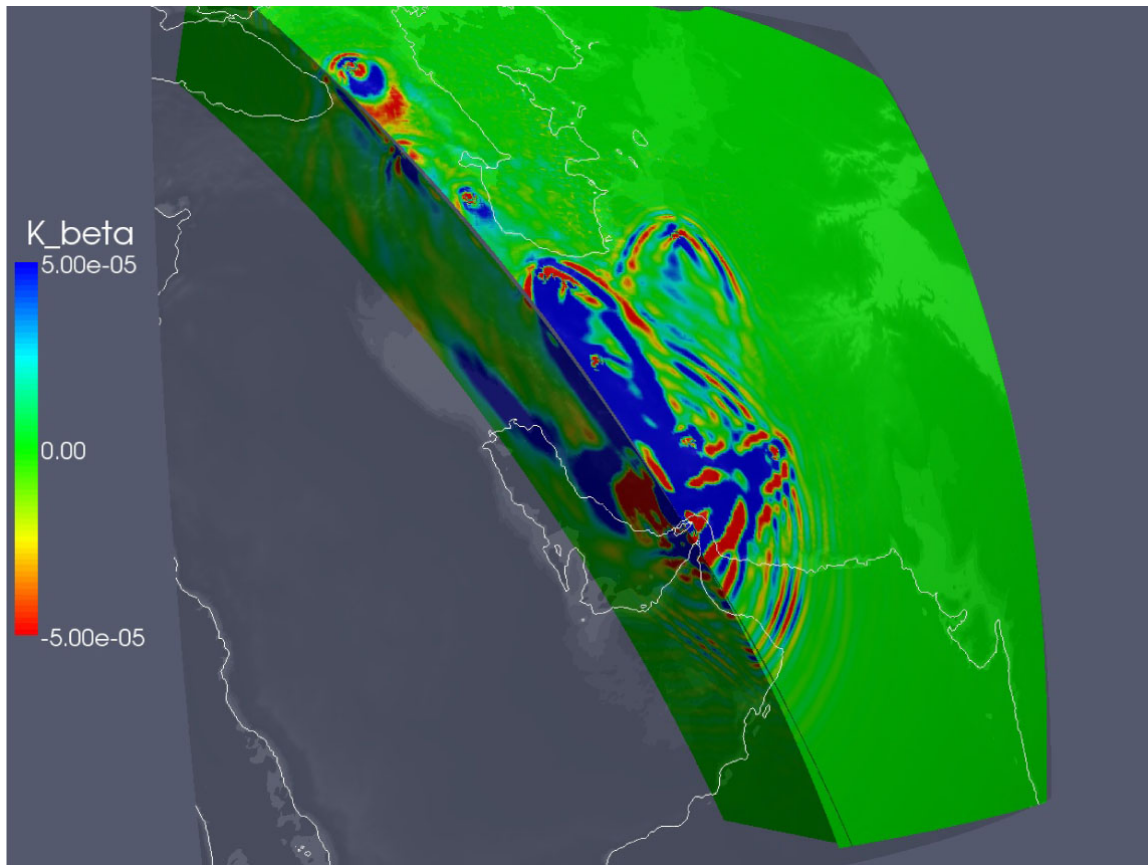


Figure 1: Shear-velocity event kernel for an earthquake in the strait of Hormuz recorded 2005 by several regional stations. Sensitivities are shown on a horizontal cross-section at 5 km depth and a vertical cross-section through the source and a station location down to a depth of 670 km.

Reference

Peter, D., A. Rodgers, B. Savage, and J. Tromp (2008), Adjoint tomography for the Middle East, *AGU fall meeting 2008*, paper presented.

Investigating the effects of 3-D anelasticity (Q) structure in global surface-wave propagation using the Spectral Element Method (SEM)

Youyi Ruan and Ying Zhou, *Department of Geosciences, Virginia Tech, Blacksburg, VA*

In the past decades, lateral heterogeneities in S-wave velocity in the upper mantle have been progressively mapped out in global surface-wave tomographic studies. It is known that S-wave speed anomalies can have either a thermal or compositional origin, or both. The earth's anelasticity (Q) structure has strong sensitivity to temperature and weak sensitivity to compositional variations, and therefore can be applied as additional constraints to distinguish between thermal and compositional variations in the mantle. Compared to S-wave velocity tomography, studies of the global anelasticity (Q) structure have advanced only slowly in the past decades. In fact, the effects of 3-D Q variations in surface-wave propagation have not been well understood.

In Ruan and Zhou [2009], we quantify the effects of 3-D anelasticity (Q) on surface wave phase delays by simulating wave propagation in 3-D anelastic earth models using the Spectral Element Method (SEM). We compare measured phase delays caused by 3-D anelasticity structure to those caused by 3-D velocity structure. The 3-D Q model and 3-D velocity model are both constructed from a 3-D temperature model, and the strength (rms) of the 3-D models is comparable to current tomographic models. Our measurements based upon synthetic SEM seismograms show that (1) roughly 20-30% of the observed phase delays (travel times) are due to 3-D anelasticity (Q) structure; this implies that neglecting 3-D anelastic dispersion effects can lead to biased velocity perturbations in seismic tomography; (2) the significance of 3-D anelastic dispersion is frequency dependent, it's stronger in long period surface waves as their sensitivity in the low-Q asthenosphere is maximized; (3) the 3-D anelastic dispersion effects are stronger in regions of “slow” anomalies where the temperature is higher than the background model and (4) focusing and defocusing effects due to 3-D velocity structure account for a major portion of observed amplitude perturbations in long-period surface waves.

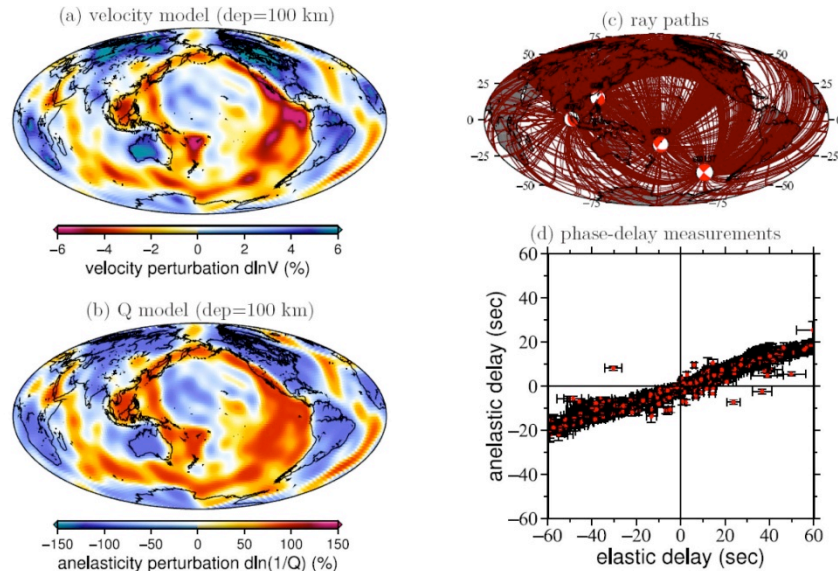


Figure 1: Examples of 100-s Rayleigh-wave phase delays caused by 3-D velocity structure and 3-D Q structure based upon global SEM wave propagation simulations in earth models.

References

- Ruan, Y. and Y. Zhou (2009), The effects of 3-D anelasticity (Q) structure on surface-wave phase delays, in preparation for *Geophysical Journal International*.
- Ruan, Y. and Y. Zhou (2008), The effects of 3-D Q structure on surface-wave phase delays, Abstract AGU, San Francisco, CA.

Adjoint tomography of the southern California crust

Carl Tape¹, Qinya Liu², Alessia Maggi³, and Jeroen Tromp⁴

¹ Seismological Laboratory, California Institute of Technology, Pasadena, California, USA

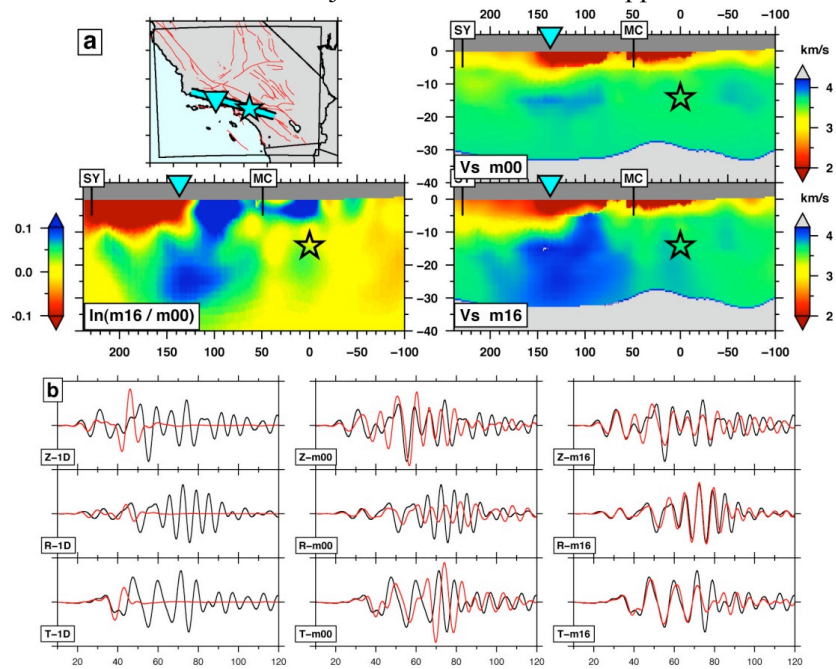
² Department of Physics, University of Toronto, Ontario, Canada

³ Institut de Physique du Globe, Université de Strasbourg, Strasbourg, France

⁴ Department of Geosciences, Princeton University, Princeton, New Jersey, USA

The purpose of our research is to improve 3D wavespeed models using the accuracy of SPEC-FEM3D simulations embedded within an inversion scheme based on adjoint methods. Our first application is for a southern California crust and upper mantle model (Komatitsch et al., 2004). We make measurements on 52,000 seismograms using the FLEXWIN algorithm (Maggi et al., 2009) and iterate the starting model 16 times, following the procedure discussed in Tromp et al. (2005); Liu and Tromp (2006); Tape et al. (2007). One example of the net changes made to the model is shown at right, along with the corresponding improvement of fit to the seismograms.

Figure 1: Cross sections of the tomographic model with corresponding seismograms. Boxed labels with vertical lines denote the location of the faults for reference: MC, Malibu Coast, SY, Santa Ynez. (a) Path for an M_w 5.4 earthquake (\star) beneath Chino Hills to station STC (∇), within the Ventura basin. (b) Synthetic seismograms (red) and recorded seismograms (black) for the period range 6–30 s. Left column, 1D model; center column, initial 3D model (m_{00}); right column, final 3D model (m_{16}).



References

- Komatitsch, D., Q. Liu, J. Tromp, P. Süß, C. Stidham, and J. H. Shaw (2004), Simulations of ground motion in the Los Angeles basin based upon the spectral-element method, *Bull. Seismol. Soc. Am.*, *94*, 187–206.
- Liu, Q., and J. Tromp (2006), Finite-frequency kernels based on adjoint methods, *Bull. Seismol. Soc. Am.*, *96*, 2383–2397.
- Maggi, A., C. Tape, M. Chen, D. Chao, and J. Tromp (2009), An automated time-window selection algorithm for seismic tomography, *Geophys. J. Int.*, doi:10.1111/j.1365-246X.2009.04099.x, in press.
- Tape, C., Q. Liu, and J. Tromp (2007), Finite-frequency tomography using adjoint methods—Methodology and examples using membrane surface waves, *Geophys. J. Int.*, *168*, 1105–1129.
- Tromp, J., C. Tape, and Q. Liu (2005), Seismic tomography, adjoint methods, time reversal, and banana-doughnut kernels, *Geophys. J. Int.*, *160*, 195–216.

Geodynamo Models with Core Evolution

Peter Driscoll and Peter Olson, *Dept. of Earth and Planetary Sciences, Johns Hopkins University*

Numerical dynamos with time-variable control parameters that simulate the secular evolution of the core are used to interpret long-term trends in geomagnetic field behavior, including changes in polarity reversal frequency. Dynamos with time evolution in convective forcing, inner core size, and rotation rate show trends in dipole field intensity and fluid velocity with systematic variations in polarity chrons in some cases. The dynamo model shown below started in a non-reversing state and subject to anomalously fast inner core growth rate (simulating a pulse of rapid cooling of the core) evolves over 20 Myr to a reversing state with substantial trends in dipole intensity and polarity chron length. The dispersion of polarity chron lengths in the dynamo model with anomalous evolution is qualitatively similar to the observed dispersion of geomagnetic polarity chrons since the end of the Cretaceous Normal Superchron.

The dynamo code MAG used here is supported by the Computational Infrastructure for Geodynamics (CIG).

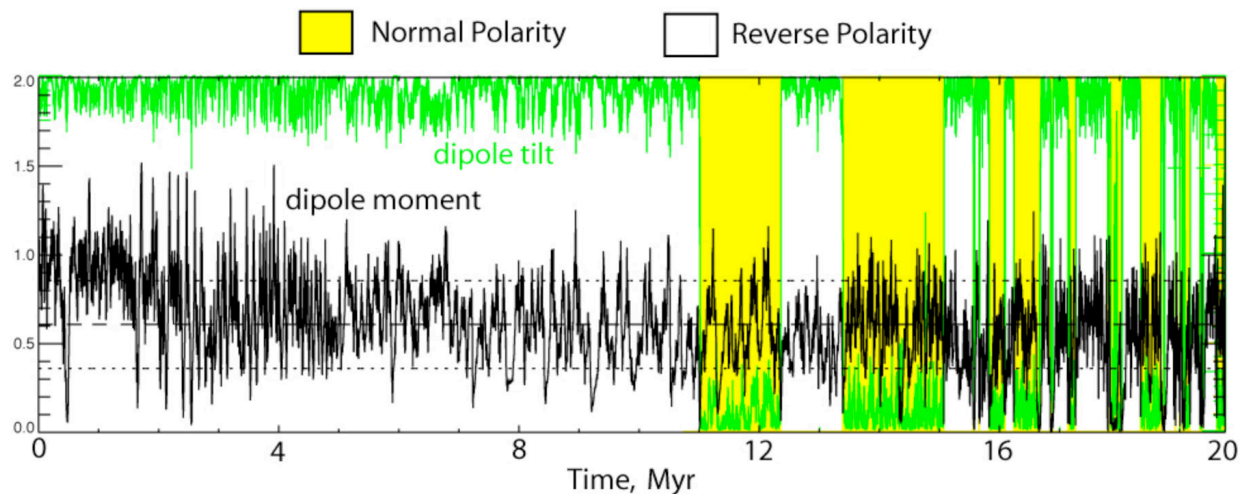


Figure 1: A 20 Myr simulation of an evolving geodynamo model, showing the effects of accelerated core cooling on the frequency of geomagnetic polarity reversals.

Reference

Driscoll, P. and P. Olson (2009), Polarity Reversals in Geodynamo Models with Core Evolution, *Earth Planet Sci. Lett.*, doi:10.1016/j.epsl.2009.02.017, in press.

Dipole collapse and reversal precursors in a numerical dynamo

Peter Olson and Peter Driscoll, *Dept. of Earth and Planetary Sciences, Johns Hopkins University*
Hagay Amit, *Institut de Physique du Globe de Paris*

Precursors to extreme geomagnetic field changes are examined in a numerical dynamo with a reversing dipolar magnetic field. The dynamo model shown below is driven by compositional convection in a rotating spherical shell and produces a strongly dipolar external magnetic field, with stable polarity epochs and occasional dipole collapses, some of which result in polarity reversals. We analyze the model behavior during dipole collapses that lead to polarity reversals, focusing on observable precursors. Reversed magnetic field induced in the dynamo interior by intermittent convective variability is the primary cause of dipole collapse. Spots of reversed magnetic flux emerge on the outer boundary at an early stage of the dipole collapse. The dynamo code MAG used herein is supported by the Computational Infrastructure for Geodynamics (CIG).

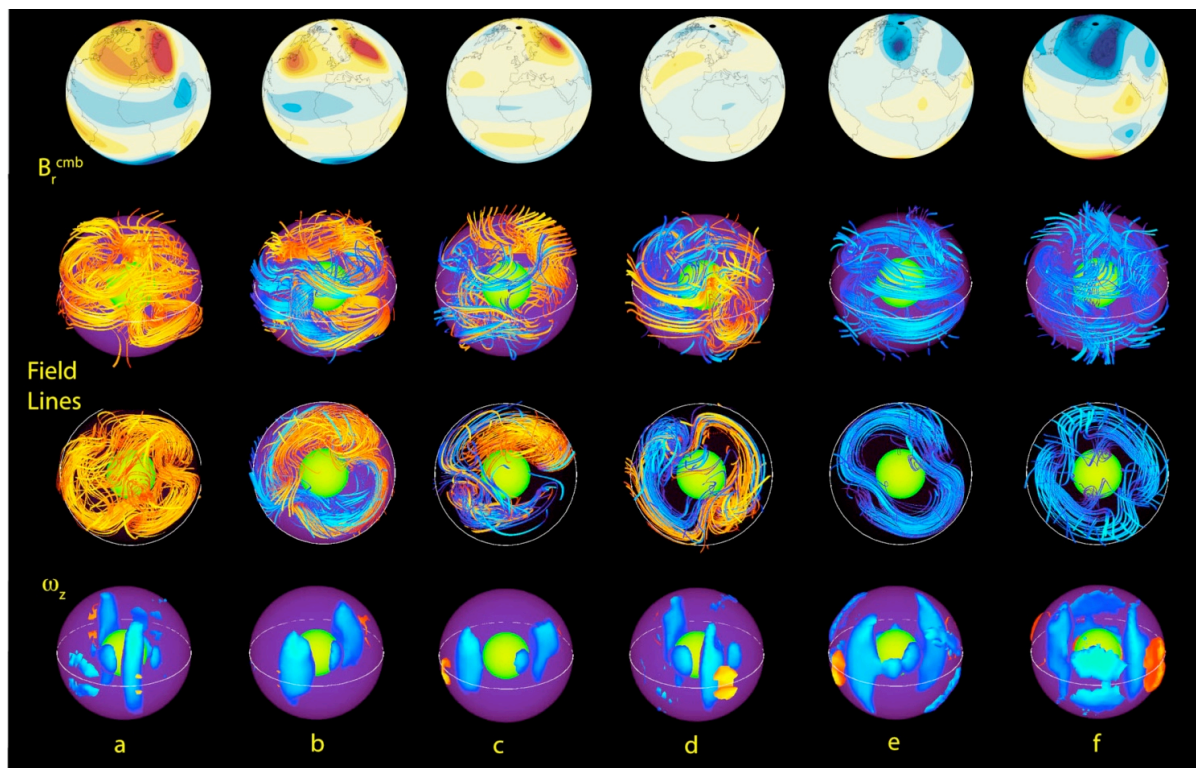


Figure 1: Magnetic dipole collapse and polarity reversal from a geodynamo simulation, in 5 kyr steps. Top row: radial magnetic field intensity on the core-mantle boundary. Middle rows: magnetic field line structure within the outer core (meridional and north polar views). Bottom row: axial vorticity of the convection.

Reference

Olson, P., P. Driscoll, and H. Amit (2008), Dipole collapse and reversal precursors in a numerical dynamo, *Phys. Earth. Planet. Inter.* 173(1-2), 121-140, doi:10.1016/j.pepi2008.11.0101.

Reproducing Observed Fault Statistics in 3D Numerical Models

Eunseo Choi and Roger Buck, *Lamont-Doherty Earth Observatory, Columbia University*

We plan to use SNAC, a CIG code for 3D solid modeling, to study the controls of strain weakening on fault statistics. We model the initiation of 3D extensional fault fields as in a preliminary model shown in Fig. 1 and would try to answer the specific question: What fault weakening parameters are needed to match normal fault population statistics for natural and analog studies? Statistics that we would consider include the size-frequency distribution and length-offset ratios. This work builds directly theoretical and numerical work we have done on 2D extensional faulting. We would look at the extension of uniform brittle (elasto-plastic) layers in an effort to find fault weakening parameter that give fault population statistics similar to those observed in the areas of extensional faulting (e.g., Gudmundsson, 1987), in simple 2D numerical models (e.g., Spyropoulos et al., 2002) and in laboratory experiments (e.g., Withjack and Schlische, 2006). Model predictions of D/L (displacement to length ratios), size-frequency distributions and spacing distributions are compared with published data. Next we would consider bending of layers, as may occur at subduction zones and see if we can reproduce the fault populations statistics that are observed to be different than for extensional faulting (e.g., Supak et al., 2006).

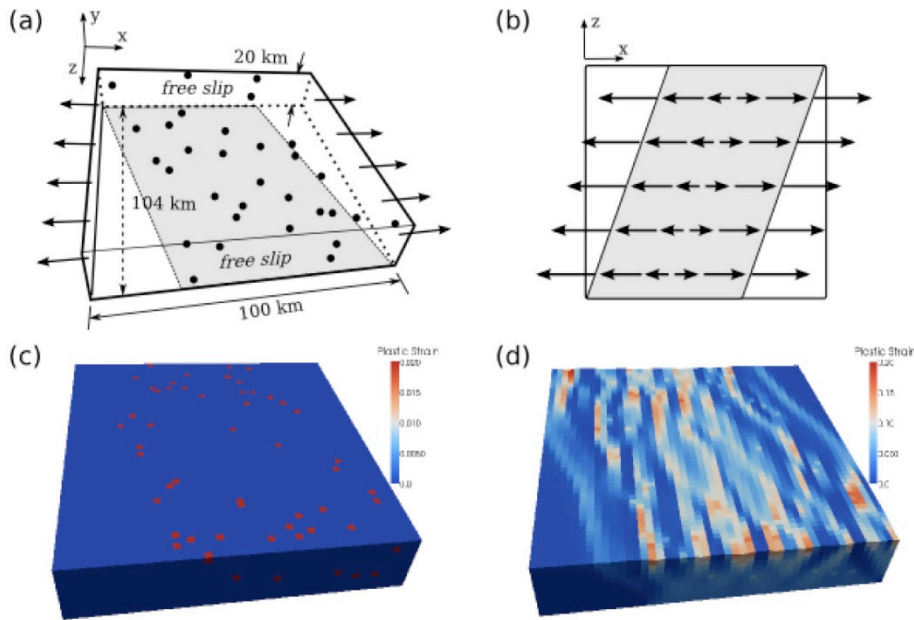


Figure 1 (a) The geometry of domain and the initial and boundary conditions. Arrows represent applied velocity boundary conditions (1cm/yr). Black dots represent randomly distributed “seed” elements with 2% of initial plastic strain. A constant strain rate is applied on the gray shaded region of the bottom surface. (b) The bottom surface viewed from below. The velocities applied to the gray region vary linearly across the width while the outside regions have uniform velocities. (c) The initial state of the test model. Red-colored elements are the “seeds” and are randomly distributed

within the oblique band. (d) Plastic strain accumulated after 0.1 Myr of extension, ranging from 0 to 20%.

References

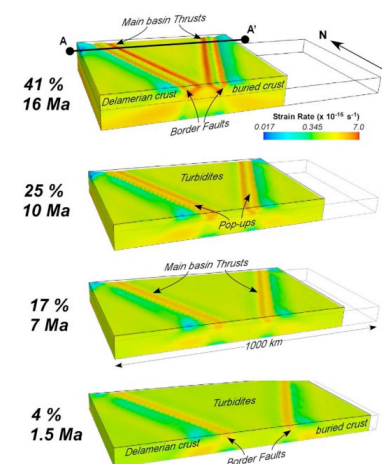
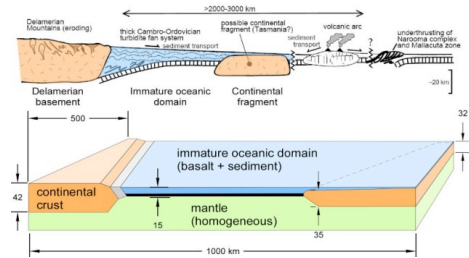
Gudmundsson, A. (1987), Geometry, formation and development of tectonic fractures on the Reykjanes peninsula, southwest Iceland, *Tectonophysics*, 139(3-4), 295-308.
 Spyropoulos, C., C. H. Scholz and B. E. Shaw (2002), Transition regimes for growing crack populations, *Phys. Rev. E*, 65(5), 056105.
 Supak, S. K., D. R. Bohnenstiehl, and W. R. Buck (2006), Flexing is not stretching: An analog study of bending induced cracking: *Earth and Planetary Science Letters*, 246, 125-137
 Withjack, M. O., and R. W. Schlische (2006), Geometric and experimental models of extensional fault-bend folds, *Analogue and numerical modelling of crustal-scale processes*, 253, Geological Society Special Publications, 285-305.

Application of Long-term Tectonic Simulations to Predictive Mineral Exploration: The Victorian Goldfields Architecture

Guillaume Duclaux, CSIRO Exploration and Mining, Bentley, WA, Australia, Minerals Down Under Flagship
 Tim Rawling, GeoScience Victoria, Melbourne VIC, Australia

A series of high strain simulations were run to examine the conditions favourable for the formation of terrane-scale high strain zones that provide the host architecture for most orogenic gold deposits in the western Lachlan Orogen of Victoria (SE Australia). Gale, a visco-plastic finite-element code based on Underworld, has been used to simulate the tectonic evolution of the area. It allows the simulation of large-scale deformation under realistic convergence rates. A simplified geometry representing an immature oceanic turbidite basin and its margins was shortened up to 60%. These simulations successfully reproduce some of the geological features of the western Lachlan Orogen, such as the development of major faults, their spatial distribution and their relative chronology.

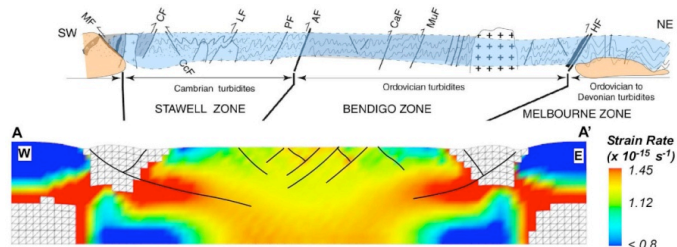
Figure 1: Model design. Comparison of the Lachlan tectonic model at 455 Ma (after Foster and Gray, 2000), incorporating a microplate in the eastern part of the western Lachlan with the model initial geometry used for the simulations. Crustal materials are visco-plastic, combining a Mohr-Coulomb yielding rheology and Frank-Kamenetskii viscous rheology. Mantle is defined as purely viscous. A constant velocity condition (convergence at 2.2 to 4.4 cm.yr⁻¹) is applied on the right wall of the model. Top surface is free to move.



Gale simulation results (Fig. 2) shown that the first structures to be activated as thrusts are the basin's passive margins (Border Faults). After about 3 Myr, these high strain zones start to widen. After about 7 Myr, backthrusts, dipping toward the edge of the basin develop within the basin and accumulate most of the strain (Main basin Thrusts). At that time 2 pop-ups are formed between the marginal border Faults and the Main basin thrusts. The general timing and fault sequence observed in our model is compatible with the tectonic evolution of the western Lachlan orogen as reported by Gray and Foster (2004) and Miller et al. (2006) (Fig. 3). Simulations also illustrate that the shortening is preferentially accommodated within the turbidite basin.

Figure 2: (Left) From bottom to top: Evolution of the Strain Rate second invariant

between 1.5 (4% shortening) and 16 Myr (41% shortening). As the convergence starts, thrusts develop at the basin's passive margins (Border Faults). After about 3 Myr, these high strain zones start to widen. After about 7 Myr, backthrusts, dipping toward the edge of the basin develop within the basin and accumulate most of the strain (Main basin Thrusts). Simultaneously, 2 pop-ups are formed between the Border Faults and the Main basin thrusts. (model resolution: 80 x 15 x 40). **Figure 3:** (Right) Comparison of a geological cross-section of the western Lachlan Orogen where major faults are highlighted (after Miller et al., 2006) with strain rate image along vertical section A-A' for Gale simulation (Fig. 2). The spacing and general distribution of the faults in the simulation (approximated by higher strain rate, highlighted by continuous black lines) is compatible with geological observations.



Gale simulations successfully reproduce the general deformation pattern proposed by previous authors resulting from field observations and recent geophysical interpretations. Long-term tectonic simulations are helpful tools to test simplified regional deformation scenarios and to understand crustal architecture. They also have the potential to inform exploration at increasing depth and undercover, and promote the discovery of new deposits in greenfield terrains where only coarse geological features are known.

References

Foster, D., Gray, D. (2000), *Annual Reviews of Earth and Planetary Science*, 28, 47-80.
 Gray, D., Foster, D. (2004), *Australian Journal of Earth Sciences*, 51, 773-817.
 Miller, J., Wilson, C., Dugdale, L. (2006), *Australian Journal of Earth Sciences*, 53, 677-695.

Mantle flow and crustal dynamics in southern California and the Pacific Northwest

Noah Fay, *Department of Geosciences, University of Arizona*

We calculate the small-scale convective flow of the southern California upper mantle and its influence on the dynamics and deformation of the overlying crust. Three dimensional anomalous upper mantle density structure, derived from shear wave tomography, is used to drive three-dimensional viscous flow using the CIG finite element code *Gale*. Figure 1 shows the resulting stresses on the base of the crust caused by flow of the underlying upper mantle. Regions overlying anomalously fast/dense upper mantle, such as in the Transverse Ranges and southern Great Valley (The Transverse Ranges and Sierra Nevada “drips”), are being compressed by mantle tractions (convergent vectors in Fig. 1) and regions overlying slow/buoyant upper mantle, such as the Salton Trough and southern Walker Lane Belt, are being extended (divergent vectors) by mantle tractions. We find a strong correlation between contemporary surface deformation (in particular dilatation) and crustal deformation predicted by the model suggesting these mantle tractions contribute significantly to the sum of forces deforming the southern California crust.

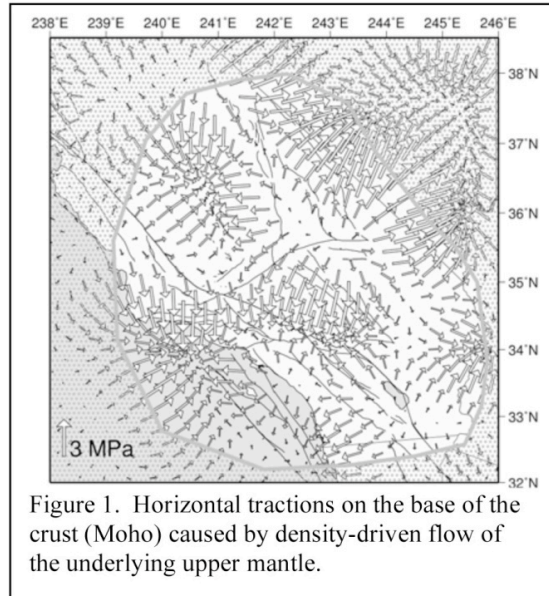


Figure 1. Horizontal tractions on the base of the crust (Moho) caused by density-driven flow of the underlying upper mantle.

Reference

Fay, N. P., R. A. Bennett, J. Spinler, and E. D. Humphreys (2008), Small-Scale Upper Mantle Convection and Crustal Dynamics in Southern California, *Geochem. Geophys. Geosys.* 9, Q08006, doi:10.1029/GC001988.

Recent seismic tomography models suggest the Juan de Fuca (JdF) slab beneath the Pacific Northwest may contain a hole or tear, or otherwise be discontinuous. We use the CIG code *Gale* to estimate how variations in JdF slab structure influence the mantle flow it induces during subduction. The subduction and rollback of a continuous and finite-length slab (Fig. 2a) excites a strong counter-clockwise toroidal flow around the edge of the slab.

A discontinuous slab (Fig. 2b) also excites a toroidal flow in addition to a flow through the ‘slab gap’ with a significant component of upwelling. Although speculative, this vertical mantle flow and associated decompression melting, and its progression through time as the slab subducts and possibly rolls back (to the west), may provide an explanation for the westward-migrating anomalous volcanism now located at Newberry caldera.

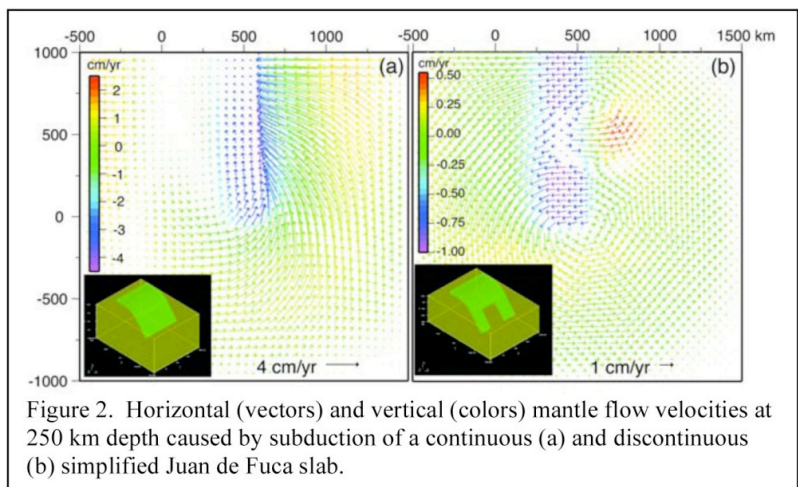


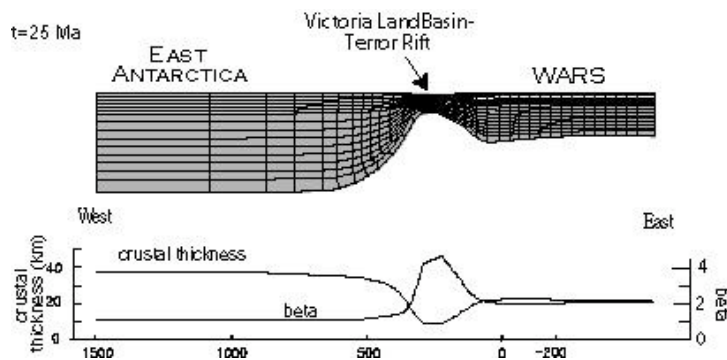
Figure 2. Horizontal (vectors) and vertical (colors) mantle flow velocities at 250 km depth caused by subduction of a continuous (a) and discontinuous (b) simplified Juan de Fuca slab.

Geodynamic Models of Extension in West Antarctica

Dennis Harry, *Colorado State University*

The Geodynamics group at Colorado State University (CSU) is investigating rifting in West Antarctica. The fundamental questions concern 1) why the mode of rifting in West Antarctic transitioned from a prolonged period of Late Mesozoic and Early Cenozoic diffuse extension that encompasses most of the Ross Sea to a more recent period of more focused extension in the Victoria Land Basin; and 2) what constraints do these rifting models place on the nature of the mantle beneath the rift system – is a hot mantle or impingement of a mantle plume required to explain the transition in the style of rifting (as previously argued) or is a cooler mantle consistent with the change in rift style? Our approach to investigating these issues is to develop finite element geodynamic models of the rifting process. We are using the CIG code *Gale* for this purpose, and plan to improve the code to better model the magmatic consequences of rifting.

Our models suggest that even modestly high mantle potential temperatures ($> ca. 1300\text{ }^{\circ}\text{C}$) are inconsistent with a transition from diffuse to focused extension. Assessment of magma production due to decompression melting shows these results to be marginally consistent with independent estimates of syn-rift magma volumes. However, the models that best fit the rift structural history invoke a cooler mantle and thus predict lower volumes of syn-rift melt. Models that best fit the total volume of syn-rift melt in the broad West Antarctic Rift System predict too much melt in the much narrower Victoria Land Basin portion of the rift.



We are currently working to expand this research. First, our models to date are 2-D. We feel that 3-D models will better capture the structural evolution of the rift, and that this may impact the melt predictions. Second, we have not yet considered melting of a fluid metasomatised mantle.

Figure (above) shows the finite element mesh, crustal thickness, and extension factor beta at the beginning of the Miocene (approximately 80 m.y. after extension began). Dark gray in top figure is crust, light gray lithospheric mantle. Vertical exaggeration is 2:1.

Reference

Huerta, A., and D. L. Harry (2007), The transition from diffuse to focused extension: Modeled evolution of the West Antarctic Rift system, *Earth and Planetary Science Letters*, 255, 133-147.

Geodynamic Models of Opening of the Gulf of Mexico

Dennis Harry, *Colorado State University*

The Geodynamics group at Colorado State University (CSU) is investigating opening of the Gulf of Mexico. We are focusing on two basic science issues. First, is the Gulf of Mexico a magmatic or amagmatic rift system? Second, what is the nature of the crust beneath the central Gulf of Mexico?

In regards to the first question, the northern Gulf region has long been considered to be a volcanic rift system, but this contrasts with a lack of evidence for widespread syn-rift magmatic rocks. Recent observations from the Iberia and Grand Banks rift margins, obtained primarily from IODP data, identified amagmatic rifts as a new class of rift margins. As the title implies, these margins are characterized by a lack of syn-rift magmatic rocks, as is observed on the northern Gulf margins. Geophysical data from the Iberia and Grand Banks margins (and data collected from subsequently recognized rift systems) suggests that amagmatic rift systems are also associated with anomalous seismic velocities in either the lower crust or upper mantle beneath the extended crust, and extremely wide zones of extended continental crust adjacent to the continental margin. Observations from the Gulf of Mexico are consistent with the observations from the other recognized amagmatic rift margins. Thus, we have a dichotomy. Traditional thinking is that the Gulf is magmatic, but many characteristics appear to resemble amagmatic rift systems.

The second question has great societal importance. The petroleum industry has traditionally considered oceanic crust to be non-prospective, due to a lack of source rocks (which, in early rift environments, generally accumulate atop continental crust). Comparison to other amagmatic rift systems indicates that the deep Gulf may not be underlain by oceanic crust as previously thought, and is instead underlain by highly extended continental crust or exhumed subcontinental mantle. This possibility leads to a new paradigm for hydrocarbon exploration in the Gulf.

The CSU group is exploring these issues through 3-D geodynamic modeling. Our goal is to test the amagmatic vs. magmatic models of rifting, and to explore the consequences of viable rifting models in regards to the nature of the deep Gulf crust. We are in the early stages of this modeling, but are using the CIG code *Gale* toward this end. Our intent is to transfer basic science, partially funded by NSF through CIG, into the private sector.

Funding

“The Nature of the Crust Beneath the Deep Gulf of Mexico and Development of the Syn-Rift and Early Post-Rift Gulf Basin” American Chemical Society Petroleum Research Fund, \$135,000, Jan. 1, 2007-Aug. 31, 2010. Principal Investigator: D. Harry.

References

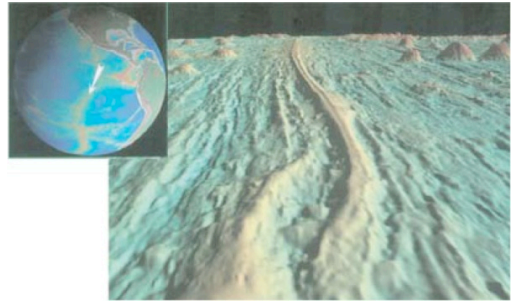
- Harry, D.L., Geodynamic Constraints on Opening of the Gulf of Mexico and the Nature of the Crust, Geological Society of America Annual Meeting, Houston, TX, Oct. 5-9 2008.
- Harry, D.L., Shifts in extension centers and the transition from amagmatic rifting to sea-floor extension. The Geological Society of London/SEPM Conference on “Rifts Renaissance: Stretching the crust and extending exploration frontiers, Houston, TX, Aug. 19-21, 2008 (invited).

3-D Faulting and Magmatism at Mid-Ocean Ridges

Garrett Ito, *SOEST, University of Hawaii, Honolulu HI*

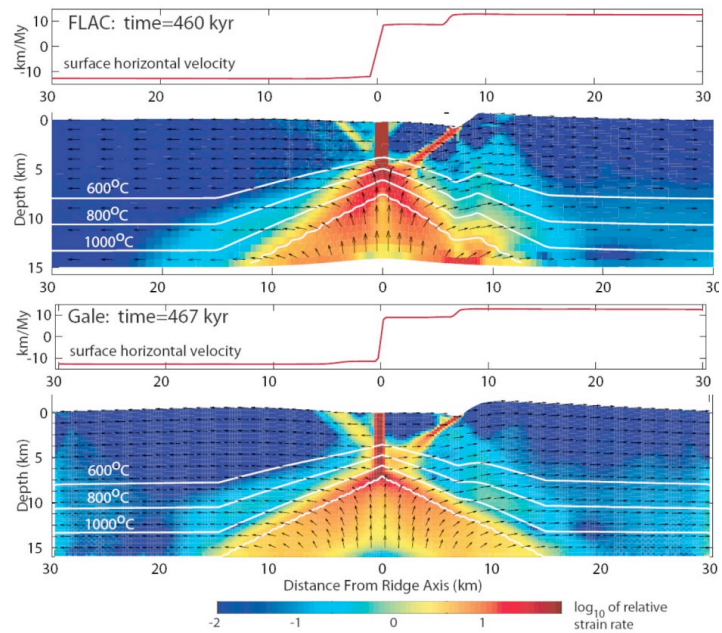
Mark D. Behn, *Woods Hole Oceanographic Institution, Woods Hole MA*

Faulting and magmatism at mid-ocean ridges influences the geometry of the plate boundary, shapes the topography of the axial zone, and creates seafloor fabric that covers two-thirds of the Earth's surface. The tectono-magmatic cycle at ridges creates a situation in which extension is accommodated partly by magmatic intrusions and partly by faulting. Magmatism is also heat source that influences the thickness of the brittle lithosphere out of which faults grow. Recent geodynamic studies have begun to quantify relationships between observable topographic characteristics and parameters such as the fraction of magmatic vs. tectonic extension and lithospheric thickness^{1,2,3}. In so doing, these studies have established a basic understanding of the kinematics of fault migration with plate motion, controls of the stresses on and brittle strength of the lithosphere, and the dynamic processes that determine whether the axis forms a deep valley versus a topographic high.



The above studies were limited to 2D (depth and cross-axis); however, the mid-ocean ridge plate boundary is inherently 3D, with large variations in the 3rd, along-axis direction. The amount of magmatism and lithosphere thickness can vary by many times along individual ridge segments, and spreading itself is disrupted by axial discontinuities in the form of transform faults, overlapping spreading segments, and non-transform offsets.

We have begun a study to quantify the response of faulting and topography to such along axis variations using the CIG-supported finite element code *Gale*. The figure to the right shows example solutions of surface velocity (positive to the right) and strain rate by a different, 2D code (FLAC) and *Gale*. Despite fundamental differences in the methods of simulating brittle behavior, the two codes predict similar times and amount of extension at which an active fault (right) begins to die at the expense of a new fault, which is beginning to form on the left plate. We are encouraged by these initial results and will soon be doing calculations 3D. This study is made possible by CIG and in particular by software engineer, Walter Landry, who has provided outstanding support in code development and assistance in adapting *Gale* for simulating faulting and magmatism at mid-ocean ridges.



¹ Buck, W. R., L. L. Lavier, and A. N. B. Poliakov (2005), *Nature*, 434, 719-723.

² Behn, M. D., and G. Ito (2008), *Geochem. Geophys. Geosys.* 9, Q08O10, doi:10.1029/2008GC001965.

³ Ito, G., and M. D. Behn (2008), *Geochem. Geophys. Geosys.* 9, Q09O12, doi:10.1029/2008GC001970.

Numerical Simulations of High Pressure Falling Sphere Experiments

O'Dwyer Brown, L., L.H. Kellogg, and C.E. Leshner, *Dept. of Geology, University of California Davis*

The physical properties of silicate melts are studied because they control numerous differentiation processes. Specifically, silicate melt viscosity and density control crystal growth kinetics, crystal settling and suspension, fractional crystallization and melt convection dynamics. These differentiation processes facilitate fractionation and ultimately influence the mantle's evolution and the petrology observed at the Earth's surface. There are many methods to determine density and viscosity of silicate melts at 1 atm. At high pressures, however, the viscosities of geologically relevant melts are widely determined experimentally using the falling sphere technique based on Stokes' Law. Density may also be determined through this method. Stokes' Law assumes that a rigid sphere falls slowly and steadily through a stationary and infinite Newtonian medium of uniform properties. High-pressure falling sphere experiments however, usually involve a dense refractory sphere falling through a liquid contained by a cylindrical capsule of finite size. The sphere velocity is influenced by the walls and the ends of the capsule, and possible convective motion of the fluid. We have used *Gale* to assess the limitations and assumptions of the high-pressure experiments by numerically simulating the conditions of these laboratory experiments. Models were set up to investigate the effects of the capsule's walls and ends (Figure 1), non-centered sphere trajectories (Figure 2), the presence of multiple spheres, varied cell geometries reflecting laboratory experimental innovations, and the consequences of thermal gradients on the sphere's velocity and trajectory.

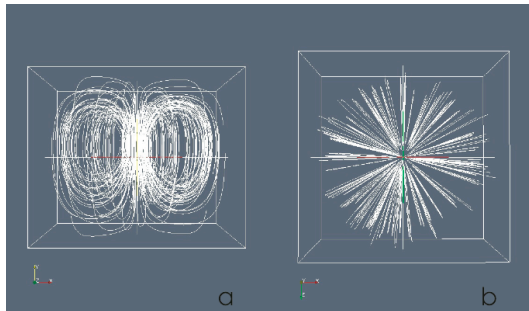


Figure 1a Streamlines of a 150 mm sphere falling along the central y-axis of a cylinder, viewed from z-axis.

Figure 1b Streamlines of a 150 mm sphere falling along the central y-axis of a cylinder, viewed from top of cylinder, down the y-axis.

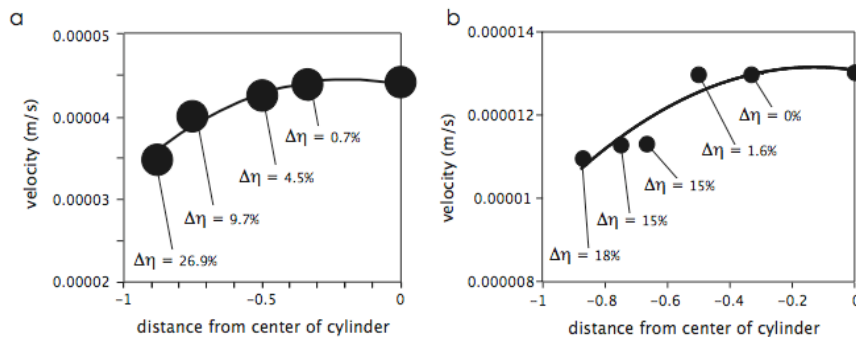


Figure 2a Velocities of 100 mm spheres falling at various distances from the central y-axis of a cylinder.

Figure 2b Velocities of 50 mm spheres falling at various distances from the central y-axis of a cylinder.

Reference

O'Dwyer, L., Kellogg, L.H., Leshner, C.E. (2007), Numerical Simulations of Falling Sphere Viscometry Experiments, *Eos Trans. AGU*, 88(52), Fall Meet. Suppl., Abstract MR13A-1257.

Collaborative Code Development with CIG

AuScope Simulation & Modelling Victoria – Monash University and VPAC

Steve Quenette, *Victorian Partnership for Advanced Computing, Australia*

Louis Moresi, *Monash University, Australia*

AuScope (www.auscope.org.au) is an Australian organization formed to facilitate the implementation of a world-class infrastructure system for earth science with a significant component of modeling software development. A fruitful and positive collaboration on software development has been built up between the Melbourne-based geodynamics software group in AuScope and CIG.

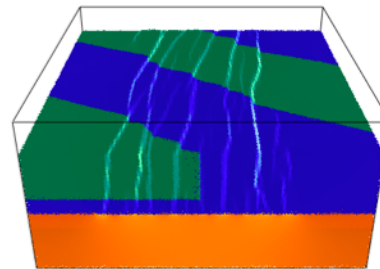


Figure 1: *Underworld/Gale model of shear deformation in a layered viscoplastic numerical experiment.*

We have held a number of developer-meets-user retreats in Australia with strong participation from members of the CIG team and the research community. At these retreats we have been able to solve outstanding issues raised by users, start seed projects, develop and trial new algorithm prototypes, discuss new developments in the field, and highlight risk areas for our projects. Both the *Gale* and MaDDS projects were initiated by retreats held close to Melbourne. Our developers and collaborators have also benefitted considerably from attending and contributing to CIG meetings.

In developing new software with CIG, we have consolidated Underworld as a framework for long-term geophysics, and StGermain as an environment for facilitating reusable numerical software. In turn CIG has contributed by driving features such as free surface deformation, PIC in irregular meshes, frictional boundary conditions, and solver configurations targeted to *Gale* problems.

The StGermain model for scientific code development is targeted at collaborative software development. Each component or feature is developed and maintained in isolation, contributed to a toolbox or plugin, and stitched into a “code” by means of an input file. In general, as new features become available, one doesn’t need to change their own code to use it. About two years ago the *Gale* developers forked *Gale* from the Underworld repositories, and in doing so isolated its users from the continually evolving features in our toolboxes and the framework itself. Some features that are readily beneficial include multigrid, refined PIC, REP, and so on. We believe the collaboration would strengthen if the CIG long-term geodynamics community were to adopt a policy to keep their code coherent with the Underworld release set.

The value our group then represents, is the research and implementation of numerical components that make the solve times for such systems tangible, on various computer architectures, as demonstrated to date.

Our vision is to provide the International long-term geodynamics community a platform for rapid and robust application development. There are three key challenges to scale our infrastructures to what the community might ask for in a “dream application.” One challenge for anyone implementing software infrastructure for these problems is, and will continue to be, the ability to describe complicated multi-scale, multi-physics systems and solve them efficiently, while simultaneously making such infrastructure available to novices, as well as to the math- and C-literate power users. A second challenge is to enabling flexible model development: our group is developing features such as template PDE equations to readily describe large coupled systems, configurable block based solvers, and compile-time stitching.

Creating a high quality software product for a diverse user-base and set of expectations is/will be a challenge for infrastructure providers such as CIG and our group. We are developing infrastructure to support users using auto-generated GUIs in conjunction with the Australian Grid programme. We’re also beginning to develop binaries that encompass all the dependencies, and continue making the traditional tar-ball frequent releases, and repository access. This infrastructure will leverage code- and meta-information already in the developed toolboxes, and will produce an environment for cost-effective development and maintenance of a spectrum of “codes.” Also, a new suite of unit, scientific, and system tests are in development.

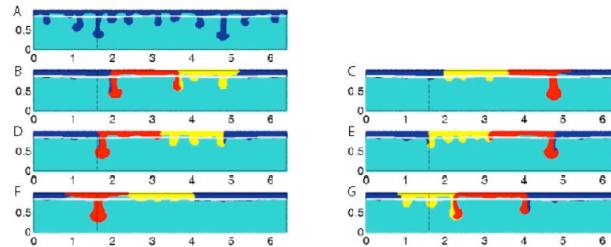
The effect of anisotropic viscosity on mantle dynamics

Einat Lev and Bradford H. Hager, *Massachusetts Institute of Technology, Cambridge, MA, USA*

Rocks often develop fabric when subject to deformation, and this fabric causes anisotropy of physical properties such as viscosity and seismic velocities. We use the finite-element code Underworld to investigate the effect of anisotropic viscosity on a range of mantle flows, including lithosphere instabilities and plate subduction. Underworld is an evolution of the code Ellipsis3D and stands at the base of Gale. Underworld is unique among mantle convection codes in that it includes handling of anisotropic viscosity and tracks fabric evolution.

Rayleigh-Taylor instabilities are the fundamental process behind lithosphere instabilities and diapirism. The results of our experiments demonstrate a dramatic effect of anisotropic viscosity on the development of instabilities – their timing, location, and, most notably, their wavelength is strongly affected by the initial fabric. Specifically, we find a significant increase in the wavelength of instability in the presence of anisotropic viscosity, which favors horizontal shear. We also find that interplay between regions with different initial fabric gives rise to striking irregularities in the downwellings. Our study shows that for investigations of lithospheric instabilities, and likely of other mantle processes, the approximation of isotropic viscosity may not be adequate, and that anisotropic viscosity should be included.

Figure 1: RT instabilities developed in isotropic (blue), anisotropic with horizontal easy glide planes (red) and anisotropic with 45-degree dipping planes (yellow). Note the difference in wavelength and location of drips.



The thermal structure of the mantle wedge in subduction zones controls the distribution of melting and the derived volcanism, as well as dehydration reactions and seismicity. Physical parameters such as subduction geometry, velocity and mantle rheology influence the thermal structure of wedges; we focus here on the effect of anisotropic viscosity. The abundant observations of seismic anisotropy in subduction zones collected in recent years suggest that the material in the mantle wedge has a strong fabric and may be mechanically anisotropic. We use two-dimensional finite-elements kinematic models constructed in Underworld. We find that anisotropic viscosity leads to two substantial changes: (1) a large increase in the partially-molten area through narrowing of the overlying lithosphere (figures 2, 3 below), and (2) time variability of the melt area and excess temperatures (figure 3). This behavior is observed for both linear and non-linear viscosities. The observed time-variability, a result of heterogeneity in alignment of the flowing material, can provide an explanation for temporal changes in melt observed in some volcanic regions, without having to invoke a change in the wedge geometry, slab age or composition.

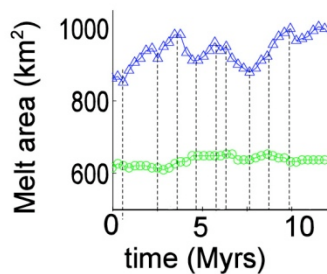


Figure 2: Total melt area as a function of time for isotropic (green) and anisotropic (blue) wedge viscosities

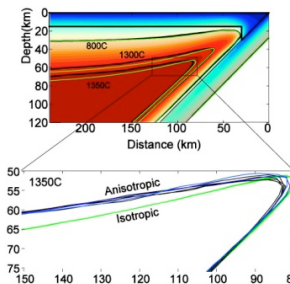


Figure 3: Thermal structure of the wedge nose. Note variability of anisotropic $T=1350C$ contours (blue) versus the isotropic ones (green).

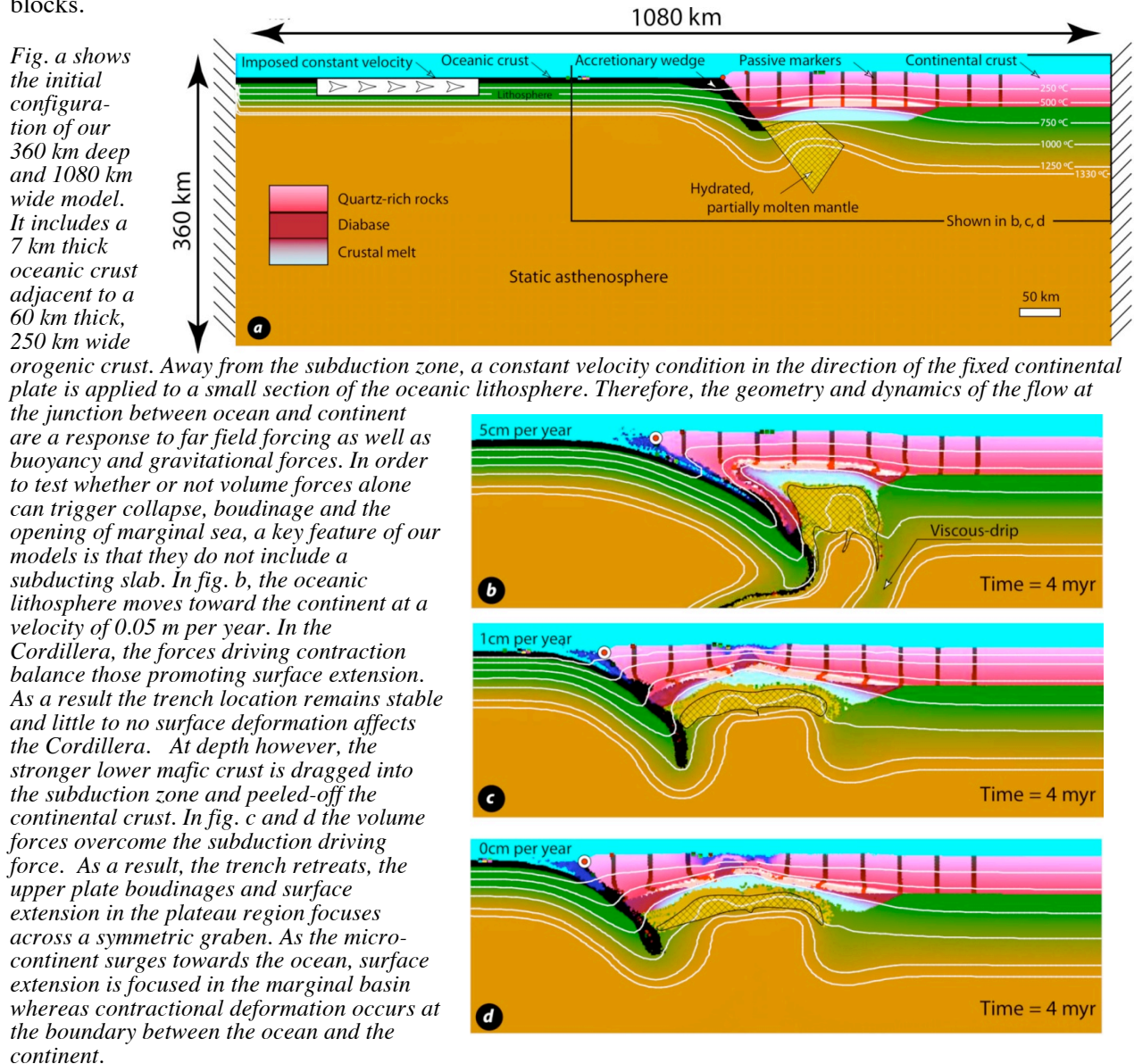
References

- Lev and Hager, Anisotropic viscosity changes the thermal structure at subduction zone wedges, in preparation for *Geophys. Res. Lett.*
- Lev and Hager (2008), Prediction of anisotropy from flow models – a comparison of three methods, *G-cubed* 9, Q07014, doi:10.1029/2008GC002032.
- Lev and Hager (2008), Rayleigh-Taylor instabilities with anisotropic lithosphere viscosity, *Geophys. Jour. Int.*, doi:10.1111/j.1365-246X.2008.03731.x

Active Plate Margin Fragmentation: Some Ellipsis Experiments

P.F. Rey and R.D. Müller, *EarthByte Research Group, The University of Sydney, Sydney, Australia*

On the basis of Ellipsis 2D thermo-mechanical numerical experiments we show that volume forces acting on Cordilleran-type orogens can drive a range of tectonic processes including gravitational orogenic collapse, the formation of marginal basins, trench retreat, slab rollback and ultimately the fragmentation of the plate margin via the detachment of microplates. In our model, trench retreat and slab rollback are a consequence of extension in the upper plate rather than its cause. The buoyancy of the mantle wedge underneath the Cordillera played a major role in the initiation of continental rifts leading to the formation and detachment of micro-continents, forcing trench retreat and the oceanward motion of the continental blocks.



Reference

Rey P. and R. D. Müller, (2008), On the dynamic of active continental margin. Australian Earth Science Convention, Perth.

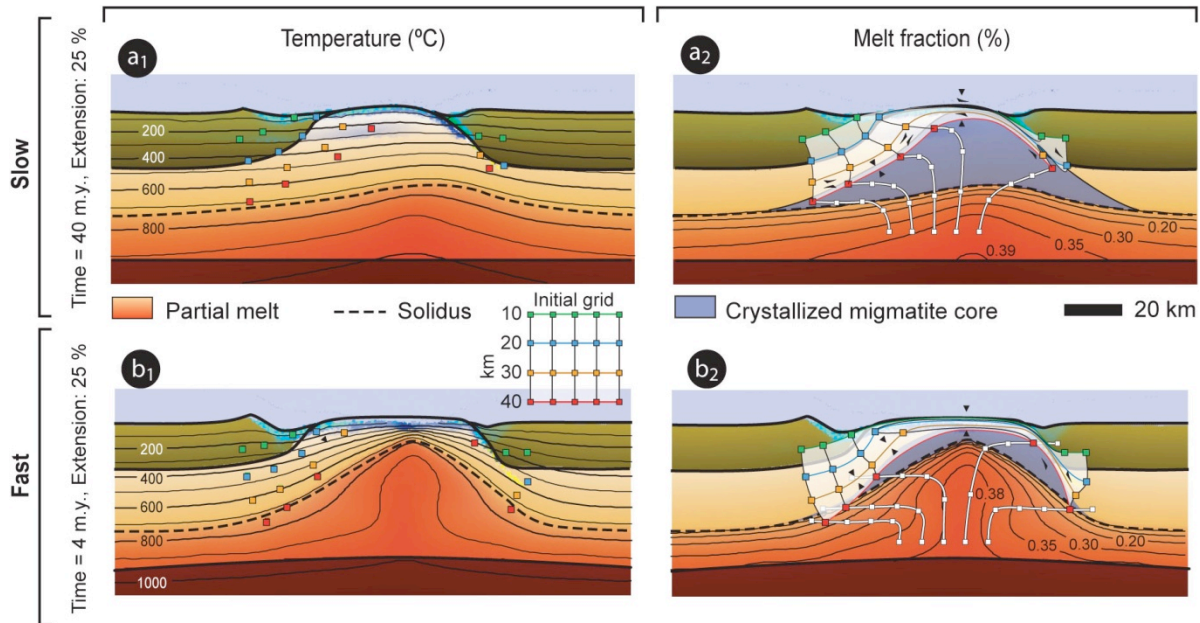
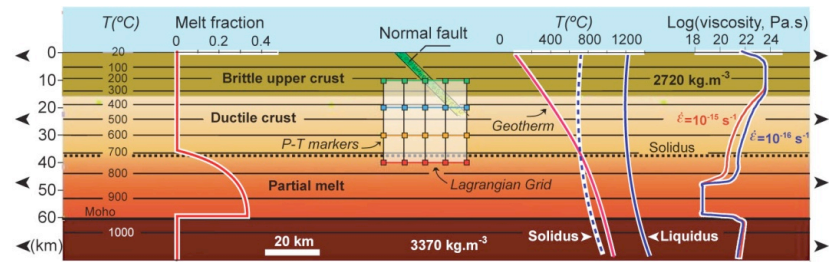
Extension Rates, Crustal Melting & Core Complex Dynamics

P. F. Rey, *EarthByte Research Group, The University of Sydney, Australia*

C. Teyssier and D. L. Whitney, *Dept. of Geology and Geophysics, University of Minnesota, MN, USA*

Migmatite-cored metamorphic core complexes are common crustal-scale features that develop when thick, partially molten continental crust is exhumed beneath low-angle normal faults (detachments) by extension. They offer an opportunity to study deep crustal processes; they contribute to the thermal and mechanical re-equilibration of orogenic crust and, as we show here through Ellipsis 2D experiments, record the kinematic boundary conditions prevailing during the final stages of orogeny.

Figure a: Initial and boundary conditions. The upper and lower crust have the same rheology and density structures, so the depth of the brittle-ductile transition evolves with strain rate and temperature. A melt fraction accounts for the thermal and mechanical effects of partial melting. The solidus and liquidus are adjusted to obtain a peak melt fraction of 35% at the Moho. The density of the partially melted region decreases linearly by 13% between the solidus and the liquidus, whereas the viscosity decreases linearly by 3 orders of magnitude when the melt fraction increases from 15 to 30%. There is no segregation of the melt from its source, a reasonable approximation for many migmatite-cored metamorphic core complexes, in which melt and solid fractions move en masse.



At high strain rates, migmatite cores crystallize and cool along a hot geothermal gradient (35 to 65°C km⁻¹) after the bulk of their exhumation. At low strain rates, migmatite cores crystallize at higher pressure before the bulk of their exhumation, which is accommodated by solid-state deformation along a cooler geothermal gradient (20 to 35°C km⁻¹). In the cases of boundary-driven extension, space is provided for the domes, and therefore the buoyancy of migmatite cores contributes little to the dynamics of metamorphic core complexes. The presence of melt favors heterogeneous bulk pure shear of the dome, as opposed to bulk simple shear, which dominates in melt-absent experiments. The position of migmatite cores in their domes reveals the initial dip direction of detachment faults.

Reference

Rey, P., Teyssier, C. & Whitney, D.L. (2009), Extension Rates, Crustal Melting and Core Complex Dynamics. *Geology* 37(5), L18303, doi:10.1130/G25460A.1.

The Fate of Continental Slabs

P. F. Rey, EarthByte Research Group, *The University of Sydney, Australia*

C. Teyssier and D.L. Whitney, *Dept. of Geology and Geophysics, University of Minnesota, Minneapolis, USA*

Ellipsis 2D thermo-mechanical numerical experiments can help predict the most likely mode by which continental slabs evolve under the action of thermal relaxation, partial melting, viscous forces, buoyancy forces and gravitational forces. In these experiments, we model a single subducting slab to show the first-order relationships of subduction, partial melting, and exhumation.

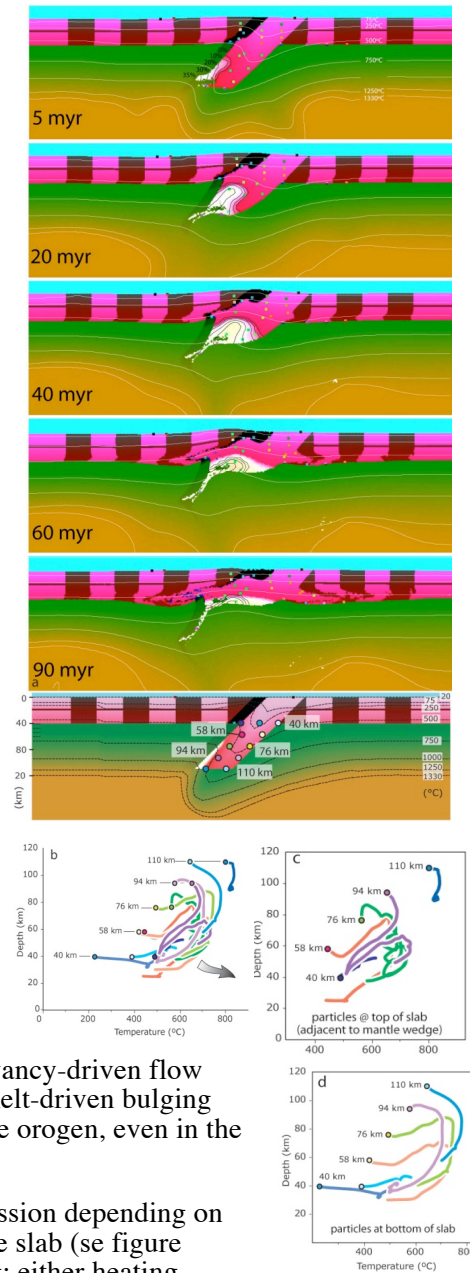
Our model is made of visco-plastic material with a temperature and stress dependent viscosity for stresses below the yield stress, and a depth-dependent plastic branch above the yield stress. For the continental crust and the mantle we use dislocation creep parameters of quartz-rich rocks and olivine, respectively. In our models, the rheology of crust also involves diffusion creep, as this mechanism of deformation becomes important under low differential stress, high temperature conditions, and when partial melt is present.

In the Ellipsis model, no extension is applied at the boundaries. Upward flow of crust is solely controlled by buoyancy and rheology. The crustal melt from the slab remains confined to the slab and ponds at the Moho, and the overlying crust is extruded horizontally into the weak lower crust of the overlying continent and displaces the Earth surface upward to form an orogenic plateau and the Moho downward to accommodate the influx of material into the lower crust. The volume of melt in the slab controls the rate of these processes, which can be accomplished in < 10 million years when large volumes of melt (> 75%) are present in the slab. For lower melt fractions the time-scale for buoyancy-driven flow can extend over many tens of million years. The combination of melt-driven bulging and lower crustal extrusion contributes to the construction of a wide orogen, even in the case of a single subduction zone, as shown in the model.

Rocks experience varying amounts of heating relative to decompression depending on the maximum depth of subduction of the rock and its position in the slab (see figure bottom right). Particles at the bottom of the slab experience heating; either heating during decompression (followed by a near-isotherm phase of decompression) for particles subducted to depths > 90km, or near-isobaric heating followed by decompression and cooling. Particles at the top of the slab (adjacent to the mantle wedge) have complex paths, including some paths that involve convection within the partially molten region in the continental slab (e.g., the path for the 76 km rock near the top of the slab). In the model, the 110 km rock at the top of the slab remains entrained in the mantle and stays at high temperature without significant decompression. Such a process would contribute to mixing of continental and mantle material and would influence the geochemical character of the mantle. The shallowest rocks that were tracked in the model – i.e. those at 40 km depth – are not incorporated into the partially molten region and experience only heating as they are extruded into the lower crust of the overriding continent, close to the Moho.

Reference

Whitney, D.L., Teyssier, C. & Rey, P. A new paradigm for mountain building: lithosphere-scale thrusting, melting, and the end of orogeny, *Nature Geoscience*, submitted.



How far can the plateau lower crust flow? Ask Ellipsis!

P.F. Rey, *EarthByte Research Group, The University of Sydney, Australia*

C. Teyssier and D.L. Whitney, *Dept. of Geology and Geophysics, U. of Minnesota, Minneapolis, USA*

Gravitational potential energy stored in an orogenic plateau can be sufficiently strong to deform the surrounding region (foreland), hence contributing to both plateau growth and collapse. Gravity-driven channel flow from the plateau lower crust into the foreland lower crust, called channel extrusion, has been proposed as a main contributor to the eastward growth of the Tibetan plateau, possibly driving the lower crustal channel as far as 1000 km. On the basis of numerical modeling using temperature-dependent viscosities and densities, we investigate channel flow extrusion and its impact on the stability of orogenic plateau.

The 400 km wide plateau region is made of a 70 km thick crust, which stands 4500 m above the foreland region for which continental crust is 40 km thick. In both the foreland and the plateau, the strong upper crust is made locally weaker by introducing a fault-shaped rheological anomaly. Viscous creep is modeled assuming both dislocation creep and diffusion creep. The lower crust of the plateau region is partially molten, which makes it more buoyant.

Figure a: Initial and boundary conditions

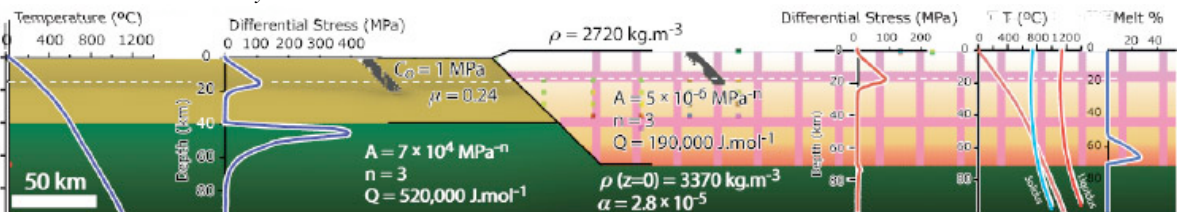


Figure b: Fixed boundary collapse: The velocity in the channel decreases from a few cm to a few mm per year in a few myr, due to cooling and crystallization of the channel as it travels through the cooler foreland. Soon after, the plateau channel starts to convect inhibiting further the laminar flow that was driven the plateau lower crust into the foreland. Under the gravitational push from the plateau, extension in the plateau focuses along a normal fault, which controls the exhumation of an incipient metamorphic dome. After 24 myr, the channel has traveled at most 150 km into the foreland.

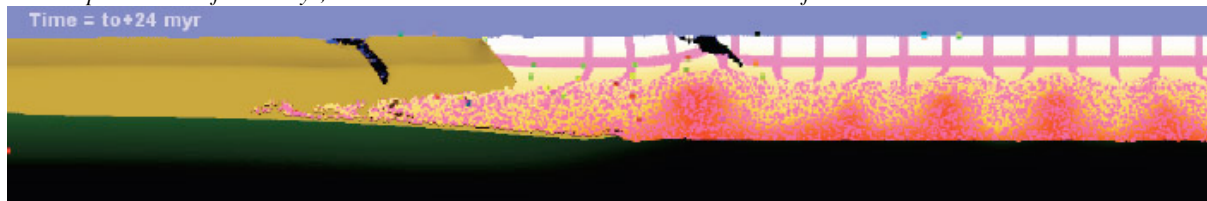
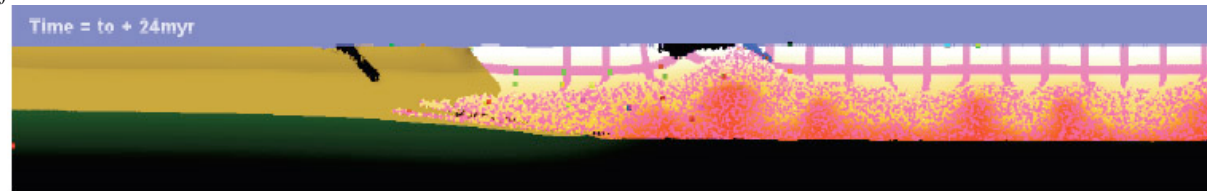


Figure c: In this experiment, the foreland is moving to the left at 2.3 mm per year (strain rate 10-16 s⁻¹). It shows that a modest boundary-driven extension activates zones of weakness in the plateau region, promoting the development of Metamorphic Core Complexes (MCC). Surface extension in the plateau provides a shortcut to the surface for the weak plateau channel, which flows into the growing MCC, inhibiting the channel flow extrusion into the foreland. Vigorous erosion along the plateau margins would have the same inhibiting effect on channel flow extrusion. After 24 myr, the channel has traveled at most 75 km into the foreland.



Within the limits of our model, the length scale of the extrusion channel is an order of magnitude less than what has been proposed for eastern Tibet (i.e. 100 km rather than 1000 km). Overall, our models cannot account for hundreds of km of channel flow extrusion as large magnitude channel flow extrusion is inhibited by any one of the following processes: cooling of the extrusion channel; convective motion in the plateau channel; and surface extension in the plateau providing a shortcut to the surface for the weak plateau channel. Results point also to a general incompatibility between coeval channel flow extrusion and the formation of metamorphic core complexes or aggressive localized erosion.

Reference

Rey, P., C. Teyssier, and D.L. Whitney (2009), How far can the plateau lower crust flow? EGU Vienna.

A comparison between lithospheric scale numerical and analogue models

J. Sheehan and B. O'Reilly, *Dublin Institute for Advanced Studies, Ireland*
 D. Sokoutis, *Netherlands Centre for Integrated Solid Earth Sciences, The Netherlands*

Both analogue and numerical methods seek to address similar problems, for example, how continental lithosphere stretches, deforms and subsides to form sedimentary basins. It is therefore reasonable to assume that these methods will generate similar results when applied to an identical problem. Some authors have already considered crustal scale comparisons with relative success. Such comparisons are especially beneficial for numerical codes, as no analytical solutions exist for problems of such complexity. In lieu of analytic solutions, analogue models can provide, in essence, a crude benchmark.

This study extends the previous crustal scale comparisons to the lithospheric scale, in an extensional context, using analogue models performed at the Vrije University Amsterdam and the numerical code *Gale*, which has been made available to researchers by the Computational Infrastructure for Geodynamics (CIG). This is an area that presents challenging problems in terms of boundary conditions for both methods. As far as possible, measured parameters for the analogue models are replicated in the numerical models to ensure a valid comparison.

Results are seen to be broadly similar, which provides encouragement in the consistency of both methods. It can be seen that *Gale* is capable of reproducing the gross geometry of the analogue model; however the faulting which occurs in brittle materials still remains a challenge.

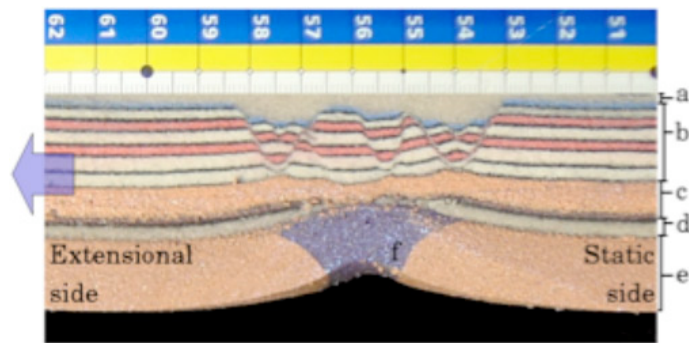


Figure 1

Figure 1: This is a section through the centre of an extensional, Lithospheric scale, analogue experiment in the direction of extension, post run. The labels are: a - quartz covering applied to model after extension to preserve surface features; b - brittle crust (feldspar); c - ductile crust ($\rho = 1350 \text{ kg/m}^3$, $\eta = 3 \times 10^4 \text{ Pa s}$); d - brittle mantle (quartz); e - ductile mantle ($\rho = 1489 \text{ kg/m}^3$, $\eta = 9 \times 10^4 \text{ Pa s}$); f - the weakened zone in the ductile mantle ($\rho = 1364 \text{ kg/m}^3$, $\eta = 1.9 \times 10^4 \text{ Pa s}$). The blue arrow indicates direction of extension (2.5 cm/hr).

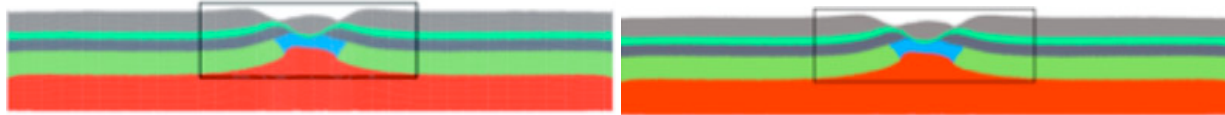
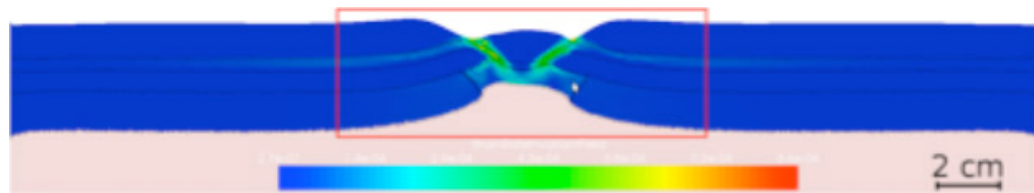


Figure 2a (with grid)

Figure 2a (without grid)

Figure 2a: Geometry of simulation of analogue model, with the portion contained in the black box corresponding to the portion of the analogue model shown in Figure 1. The layers are from top down, brittle crust, ductile crust, brittle mantle, ductile mantle and asthenosphere. Physical parameters such as density, velocity, and viscosity of the ductile layers are inherited from the analogue model. The brittle layers are modelled with Mohr-Coulomb yielding and an artificial viscosity of $5 \times 10^6 \text{ Pa s}$. The grid resolution is 240×80 with 30 sample points per grid element.

Figure 2b: Numerical models are able to display additional information such as viscosity, which regions of the model are exceeding the yield value, and in this case, the second strain rate invariant.

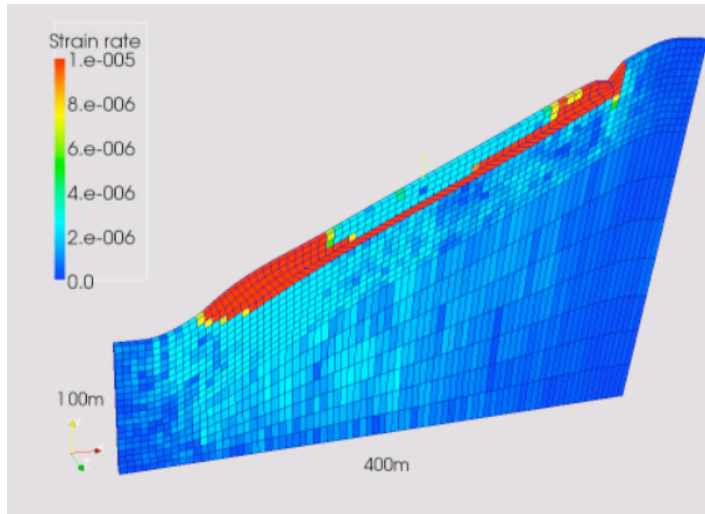


3D simulation of landslide failure and incipient runout

Colin P. Stark and Eunseo Choi, *Lamont-Doherty Earth Observatory*
Matteo Convertino, *IMAGE Dept., Univ. of Padova*

Landslides are a major environmental hazard and a fundamental process in the erosion of mountain landscapes. In both contexts, a major question is this: when a slope fails, how big will the landslide be? The question is a challenging one to study in the field or model numerically, because landslide volumes span many orders of magnitude and frequency, and because the mechanisms that control failure geometry are a matter of hot debate. We are conducting a pilot study to see whether this issue can be addressed through the modeling of large ensembles of landslide failures in 3D. We have chosen to use SNAC (Choi et al., 2008) and its ability to simulate the deformation of a heterogeneous Mohr-Coulomb material prone to strain weakening.

Our aim is to generate ~100 realizations of incipient slope failure given stochasticity in the governing



physical and topographic properties. Of particular interest are: (1) complexity in the way in which landslide ruptures grow; (2) how strain weakening mechanisms and heterogeneity distributions affect the structure of deformation; (3) the nature of scaling relations between length, depth, area and volume. These results will be compared with observations of landslide structures, variability and scaling to determine the quality of the modeling. Armed with these insights, we will then be able to evaluate the practicality and efficacy of a larger project (>1000 realizations) to study what controls the probability distribution (PDF) of landslide volumes.

Figure: First successful SNAC simulation of landslide failure. Strain rate @ $t=75$: snapshot. See <http://geomorph.ldeo.columbia.edu/grg/projects/landslides/snac-experiments/snac-expt-hillslope17> In terms of testing specific hypotheses, we will be able to discriminate between the idea of Katz & Aharonov (2006) that the PDF is a mix of two types of landslide generated in different ways and at two distinct scale ranges, and the model of Stark & Guzzetti (2009) that the PDF and its power-law scaling is the result of a single stochastic process of rupture propagation. In terms of SNAC/CIG code development, at the time of writing we have built a new SNAC plugin called hillSlope to handle model domain geometry, material heterogeneity, and simulation tracking. In addition we have made improvements to post-processing tools. These adaptations are currently undergoing testing on TeraGrid Ranger (project# TG-EAR090034).

References

- Choi, E., L. Laver, and M. Gurnis (2008), Thermomechanics of mid-ocean ridge segmentation, *Phys. Earth Planet. Interiors*, 171(1-4), 374-386, doi:10.1016/j.pepi.2008.08.010.
- Katz, O., and E. Aharonov (2006), Landslides in vibrating sand box: What controls types of slope failure and frequency magnitude relations? *Earth and Planetary Science Letters*, 247(3-4), 280-294, doi:10.1016/j.epsl.2006.05.009.
- Stark, C. P., and F. Guzzetti (2009), Landslide rupture, area and volume distribution, and debris mobilization, *Jour. Geophys. Res.*, in review.

MultiMaDDS – Implementing Magma dynamics with the commercial software COMSOL Multiphysics™

Laurent G. J. Montési, *University of Maryland, College Park, USA*

The Magma Dynamics Demonstration Suite (MaDDS) is a sequence of models defined for CIG by Spiegelman et al. [2007] as a guide to implement magma dynamics in a software platform. I have been implementing MaDDS in the commercial software COMSOL Multiphysics™ (MultiMaDDS project), used in my research group to model mantle flow, thermal evolution, shear zone formation, and elastic flexure. Implementing melt migration in COMSOL Multiphysics opens the door to new investigations of the various coupling in effect in the crust and upper mantle.

MultiMaDDS currently features MaDDS-1 (Stokes solver test), MaDDS-2 (Melt migration in a constant porosity background, Fig. 1) and MaDDS-4 (Solitary waves, Fig. 2). MaDDS-1 uses the predefined Navier-Stokes application and reveals the importance of using quadratic mixed-mode elements and unstructured meshes refined at the ridge's corner. MaDDS-2 was straightforward either as a post-processing step in Matlab or as a true multiphysics problem coupling the Navier-Stokes and Darcy application modes. For the Solitary Waves problem (MaDDS-4), it was necessary to use the PDE-general form mode coupled with a predefined Helmholtz equation mode.

As advertised, it is easy to couple various predefined modes (MaDDS-1, MaDDS-2) or even to define a custom mode from the PDE without the need to derive the weak form of the equation. However scaling is limited, as COMSOL cannot take advantage of DMM architectures. I find that advection is somewhat problematic: advection tests and solitary waves in a moving frame suffered from discretization artifacts. Nevertheless, the ease of use (including an intuitive GUI) and flexibility of mode coupling, mesh generation, and element choice make COMSOL a valuable tool for small geodynamics problem, exploratory studies, and student training. Inspired by this CIG activity, I developed simple geodynamics demonstration problems using COMSOL and posted them at <http://www.geology.umd.edu/~montesi/Geodynamics/ComsolModels.shtml>.

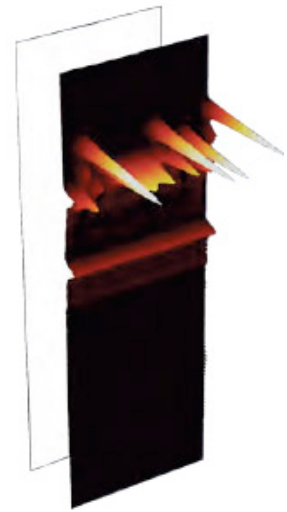


Figure 2: 2D Solitary wave (MaDDS-4) realized with COMSOL Multiphysics. An initial “bar” of high porosity breaks down into circular waves that rise with minimal (although non-zero) interaction. The simulation is realized in a reference frame that moves with the expected motion of the waves.

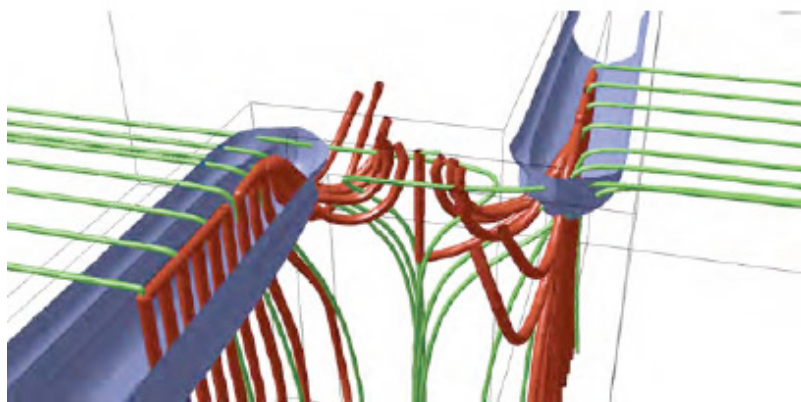


Figure 1: MaDDS-2 implemented with COMSOL Multiphysics. Green lines represent mantle trajectories underneath a segment ridge axis, with the blue surface a pressure isosurface and red are trajectories of magma assuming constant porosity. The model reproduces 2D focusing far from the ridge offset and 3D effects near the offset, including melts that cross the transform fault.

The development of stgMaDDS – the Magma Dynamics Demonstration Suite on StGermain

A collective explorative development effort between CIG & AuScope Simulation & Modelling through VPAC

Steve Quenette, Dave Lee, *Victoria Partnership for Advanced Computing, Australia*

Marc Spiegelman, *Columbia University, USA*

The aim of stgMaDDS was to implement the CIG Magma Migration working group's series of benchmark models [1], "the Magma Dynamics Demonstration Suite" to assess the feasibility of building these into an existing computational framework StGermain currently used for *Gale*. These models were specifically designed to highlight and benchmark the fundamental numerical and software challenges in developing the next generation of magma migration codes. In particular, to explore the computational issues in developing tightly coupled multi-physics fluid/solid solvers for FEM models at the mid-ocean ridge scale.

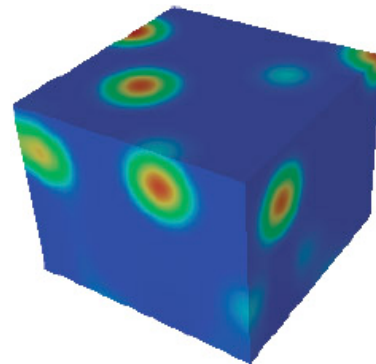


Figure 1 – From benchmark 4: A collection of 3-D solitary porosity waves

The effort began with discussions about Stokes and multi-scale and multi-physics solvers between Marc Spiegelman and Steve Quenette at CMG2006 in Israel. At that time CIG and VPAC were developing *Gale* based on Underworld through the StGermain approach and framework. This approach enables a 'building blocks' view of the complex numerical and physical problem. At the Magma Migration working group meeting at Columbia University a piecewise approach was decided based on incrementally solving the steps of the benchmark models.

The processes are modelled via a coupling of Stokes flow for the solid phase and Darcy's law for the flow of the melt through this deforming permeable material. The porosity field is dynamic and evolves in time in response to solid advection, compaction and expansion of the solid phase driven by fluid pressure and the degree of melting. The rate of asthenospheric melting is currently described via a simple productivity function proportional to the rate of decompression which may be modified with negligible affect on the rest of the code. More complex thermodynamic coupling, requires a larger multi-physics framework.

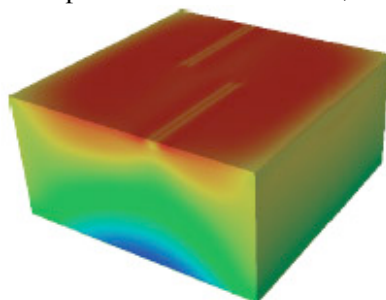


Figure 2 – From benchmark 5: A fully coupled isoviscous McKenzie system

VPAC appointed Dave Lee under the direction of Spiegelman, Luke Hodkinson and Steve to develop the software. Subsequently Dave May become involved as an early test case for his block matrix extensions to PETSc. Spiegelman invested some time to reformulate the benchmarks to better suit numerical models. The benchmark codes are available, with commentary at <http://www.geodynamics.org/cig/workinggroups/magma/workarea/benchmark>. The activity has been highly beneficial to all

parties involved. In particular, once implemented and correctness was proven, the emphasis has shifted to the development of adequate pre-conditioners. Marc has subsequently pursued methods and environment to explore pre-conditioner development. VPAC has subsequently begun developing a PDE level to its high level language, enabling much of the MaDDS problem to be described without having to write C or StGermain object code.

Reference

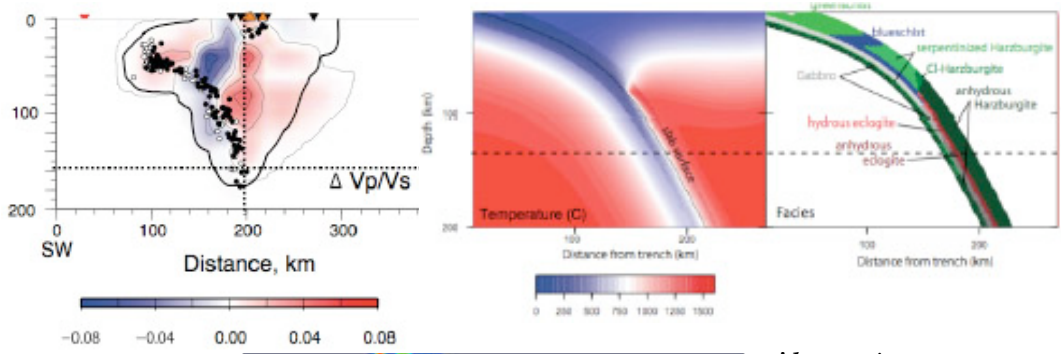
Spiegelman, M., R. Katz, and G. Simpson, 'An Introduction and Tutorial to the "McKenzie Equations" for magma migration', <http://www.geodynamics.org/cig/workinggroups/magma/workarea/benchmark/McKenzieIntroBenchmarks.pdf>

ArcFlow: Advanced models of fluid flow in subduction zones

Marc Spiegelman, *Columbia U.*, Peter van Keken, *U. Michigan*, Bradley Hacker, *UC Santa Barbara*

Subduction zones are one of the most critical components of global plate tectonics and mantle convection. They control the structure of the plates, are the major downwelling structures of mantle convection and control the geochemical cycling and transport between the surface and the deep interior. These systems are also perhaps the most difficult and complex geodynamic systems to model, requiring flexible multi-physics/multi-scale computations that can explore couplings between asthenosphere and lithosphere, brittle deformation, fluid-flow and magmatism. Considerable work has developed high-resolution solid flow and thermal models for subduction zones, but there has been much less modelling of the flow of hydrous fluids and magmas through the slab and wedge. Because many of the critical observations—including the position of volcanoes with respect to intermediate depth earthquakes, and variations in arc lava geochemistry—depend on the sources and pathways of fluids, considerable questions remain as how to relate these observations to the underlying dynamics.

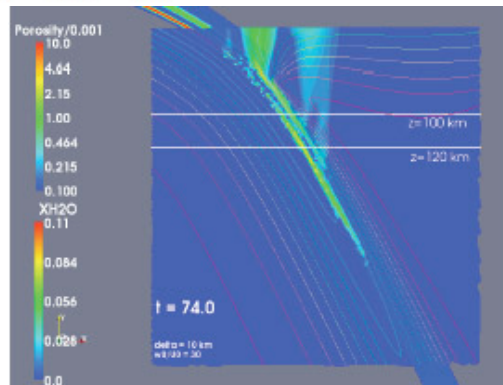
The ArcFlow project is an NSF-MARGINS funded project to develop advanced models for calculating and exploring the coupled fluid-solid dynamics of subduction zones, built on modern computational libraries (FEniCS, PETSc, Sepran, Perple_X). Key features of these models include the ability to reuse existing high-resolution thermal/solid flow models on unstructured grids that can be generated for specific arc geometries (van Keken using SEPRAN), together with thermodynamic calculations of phase diagrams to calculate the rate and distribution of fluid production in the slab (Hacker using Perple X). Given these inputs, the initial models solve for the explicit flow of fluid using the magma-dynamics formulation of McKenzie (1984), implemented in a hybrid Dolfin/PETSc code that utilizes automated code generation for coupled non-linear problems (FFC/Dolfin) together with PDE-based block-preconditioners (PETSc). The first generation of models address where and at what rates fluids are generated in the slab and explore the consequences of physical parameters such as permeability and solid rheology for affecting the potential fluid-flow paths through the slab and wedge. Initial results suggest that flow paths are sensitive to mantle rheology, with the possibility of considerable up-dip slab flow if the slabs are relatively strong. Future models will explore the direct coupling of fluid flow and solid flow in the wedge. The new FEniCS/PETSc will be made available through CIG and will contribute to the next generation of magma dynamics codes.



Top right figure, left side: Solid Flow/Thermal calculations for Nicaragua calculated using SEPRAN (van Keken) on a high-resolution unstructured mesh with nonlinear olivine rheology; **right**

side: consistent water-saturated facies for high-resolution submesh calculated using PERPLE_X (Hacker)

Above figure: Vp/Vs perturbations observed in Nicaragua (TUCAN experiment, Syracuse et al, G-cubed, 2009), showing potential fluid-flow paths in the wedge



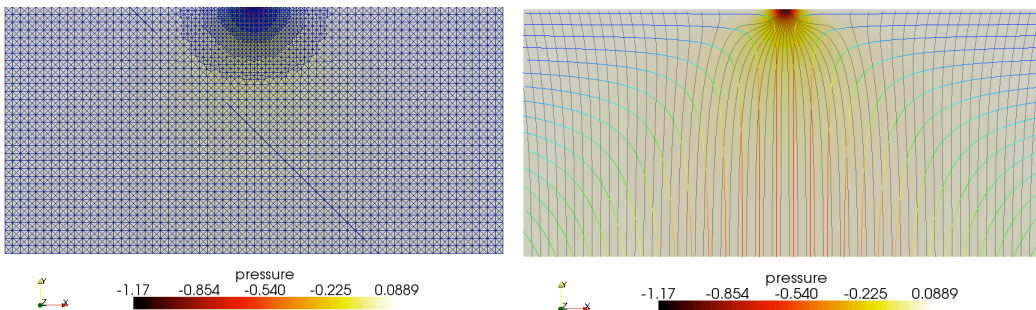
Bottom figure: Evolving porosity field for fluids produced by slab dehydration. Note, two principal dehydrating layers, a shallow layer that dehydrates rapidly supplying fluids to the “cold nose” and a deeper, serpentinized layer with considerable up-dip transport before being released into the wedge at ~ 120 km depth to the earthquakes. Calculations done using hybrid FEniCS/PETSc code (Spiegelman)

MADDs-FP – Flexible multi-physics models for Magma Dynamics using advanced computational libraries

Marc Spiegelman, *Applied Math/LDEO, Columbia U.*, Gideon Simpson, *U. of Toronto*

Magma Dynamics is one of the more challenging multi-physics problems in solid Earth Science, requiring a consistent coupling the flow of a low viscosity fluid or melt with large scale solid deformation (e.g. mantle convection or lithospheric deformation). The coupled system is non-linear, can be highly time dependent and is often unstable to the formation of coherent small-scale features such as magma waves or localized channels. To explore, these processes and understand how they affect observables and the large-scale flow requires computational software that allows flexible composition of a range of models from simple process models to more realistic regional plate-boundary models, as well as providing a wide choice in solver technology. Fortunately, recent advances in computational libraries such as the FEniCS project (www.fenics.org), PETSc (www.mcs.anl.gov/petsc/) and deal.II (www.dealii.org) provide such functionality.

As part of the Magma Dynamics component of CIG, I have developed a new set of hybrid FEniCS/PETSc codes that implement the Magma Dynamics Demonstration Suite of benchmarks (i.e., MADDs-FP), and are available as a Mercurial repository from CIG (hg clone <http://geodynamics.org/hg/magma/3D/MADDs-FP>). Key features used from FEniCS includes a high level language for describing the weak form of general PDE's (Unified Form Language UFL), a Form Compiler (FFC) for automatic generation of optimised C++ code, and a high-level interface for evaluating discrete functions (Dolfin) which allows easy development of semi-Lagrangian methods on fully unstructured meshes. These codes allow full use of PETSc's linear and non-linear solvers, including FieldSplit Block pre-conditioners for physics-based preconditioning. The actual choice of solver can be chosen at run time (or changed as the problem evolves). Specific Codes and Features include:



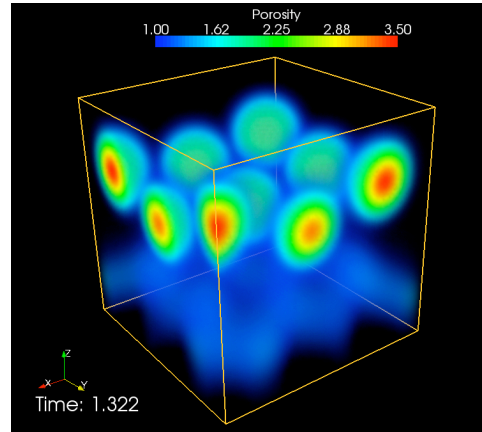
Left: mesh and pressure field from MADDs-1 Stokes solver. **Right:** fluid and solid flow lines for MADDs-2 on pressure field.

MADDs-1: Isoviscous Stokes flow for a mid-ocean ridge corner flow boundary condition using Taylor-Hood (P2-P1) elements on unstructured meshes and implementing optimal fieldsplit iterative solvers for isoviscous stokes (e.g., Elman, Wathen, etc.) as well as singular direct solvers in PETSc.

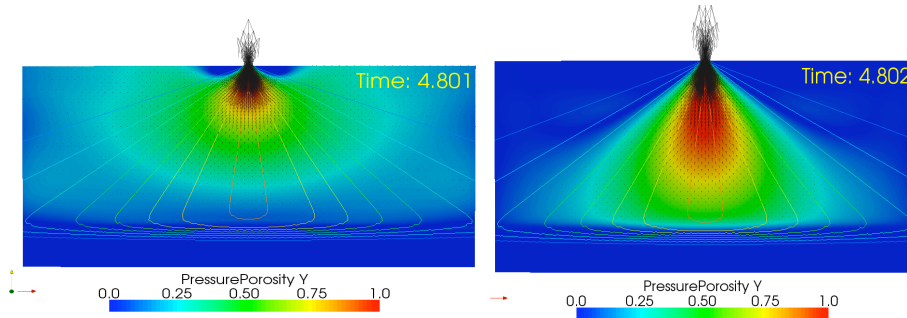
MADDs-2: A pyDolfin post-processing script to calculate the melt-velocity field given a uniform permeability, no melting and the solid velocity and pressure field from MADDs-1. This script also demonstrates how to project velocities and pressures onto non-trivial vector-valued finite element spaces (BDM) for calculating a flux-conservative melt flow field.

MADDs-4: A full-featured 2- and 3-D magmatic solitary wave Benchmark code. These codes include separate python routines for calculating spectrally accurate initial conditions for solitary waves in 1,2 and 3 Dimensions using Sinc collocation waves methods (Simpson & Spiegelman, 2009 in prep).

MADDs-5a: A 2-D time-dependent ridge melting and transport code that imports solutions from MADDs-1 for solid flow and calculates the consistent generation and transport of melt assuming adiabatic decompression melting. This model uses a new regularization of the magma equations which is easily composed in FEniCS, is fully time-dependent and uses time-adaptive implicit Newton solvers with semi-Lagrangian advection and physics-based preconditioners. Figure shows porosity/0.4%, contours of melting rate filed and melt flux for time-dependent run with moderate ($1e20$ Pa s and large shear viscosity $5e20$ Pas) both demonstrating enhanced melt flow to the ridge axis (box depth is 90 km).



Instability of 1-D solitary wave in 3-D calculated from MADDs-4.



Small-scale sublithospheric convection, a mechanism for non-hotspot volcanism

Maxim D. Ballmer¹, Jeroen van Hunen², Garrett Ito³, Paul J. Tackley¹, Todd A. Bianco³

¹*Inst. of Geophysics, ETH Zurich;* ²*Dep. of Earth Sciences, Durham Univ.;* ³*SOEST, Univ. of Hawaii*

Whereas hotspot theory accurately predicts many observations at some volcano chains, it is insufficient to explain the whole spectrum of intraplate volcanism worldwide. Though aligned by plate motion, many chains in the Pacific violate the predictions of hotspot theory in terms of linear age-distance relationships. One of the few alternative mechanisms put forward is small-scale sublithospheric convection (SSC). We use an extended version of the finite element code CITCOM to explore this concept in 3D geometry. SSC evolves at the bottom of mature oceanic lithosphere. In regions of the upper mantle with anomalously low viscosity (e.g., the South Pacific or, in the Cretaceous, the West Pacific), SSC may develop early enough (i.e., beneath sufficiently thin lithosphere) to support partial melting, and volcanism [1, 2]. SSC first removes the base of the depleted harzburgite layer, the residual from mid-ocean ridge melting.

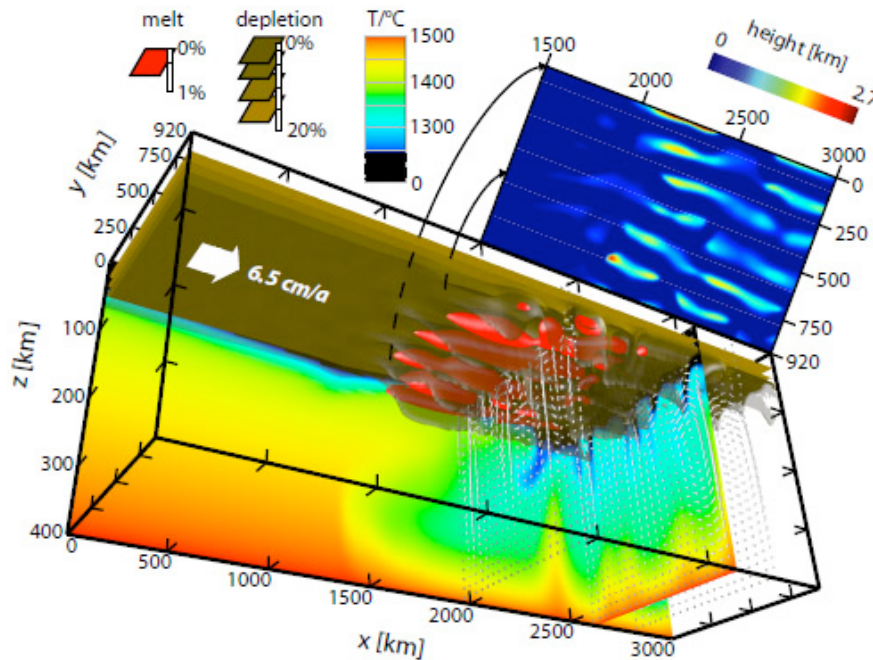


Figure: Isosurfaces of melt fraction and depletion, and cross-sections of the velocity and temperature fields for an example calculation. Lifted from the top is a plan view of the thickness of melt accumulated onto a plate moving over the box. The harzburgite layer is partly removed in downgoing sheets. Hence, partial melting emerges above SSC upwellings (Fig. from [1]).

Upwellings hereinafter bring fresh and warm asthenospheric mantle to depths of 80-100 km hence undergoing decompression melting. Melting zones from SSC are elongated and align with plate motion [1, 2], and thus reconcile quasi-synchronous volcanism over large distances (~1500 km)

along a volcanic chain as well as longevity of activity at an individual volcano. Vigorous SSC occurring beneath young seafloor is capable of melting the mantle matrix yielding depleted volcanism on seafloor of age 20-55 Myrs. In contrast, SSC occurring slightly later is only capable of fusing fertile blobs embedded in this matrix [3] yielding enriched volcanism on seafloor of age 35-70 Myrs [4]. Our numerical model predictions are consistent with geochemical observations, geochronological constraints, volcano heights, and the lateral spacing of the sub-chains of the Wakes, Marshalls, Gilberts, and Cook-Australs. Furthermore, ages along the Pukapuka ridges and the Line Islands are in concert with an origin from SSC [2], so as potentially some other volcano chains, for which only few or no reliable ages are available.

¹ Ballmer, M. D., et al. (2007), Non-hotspot volcano chains originating from small-scale sublithospheric convection. *Geophysical Research Letters* 34(23).

² Ballmer, M. D., et al. (2009), Intraplate volcanism with complex age-distance patterns – a case for small-scale sublithospheric convection. *Geochem. Geophys. Geosyst.*, submitted.

³ Ito, G. and J. J. Mahoney (2005), Flow and melting of a heterogeneous mantle: 1. Method and importance to the geochemistry of ocean island and mid-ocean ridge basalts. *Earth Planet. Sci. Lett.*, 230, p. 29-46.

⁴ Ballmer, M. D., et al. (2009), Small-scale sublithospheric convection reconciles geochemical and geochronological constraints from the Cook-Austral and Marshall Islands, to be submitted to *Geochem. Geophys. Geosyst.*

Geochemical variations at intraplate hotspots caused by variable melting of a veined mantle plume

Todd Bianco¹, Garrett Ito¹, Jeroen van Hunen², Maxim Ballmer³, John Mahoney¹

¹Department of Geology and Geophysics, SOEST, University of Hawaii, Manoa, Honolulu, USA

²Department of Earth Sciences, Durham University, United Kingdom

³Institute of Geophysics, ETH Zurich, Switzerland

A major form of volcanism on Earth occurs as chains of island-forming volcanoes, often associated with “hotspots” in the underlying mantle. Many of these hotspots are formed by plumes of hot ductile rock that rise from deep in the mantle and melt beneath the overriding tectonic plates. The compositions of these lavas, in terms of trace element and isotope ratios that finger-print material with different long-term evolution, provide an invaluable means by which to understand the compositional structure and evolution of the Earth. We use the 3D mantle convection code *Citcom* to investigate the geochemical consequences of the dynamics of flow and melting of a mantle plume interacting with a lithospheric plate. We assume that the mantle is a uniform mixture of heterogeneities with small scales ($\leq \sim 103$ m) and that begin melting at different depths. Models predict that the regional-scale, spatial variations in mantle temperature and flow associated with plume-lithosphere interaction create geographic zoning in the composition of lava rising out of the melting zone (Figs. 1 and 2). Consequently a volcano that passes over this melting zone with the moving plate is expected to sample different compositions as a function of time. Such changes in composition can explain some of the overall trends in isotope composition as observed between volcanoes and in stratigraphic records of the Hawaiian Islands. The results illustrate that magma geochemical zoning at the surface is not necessarily a map of zoning in the mantle, and this impacts further inferences about the chemical structure of the deep source that feeds mantle plumes.

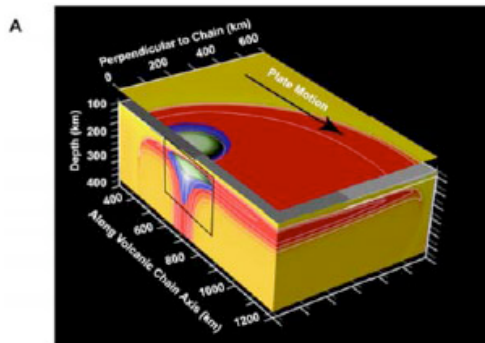


Figure 1. (a) 3D temperatures in shades of yellow (warm) and red (hot) of a mantle plume interacting with the lithosphere. Blue and light green areas show melting zones of two compositional components “EC” and “DC”. (b) Melting rate contours in the cross section in small box of (a). DC is more refractory than EC and melts in a smaller volume that overlaps the EC melting zone. Red lines are contours of fraction of partial melting; black lines are solid streamlines. The surface is moving to the right to simulate plate motion.

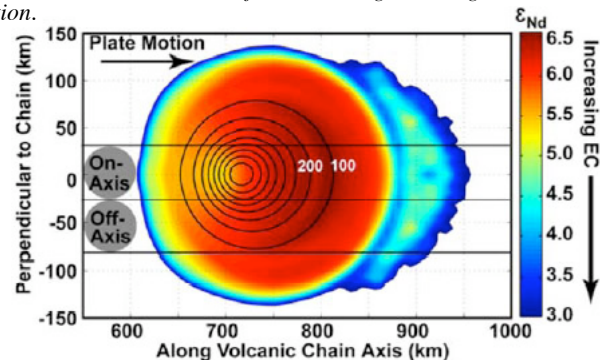
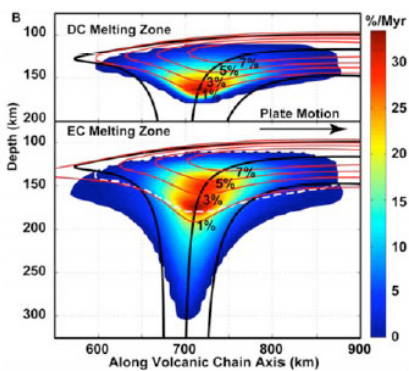


Figure 2. Map view of model Nd isotope composition (colored as ϵ_{Nd}) assuming EC (low ϵ_{Nd}) and DC (high ϵ_{Nd}) melts rise vertically and mix perfectly at the surface. Black contour lines are eruption rates in km^3/Myr (100 and 200 km^3/Myr are labeled); the center of these contours is the center of the hotspot. Gray circles mark areas from which volcanoes will sample magma; horizontal lines show the paths that two volcanoes take as they move with the plate.

References

- Bianco, T., G. Ito, J. van Hunen, M. Ballmer, and J. J. Mahoney (2008), Geochemical variation at the Hawaiian hotspot caused by upper mantle dynamics and melting of a heterogeneous, *Geochem. Geophys. Geosys.* 9, Q11003, doi:10.1029/2008GC002111.
- Bianco, T., G. Ito, J. van Hunen, M. Ballmer, and J. J. Mahoney (2009), Geochemical variations at intraplate hotspots caused by variable melting of a veined mantle plume, *in preparation*.
-

Enhanced Convection and Fast Plumes in the Lower Mantle Induced by the Spin Transition in Ferropericlase

Dan J. Bower, Michael Gurnis, and Jennifer M. Jackson, *Seismological Laboratory, California Institute of Technology*
Wolfgang Sturhahn, *Advanced Photon Source, Argonne National Laboratory*

We modify CitcomS 3.0 (obtained from CIG) to include the intrinsic density change that occurs from high to low-spin Ferropericlase around 50 GPa [Sturhahn et al., 2005]. This generates buoyancy similar to a discrete phase change. However, in pressure-temperature space the spin transition occurs over an extended pressure range for warmer material (Figure 1). The temperature broadening effect distributes spin-buoyancy over a large pressure range for warm plumes and a tight pressure range for cold slabs. In the deep mantle, spin-buoyancy works with thermal buoyancy and convection is enhanced for both upwellings and downwellings. In the shallow lower mantle spin-buoyancy mildly hinders convection.

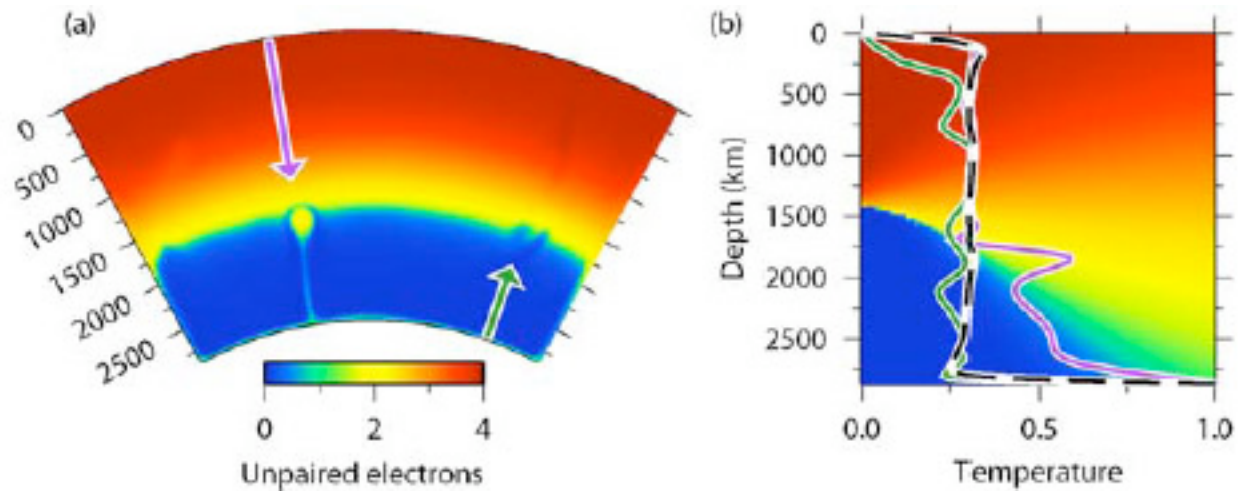


Figure 1. (a) Spin-state from simulation based on Sturhahn et al. (2005) spin model. Purple line is warm geotherm, green line is cold. (b) Geotherms with Sturhahn et al. (2005) spin-state model. Black dashed line is horizontal average.

Although the additional buoyancy does not fundamentally alter the large-scale dynamics, the Nusselt number increases by 5-10%, and vertical velocities by 20-45% in the lower mantle. Advective heat transport is more effective and temperatures in the core-mantle boundary region are reduced by up to 10%.

The spin transition, in addition to the Pv-pPv phase change, is a destabilizing mechanism that will further work against the stability of lowermost mantle structures. Furthermore, it provides additional buoyancy to small-scale hot plumes, such as those that possibly emanate from the edges of large low velocity structures.

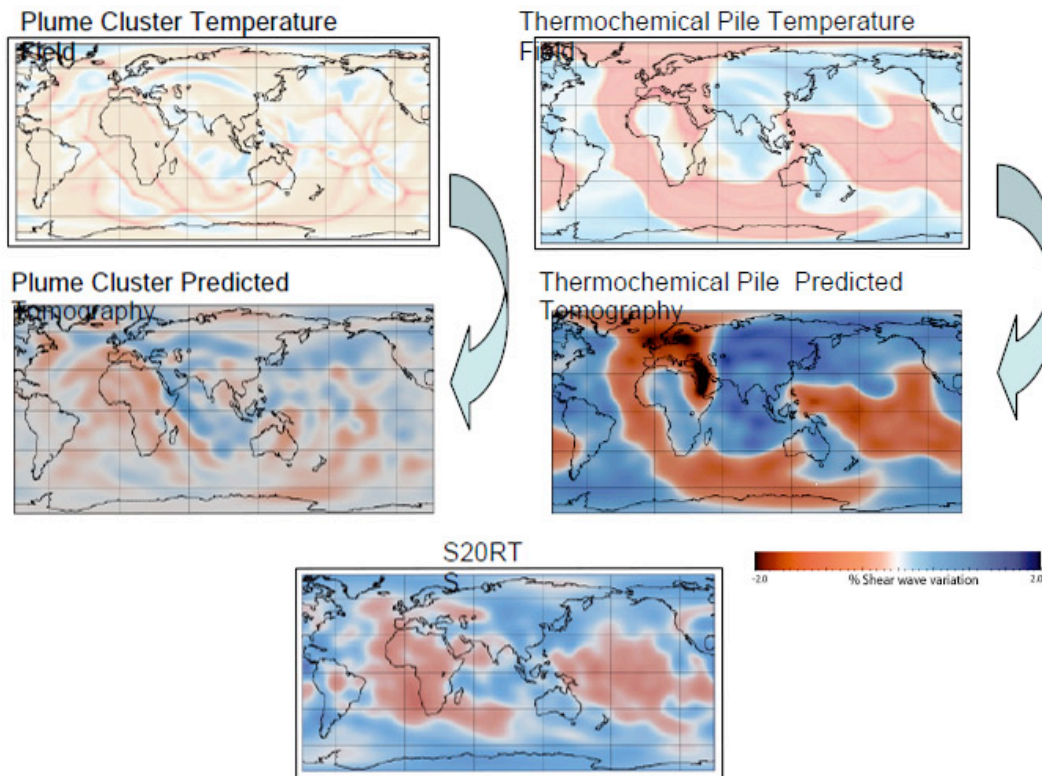
References

- Bower, D. J., Gurnis, M., Jackson, J. M., and W. Sturhahn (2009), Enhanced convection and fast plumes in the lower mantle induced by the spin transition in Ferropericlase, *Geophys. Res. Lett.*, 37, L10306
Sturhahn, W., J. M. Jackson, and J.-F. Lin (2005), The spin state of iron in minerals of Earth's lower mantle, *Geophys. Res. Lett.*, 32, L12307, doi:10.1029/2005GL022802.

Synthetic tomography of plume clusters and thermochemical piles

Abigail L. Bull and Allen K. McNamara, Arizona State University
Jeroen Ritsema, University of Michigan

Seismic tomography elucidates broad, low shear-wave velocity structures in the lower mantle beneath Africa and the central Pacific with uncertain physical and compositional origins. One hypothesis suggests that these anomalies are caused by relatively hot and intrinsically dense material that has been swept into large thermochemical piles by mantle flow. An alternative hypothesis suggests that they are instead poorly imaged clusters of narrow thermal plumes. Geodynamical calculations predict fundamentally different characters of the temperature fields of plume clusters and thermochemical piles. However the heterogeneous resolution of tomographic models makes direct comparison between geodynamical temperature fields and tomographic shear-wave anomalies tenuous at best. Here, we compute synthetic tomographic images from 3D spherical mantle convection models using CitcomS, and evaluate how well thermal plumes and thermochemical piles can be reconciled with actual seismic tomography images. Geodynamical temperature fields are converted to shear-wave velocity using experimental and theoretical mineral physics constraints. The resultant shear-wave velocity fields are subsequently convolved with the resolution operator from seismic model S20RTS to mimic the damping and distortion associated with heterogeneous seismic sampling of the mantle. We demonstrate that plume clusters are tomographically blurred into two broad, antipodal velocity anomalies in agreement with S20RTS and other global seismic models. Large, thermochemical piles are weakly distorted by the tomographic filter. The power spectrum of velocity heterogeneity peaks at spherical harmonic degree 3, unlike the degree-2 maximum in S20RTS, but decays rapidly similar to S20RTS and many other seismic models. Predicted tomography from thermochemical pile and plume cluster models correlate equally well with S20RTS given the uncertainties in the numerical modeling parameters. However, thermochemical piles match tomography better in visual comparison and in the overall character of the harmonic spectrum.



Reference

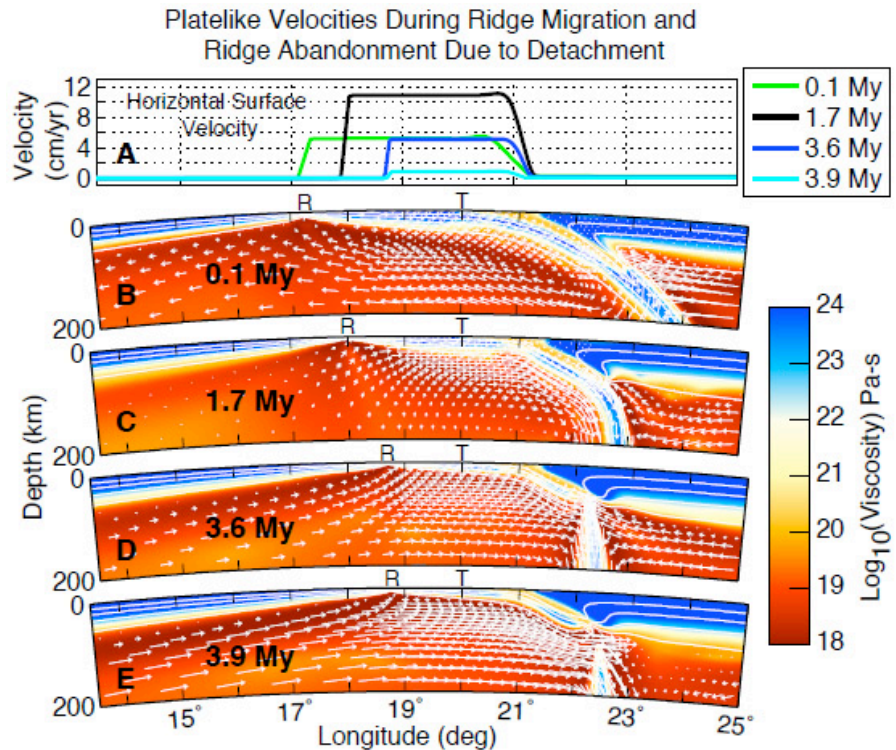
Bull, A.L., A.K. McNamara, and J. Ritsema (2009), Synthetic tomography of Plume Clusters and Thermochemical Piles, *Earth and Planetary Science Letters*, 278, 152-162.

2D Dynamics of Slab Detachment Due to Ridge-Trench Collision

Erin Burkett and Magali Billen, *Dept. of Geology, University of California, Davis*

Fully-dynamic 2D viscous models run using CitcomCU show that ridge-trench collision results in detachment of the subducted slab and abandonment of the spreading ridge for a case in which the ridge is oriented parallel to the trench. The initial thermal structure for our models defines a slab with a previous history of subduction and a spreading ridge positioned outboard of the trench. The model rheology is a composite dislocation-diffusion creep viscosity with a depth-dependent plastic yield stress. The plate boundary is modeled as a low viscosity shear zone.

Figure 1: Plate velocities and Viscous Flow Field. (A) Horizontal surface velocity profiles at four times before and during detachment for the same longitudinal extent as the plots below. (B)-(E) Viscosity plots for reference model. The changing ridge position is noted by an R and the fixed trench position by a T. White arrows indicate flow and white lines are temperature contours every 300°C.



We find that slab detachment, ridge abandonment, and opening of a shallow slab gap occur for a range of initial ridge positions (300-700 km outboard of trench), initial slab depths (200-1200 km), maximum yield strengths (300-1000 MPa), and shear zone viscosities (1021-1023 Pa-s). In none

of the cases tested does the ridge subduct, indicating that ridge subduction is not a prerequisite for slab detachment. Figure 1 summarizes the dynamics of ridge migration during subduction. First the subduction rate increases to a steady-state value (Fig. 1B-C). As necking of the slab begins, subduction rate rapidly decreases (Fig. 1D) before detachment of the slab and ridge abandonment occur (Fig. 1E). The uniform surface velocity from the ridge to the trench demonstrates rigid plate behavior during subduction, even as the plate velocity decreases because coupling of slab pull to the subducting plate drops as the slab detaches (Fig. 1A). The detachment occurs at a point along the slab where the age of the lithosphere is in the range of 7-12 My, indicating that increased weakening and positive buoyancy with proximity of the ridge to the trench lead to detachment of the older subducted slab from lithosphere younger than approximately 10 My. These results are consistent with observations of ridge abandonment offshore of Baja California together with anomalous volcanism along the peninsula suggesting the presence of a gap within the subducted slab.

Reference

Andrews (aka. Burkett), E. R., and M. I. Billen (2007), Competing Effects of Ridge Proximity and Slab Strength on Slab Detachment, *EOS Trans. AGU*, 88(52), Fall Meet. Suppl., T11C-0729.

Global Mantle Flow and the Development of Seismic Anisotropy

Clinton P. Conrad, *University of Hawaii*

Mark D. Behn, *Woods Hole Oceanographic Institute*

Viscous shear in the asthenosphere accommodates relative motion between Earth's surface plates and underlying mantle, generating lattice-preferred orientation (LPO) in olivine aggregates and a seismically anisotropic fabric. Because this fabric develops with the evolving mantle flow field, observations of seismic anisotropy can constrain asthenospheric flow patterns if the contribution of fossil lithospheric anisotropy is small. We use global viscous mantle flow models (developed using the CIG-supported CitcomS spherical convection code) to characterize the relationship between asthenospheric deformation and LPO, and compare the predicted pattern of anisotropy to a global compilation of observed shear-wave splitting measurements. For asthenosphere >500 km from plate boundaries, simple shear rotates the LPO toward the infinite strain axis (ISA, the LPO after infinite deformation) faster than the ISA changes along flow lines. Thus, we expect the ISA to approximate LPO throughout most of the asthenosphere, greatly simplifying LPO predictions because strain integration along flow lines is unnecessary. Approximating LPO with the ISA and assuming A-type fabric (olivine a-axis parallel to ISA), we find that mantle flow driven by both plate motions and mantle density heterogeneity successfully predicts oceanic anisotropy (avg. misfit = 13°). Continental anisotropy is less well fit (avg. misfit = 41°), but lateral variations in lithospheric thickness improve the fit in some continental areas. This suggests that asthenospheric anisotropy contributes to shearwave splitting for both continents and oceans, but is overlain by a stronger layer of lithospheric anisotropy for continents. The contribution of the oceanic lithosphere is likely smaller because it is thinner, younger and less deformed than its continental counterpart.

Combined Plate- & Density-Driven Flow ($\beta = 0.5$), Laterally-Varying Viscosity

A) Planform at 225 km

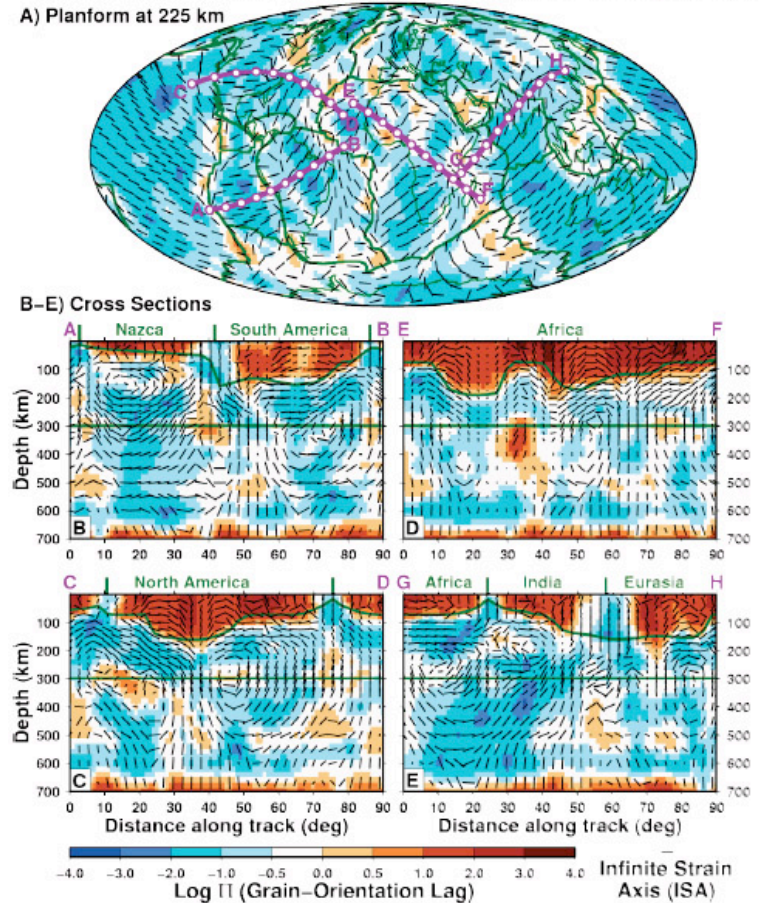


Figure 1. Map (a) and cross sections (b-d) of anisotropic fabric in the upper mantle, as predicted by the infinite strain axis (ISA, bars), which we computed using a global mantle flow model (CitcomS). Colors show the grain orientation lag parameter (Π), which compares the rate of LPO rotation away from the ISA direction to the rate of ISA formation. Wherever $\Pi < 0.5$, the ISA is a good approximation for LPO. This is true throughout most of asthenosphere, greatly simplifying the estimation of anisotropic fabric from a mantle flow model.

Note: our code for estimating ISA and Π is available: <http://www.soest.hawaii.edu/GG/FACULTY/conrad/mantleflow/mantleflow.html>

Reference

Conrad, C.P., M.D. Behn, and P.G. Silver (2007), Global mantle flow and the development of seismic anisotropy: Differences between the oceanic and continental upper mantle, *Journal of Geophysical Research*, 112, B07317, doi:10.1029/2006JB004608.

Influence of Dynamic Topography on Sea Level and its Rate of Change

Clinton P. Conrad, *University of Hawaii at Manoa, Honolulu, Hawaii, USA*
 Laurent Husson, *Université Rennes 1, CNRS, Rennes, France*

Mantle flow likely supports up to 2 km of long-wavelength topographic relief over the Earth's surface. Although the average of this dynamic support must be zero, a net deflection of the ocean basins can change their volume and induce sea level change. By calculating dynamic topography and the geoid (including self-gravitation effects) using a time-dependent global mantle flow model (the CIG-supported spherical convection code *CitcomS*), we find that continents preferentially conceal depressed topography associated with mantle downwelling (background field, Fig. 1E), leading to net seafloor uplift and $\sim 90 \pm 20$ m of positive sea level offset. Upwelling mantle flow is currently amplifying positive dynamic topography and causing up to 1.0 m/Myr of sea level rise, depending on mantle viscosity (Figs. 1A & 1C). Continental motions across dynamic topography gradients also affect sea level, but uncertainty over the plate motion reference frame permits sea level rise or fall by ± 0.3 m/Myr, depending on net lithosphere rotation (Figs. 1E & 1F). During a complete Wilson cycle, sea level should fall during supercontinent stability and rise during periods of dispersal as mantle flow pushes continents down dynamic topography gradients towards mantle downwellings. We estimate that up to ~ 1 m/Myr of sea level rise may have occurred during the most recent continental dispersal. Because this rate is comparable in magnitude to other primary sea level change mechanisms, dynamic offset of sea level by mantle flow should be considered a potentially significant contributor to long-term sea level change.

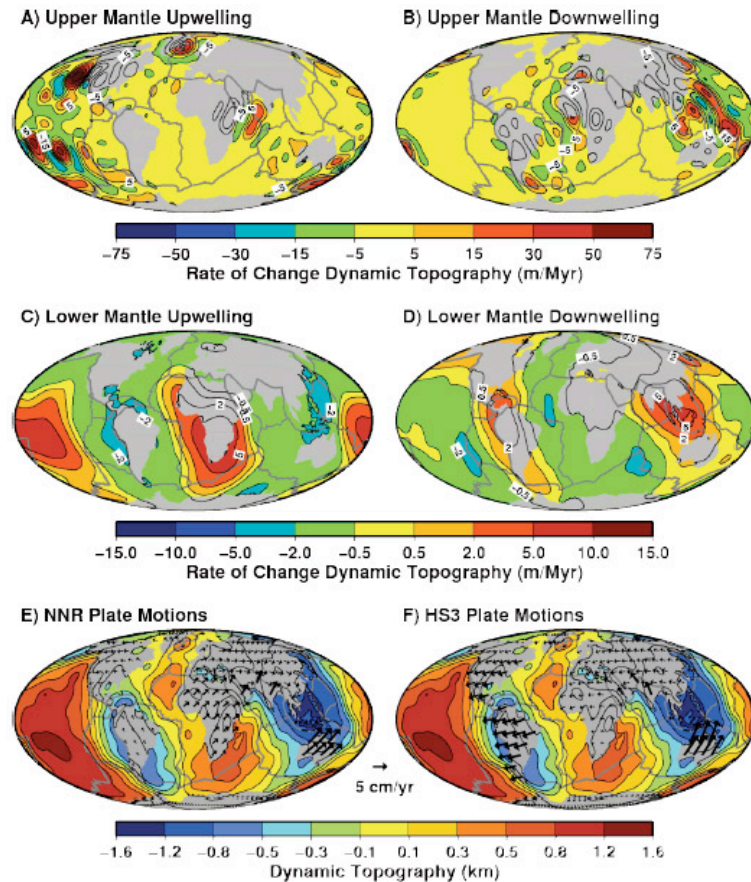


Figure 1. Rate of change of present-day dynamic topography determined from time-dependent mantle flow models driven by (A) negative and (B) positive density anomalies in upper mantle, and (D) negative and (E) positive density anomalies in the lower mantle. Thus, parts (B) and (D) show the time dependence of topography associated with active upwelling flow, while (B) and (D) are driven by downwelling flow. Sea level change is also caused by continental motions over the full dynamic topography field, as shown here for plate motions in the (E) no-net-rotation (NNR) and (F) HS3 reference frames.

Reference

Conrad, C. P., and L. Husson (2009), Influence of dynamic topography on sea level and its rate of change, *Lithosphere* 1(2), 110-120, doi:10.1130/L32.1.

Influence of Continental Roots and Asthenosphere on Plate-Mantle Coupling

Clinton P. Conrad, *University of Hawaii at Manoa*
Carolina Lithgow-Bertelloni, *University College London*

The shear tractions that mantle flow exerts on the base of Earth's lithosphere contribute to plate-driving forces and lithospheric stresses. We investigate the sensitivity of these tractions to sublithospheric viscosity variations by comparing shear tractions computed from a mantle flow model featuring laterally-varying lithosphere and asthenosphere viscosity with those from a model with layered viscosity. Lateral viscosity variations generally do not change the direction of shear tractions, but deeply penetrating continental roots increase traction magnitudes by a factor of 2-5 compared to 100 km thick lithosphere. A low-viscosity asthenosphere decreases traction magnitudes by a smaller amount, and is important only if >100 km thick. Increased plate-mantle coupling beneath thick continental lithosphere may increase plate-driving forces, surface deformation, and mantle-derived lithospheric stresses in these regions. By contrast, a low-viscosity asthenosphere does not decouple the lithosphere from mantle flow, highlighting the geological importance of mantle tractions on the lithosphere.

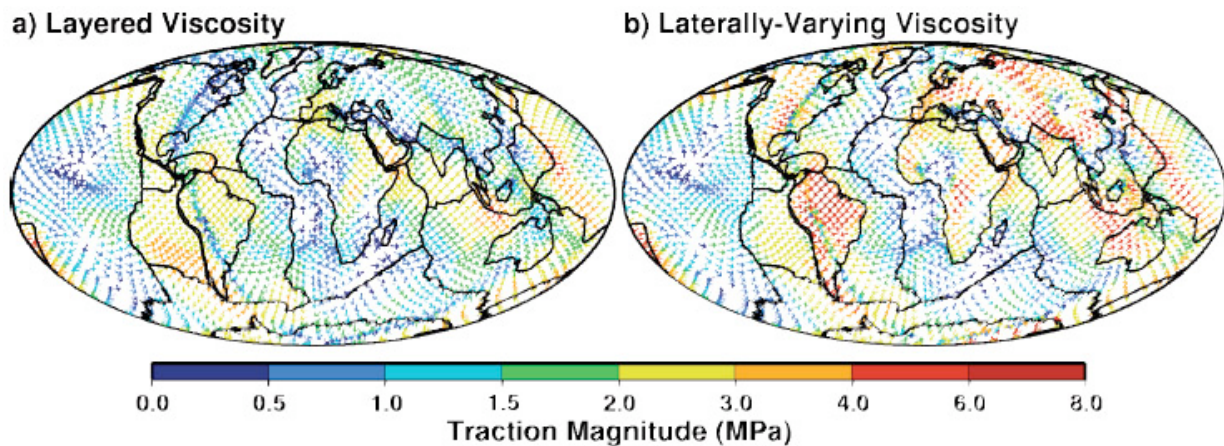


Figure 1. Shear tractions that mantle flow exerts on the base of the lithosphere, as computed using the CIG-supported spherical finite element code CitcomS. Shown are basal shear tractions for (a) a layered viscosity structure and (b) a viscosity structure that includes lateral variations in viscosity associated with lithospheric thickness variations (e.g., deeply-penetrating cratonic roots and thin lithosphere near oceanic ridges). Arrow directions and colors show shear traction azimuths and magnitudes, respectively. We found [Conrad & Lithgow-Bertelloni, 2006] that the magnitude of basal tractions is magnified beneath thick cratons by a factor of up to ~4, but the directions of these tractions are unaffected by the presence of cratons. The magnitude of these tractions, and their amplification beneath cratons, is important because the tractions are a primary driver of plate motions and can cause significant plate deformation at the surface.

Reference

Conrad, C. P., and C. Lithgow-Bertelloni (2007), Influence of continental roots and asthenosphere on plate-mantle coupling, *Geophysical Research Letters*, 33, L05312, doi:10.1029/2005GL025621.

History of the Australian region since the Cretaceous: Assimilation plate tectonic data into a regionally-globally coupled geodynamic model

Lydia DiCaprio^{1,2}, Michael Gurnis², R. Dietmar Müller¹, E. Tan³

¹ School of Geosciences, The University of Sydney, Australia

² Seismological Laboratory, California Institute of Technology, Pasadena, CA

³ CIG, California Institute of Technology, Pasadena, CA

Australia experienced first order, broad-scale vertical motions since the Cretaceous that were likely related to the horizontal motion of the continent over slabs (DiCaprio, et al., 2009). To more closely link the geological evolution of the continent over the mantle, we developed a new method based on a plate tectonic system and a model of mantle convection. First, we assimilated realistic boundary conditions: Plate kinematics, the evolving ages of oceanic plates, the lithospheric structure of continents, low viscosity within mantle wedges, and large-scale geochemical domains. Second, to provide the requisite high resolutions needed for the previous data sets, we used high-resolution regional models that were coupled into a low-resolution global model using framework-based CitcomS solvers (Tan, et al., 2006). We investigated the passage of subducted material beneath the South West Pacific since 140 Ma. These multi-scale resolution models use the deformation field of the global model as the boundary condition on the embedded solver which provides more natural boundary conditions on the regional solver than reflecting or periodic boundary conditions. We constrain the layered viscosity and initial conditions of the model to match geologic observations of dynamic topography (DiCaprio, et al., 2009) and seismic tomography. Our preferred model reproduces the expected tilt of the Australian continent as it approaches the subduction realm in South East Asia. The passage of the slab satisfies geological observations and predicts patterns of inundation and uplift across the Australian continent from 140 Ma to present.

We use the finite element package CitcomS Version 2.2, with coupled solvers, particle tracers and global mantle flow available from the Computational Infrastructure for Geodynamics (CIG).

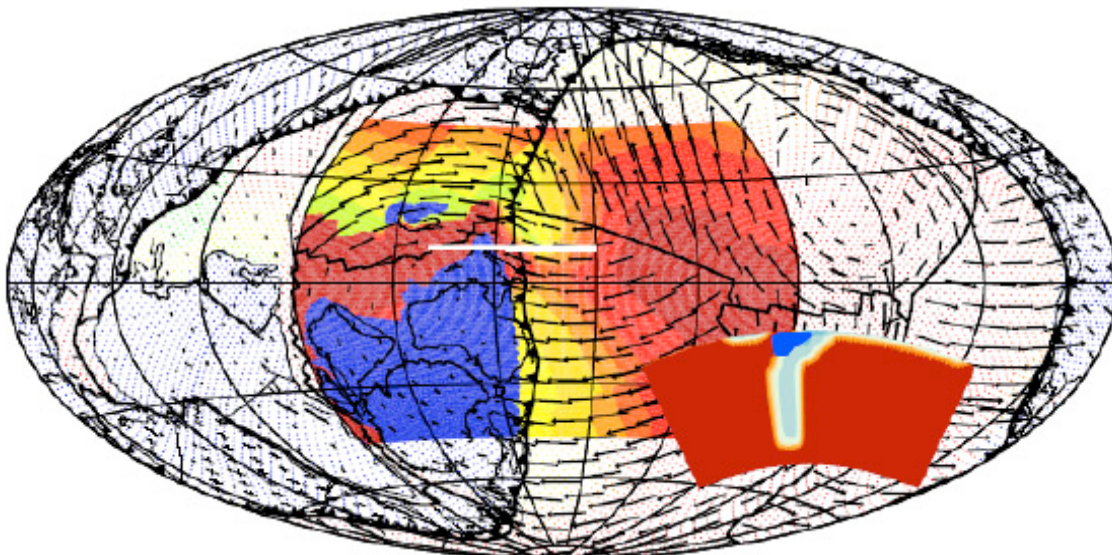


Figure 1: The assimilation of data into multiscale geodynamic models includes lithospheric age (colored background), plate velocity (vectors) and an initial subducting slab (inset) with a low viscosity mantle wedge (dark blue) and buoyant continents.

References

- DiCaprio, L., M. Gurnis, and D. Müller, (2009), Long-wavelength tilting of the Australian continent since the Late Cretaceous: *Earth and Planetary Science Letters*, 278, p. 175-185, doi:10.1016/j.epsl.2008.11.030.
- Tan, E., E. Choi, P. Thoutireddy, M. Gurnis, and M. Aivazis, (2006), GeoFramework: Coupling multiple models of mantle convection within a computational framework: *Geochemistry, Geophysics, Geosystems* 7, Q06001, doi:10.1029/2005GC001155.

Generation of Plate Tectonics and Mantle Heterogeneity from a Spherical, Visco-plastic Convection Model

Bradford J. Foley and Thorsten W. Becker, *University of Southern California*

How plate tectonics arises from mantle convection is a question that has only very recently become feasible to address with spherical, visco-plastic computations. We used CitcomS to compute convection simulations with temperature-dependent viscosity, a plastic yield stress, and varying heating modes. This rheology has been shown to be effective in producing some key features of plate tectonics in 3-D Cartesian geometry: a rigid surface forms, with deformation localized in narrow zones; downwellings are sheet-like; and surface motions are coherent and uniform across ‘plates.’ We explore the Rayleigh number (Ra) - yield stress (σ_y) phase space, and the effects of depth-dependent σ_y , bottom heating, and a low viscosity asthenosphere.

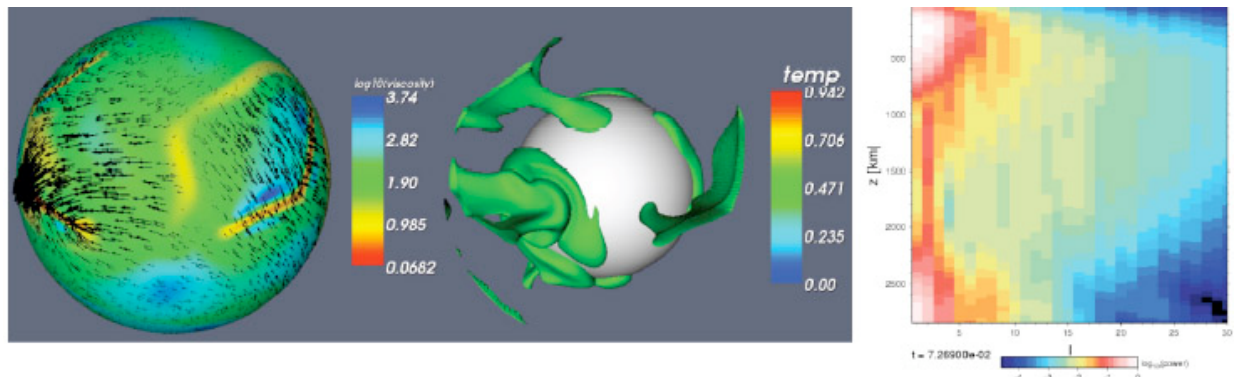


Figure: Images of the surface viscosity field, with velocity vectors (left), cold isosurface showing downwellings (center), and a temperature power spectrum (right) showing a strong degree two signature.

We find that visco-plastic convection in spherical geometry produces these same, plate-like features. Additionally, the convective planform and toroidal-poloidal velocity field ratio (TPR) are affected by near-surface viscosity variations. Toroidal motion is important in the Earth, comprising approximately half of the surface velocity field. We found that models that maximize lateral viscosity contrasts (i.e., have a strong surface and numerous weak zones). We observe TPR values near 0.5 for models with high Ra . Cartesian models tend to form very long wavelength convective planforms. Our models favor spherical harmonic degree one convection though models with a weaker surface viscosity form degree two patterns and reproduce tomographically observed power spectra. Furthermore, the depth-dependent σ_y causes convection to favor a degree two pattern. So for appropriate parameter ranges, these models approximately reproduce observations of Earth’s convective wavelength and toroidal-poloidal velocity field partitioning.

An asthenospheric viscosity reduction improves plate-like nature, as expected. Bottom heating produces strong plumes that tend to destroy plates at the surface, implying that significant internal heating may be required, both to reduce the role of active upwellings and to form a low viscosity zone beneath the upper boundary layer.

Reference

Foley, B. J. and T. W. Becker, Generation of Plate Tectonics and Mantle Heterogeneity from a Spherical, Visco-plastic Convection Model, *Geochem. Geophys. Geosys.* MS#2009GC002387, Submitted.

Implications of lower mantle structural heterogeneity for existence and nature of whole mantle plumes

Ed Garnero and Allen McNamara, *Arizona State University*
Thorne Lay, *University of California, Santa Cruz*

Recent seismological studies demonstrate the presence of strong deep mantle elastic heterogeneity and anisotropy, consistent with vigorous convection in an environment having chemical anomalies, phase changes, and partially molten material. The implications for deep mantle plume genesis are discussed in the light of the diverse seismological findings. Nearly antipodal large low shear velocity provinces (LLSVPs) beneath the Pacific Ocean and Africa are circumscribed by regions of subduction, suggestive of whole mantle circulation. The LLSVPs have sharp boundaries, low V_s/V_p ratios, and high density; thus, they appear to be chemically distinct structures. Elevated temperature in LLSVPs may result in partial melting, possibly accounting for the presence of ultra-low velocity zones detected at the base of some regions of LLSVPs. Patterns in deep mantle fast shear wave polarization directions within the LLSVP beneath the Pacific are consistent with strong lateral gradients in flow direction. The thermal boundary layer at the base of the mantle is a likely location for thermal instabilities that form plumes, but geodynamical studies show that the distribution of upwellings is affected when piles of dense chemical heterogeneities are present. The location of lowermost mantle plume upwellings is predicted to be near the boundaries of the large thermochemical complexes comprising LLSVPs. These observations suggest that any whole mantle plumes are likely to be preferentially generated in regions of distinct mantle chemistry, with non-uniform spatial distribution. This plausibly accounts for some attributes of major hot-spot volcanism.

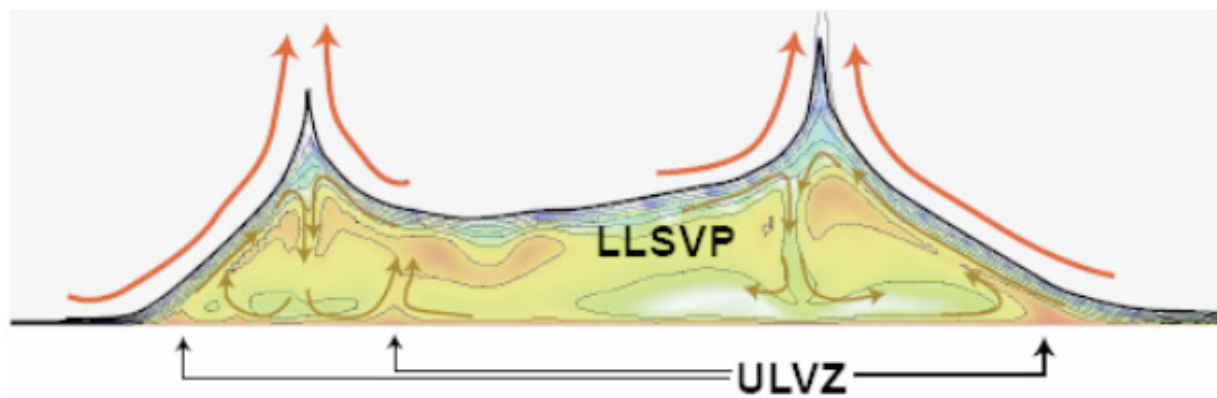


Figure: A cross-section of the temperature field of a thermochemical pile, modeled using CitcomS, beneath the Pacific Ocean. Convective motions are indicated by the arrows. The hottest zones may invoke partial melt of LLSVP material, either at the CMB (denoted as ULVZ in the figure), or in some isolated locations further up within the LLSVP.

Reference

Garnero, E.J., T. Lay, and A.K. McNamara (2007), Implications of lower mantle structural heterogeneity for existence and nature of whole mantle plumes, in *Plates, Plumes, and Planetary Processes*, editors: G.R. Foulger and D.M. Jurdy, GSA Special Paper 430.

Effect of lateral viscosity variations on mantle flow and the geoid

Attreyee Ghosh and Thorsten Becker, *Dept. of Earth Sciences, University of Southern California*
Shijie Zhong, *Dept of Physics, University of Colorado, Boulder*

We address the long-standing question of how lateral viscosity variations in the mantle such as due to presence of stiff slabs, affect the geoid. The long wavelength geoid is sensitive to the radial viscosity distribution within the Earth and an increase in viscosity, usually placed at the upper-lower mantle boundary at 660 km, is required to explain the long wavelength geoid. However, effects of lateral viscosity variations (LVVs) on the geoid are still not clearly understood. We are motivated by the findings of Zhong & Davies (1999) who found that introducing stiff slabs in the lower mantle degrades the fit to the Earth's long wavelength geoid compared to a model with only radial viscosity variations. This would indicate that slabs in the lower mantle are of the same strength as the ambient mantle, which is somewhat contrary to expectations. Moucha et al. (2007), however, recently argued that lateral viscosity variations inferred from seismic tomography have a minor effect on the geoid. We re-investigate the problem by computing the geoid in the presence of rheological complexity using the high-resolution finite element mantle convection code, CitcomS. We use different models of slab and density anomalies in the mantle, and vary slab strength, temperature-dependent viscosity, and background layer viscosity profiles in a consistent way. We test different slab viscosities and compute the correlation with the observed geoid, striving to test which description of slab dynamics, and mantle rheology, is consistent with observations. As seen in previous studies, we find that presence of LVVs worsen the fit to the observed geoid for slab models, whereas the geoid from tomography models are robust to the changes in LVV. We attribute this effect to the differences in the two types of density models and the sensitivity of the geoid on those differences.

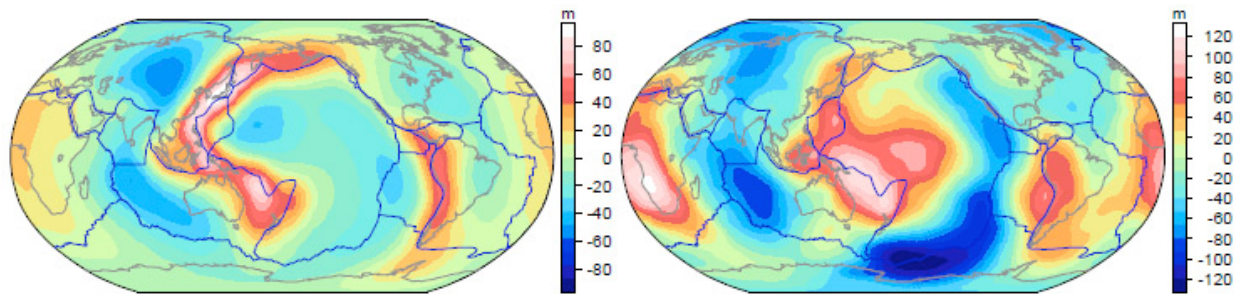


Figure 1. Predicted geoid from slab model (left) and tomography model (right) with strong LVVs.

References

- Ghosh, A., T. W. Becker, and S. Zhong (2008), Effect of lateral viscosity variations on mantle flow and the geoid, *EOS Trans. AGU*, 89(53), Fall Meet. Suppl.
- Moucha, R., A. Forte, J. Mitrovica, and A. Daradich (2007), Lateral variations in mantle rheology: implications for convection related surface observables and inferred viscosity models, *Geophys. J. Int.*, 169, 113-135.
- Zhong, S., and G. Davies (1999), Effects of plate and slab viscosities on the geoid, *Earth and Planet. Sci. Lett.*, 170, 487-496.

Three-dimensional mantle convection simulations with a low-viscosity asthenosphere

Tobias Höink and Adrian Lenardic, *Department of Earth Science, Rice University*

We have used CitcomCU to perform three-dimensional, mixed heating mantle convection simulations with a thin low-viscosity channel for a range of aspect ratios to test whether a thin, submerged low-viscosity channel, an analog to the asthenosphere, (1) allows for flow channelization, (2) decreases lateral dissipation and (3) enables long wavelength convection (Höink and Lenardic, GRL 2008).

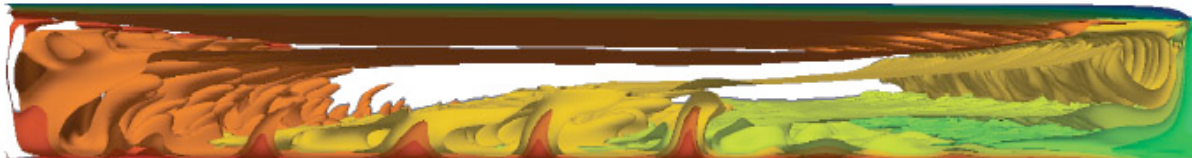


Figure: Temperature isosurfaces. Note the elongated convection cell with a broad upwelling on the left, a thin downwelling on the right. Thermal instabilities arising from the base are unable to disrupt the large scale flow.

For reasonable viscosity contrasts between lithosphere, asthenosphere and bulk mantle we find that very large aspect ratios can develop. Velocity profiles quantify the degree of channelization for various aspect ratios. Internal temperatures are found to decrease with aspect ratio and both surface heat flux and velocity are found to increase with aspect ratio. Our results are consistent with the idea that the asthenosphere channels lateral mantle flow which, in turn, stabilizes long wavelength convection cells and makes long wavelength flow energetically favorable. The extension of this work to larger wavelengths (we find stable convection cells up to aspect ratio 32) shows that mantle flow in the lithosphere-asthenosphere region is a Poiseuille-Couette flow, suggesting that velocity amplitudes in the asthenosphere can exceed surface velocities (Höink and Lenardic, in prep). Our simulations predict preferentially localized fabric development and seismic anisotropy, and they suggest that a strong pressure driven flow can exist in the asthenosphere independent of mantle plumes. The regime crossover depends on the relative thicknesses of compositional and thermal boundary layers. Additional simulations with temperature- and yield-stress dependent viscosity show consistent behavior and further suggest that the regime crossover is also associated with a change between regimes with relative large versus small energy dissipation at plate margins.

Reference

Höink T., and A. Lenardic (2008), Three-dimensional mantle convection simulations with a low viscosity asthenosphere and the relationship between heat flow and the horizontal length scale of convection, *Geophys. Res. Lett.* 35, L10304, doi:10.1029/2008GL033854.

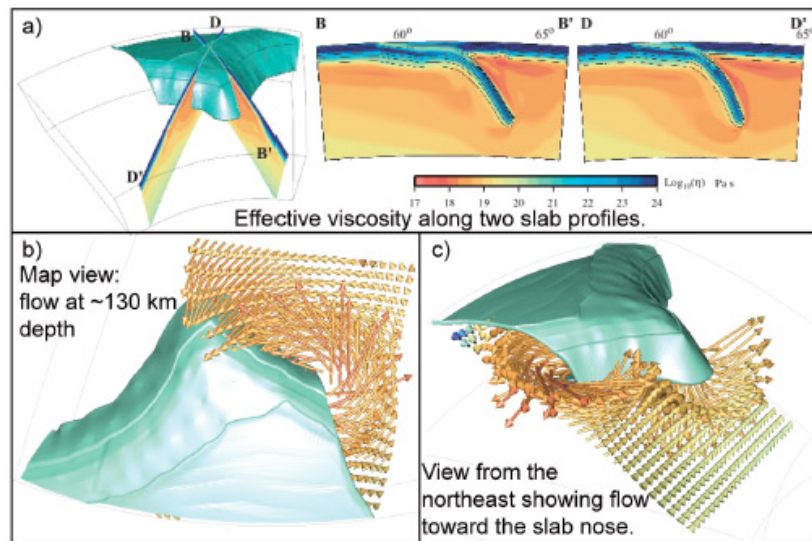
Mantle Flow at a Subduction-Transform Plate Boundary

Margarete Jadamec and Magali Billen, *Dept. of Geology, University of California, Davis*

Using high-resolution, instantaneous 3D viscous deformation models run with *CitcomCU*, we constrain how Neogene deformation in southern Alaska is linked to the subducted Pacific slab in the subsurface. The slab thermal structure incorporates the plate age at the time of subduction and the thermal structure of the overriding North American plate is constrained by heat flow and seismic observations of crust and lithosphere thickness (Fig. 1a). The model rheology is a composite dislocation-diffusion creep viscosity with a depth-dependent plastic yield stress. Plate boundaries are modeled as low viscosity shear zones.

We compare the mantle flow and surface deformation for two end-member slab shapes to observations of shear-wave splitting in the mantle, the surface distribution of volcanism and dynamic topography, and plate motions. We find that a slab shape missing the northwest extension of the slab from 100-300 km depth, as constrained by seismicity and seismic tomography, is more consistent with the entire suite of observations, than a model that includes this portion of the slab, as would be predicted based only on past plate motions. We also find that models with only a Newtonian mantle viscosity (diffusion creep) have a significantly different flow field and surface deformation than models using the non-Newtonian composite viscosity.

Figure 1. Slab Structure and Flow Field. (a) 3D view of slab shape indicating location of two viscosity slices along slab-perpendicular arcs, BB' (beneath the Wrangell Volcanics) and DD' (beneath Mt. Denali). (b) Map view of flow at approximately 100 km depth. (c) View, from the northeast, of flow around the slab edge.



For both slab shapes, the resulting flow exhibits the typical 2D corner-flow pattern away from the slab edge, with flow being drawn into the wedge corner and upwelling beneath the fore-arc. A 3D map view of flow field at a depth of 130 km, for the full-slab shape, shows a strong component of along-slab flow towards the *nose* of the slab (Fig. 1b, c). This flow is driven by the pressure-difference between the regions beneath and above the slab which draws flow around the slab edge, and the increased mass in the slab nose, which further draws this flow along the slab.

Reference

Jadamec, M. A. (2008), 3D Numerical Models of Lithosphere and Mantle Deformation in southern Alaska, Ph.D. thesis, University of California, Davis.

More Thoughts on Tharsis Rise Mars and Small-Scale Convection

Scott D. King, *Department of Geosciences, Virginia Tech, Blacksburg, VA*

Using CitcomS, a series of 3D spherical incompressible convection calculations with strong temperature-dependent rheology and a step increase in viscosity in the lithosphere over one hemisphere are used to understand convection on a planet with a hemisphere step in the lithosphere structure, which may represent the hemispheric dichotomy on Mars. The calculations start from a uniform hot mantle and the flow is followed for one billion years. There is a significant difference in the convective plan form of the two hemispheres. The thick hemisphere has a simple upwelling plume structure while the thinner hemisphere has time-dependent, short-wavelength structure below the lithosphere.

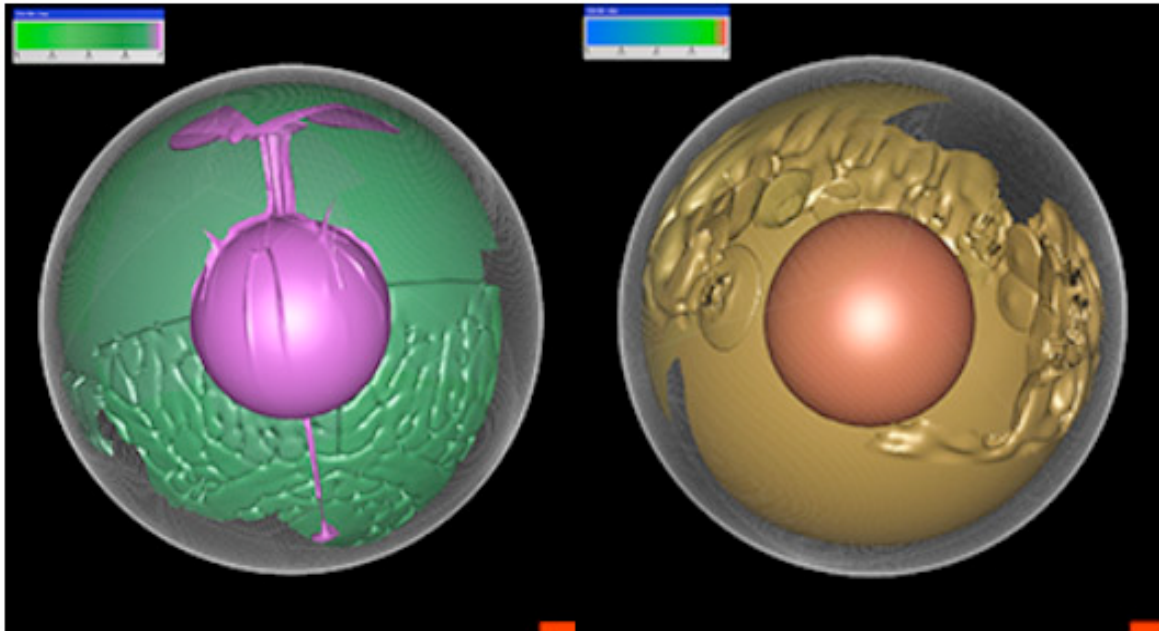


Figure 1: (left) Spherical temperature-dependent convection with a hemispherical near-surface lithosphere thickness variation of 250 km. The green surface is a temperature (0.90) isosurface just below the lithosphere. The smooth hemisphere is the thick lithosphere hemisphere and the rougher surface is the thinner lithosphere hemisphere. Two stable plumes have developed, one large plume beneath the thick hemisphere and a weak plume beneath the thin hemisphere; (right) Same as the calculation on the left with the inclusion of a low viscosity channel beneath the lithosphere. The calculation is approximately 100 m.y. after the initial uniform hot interior. The gold surface is a temperature isosurface just below the lithosphere. No plumes have developed and small-scale convection occurs at the lithospheric step boundary.

In contrast to the stable plume model (left), with a low-viscosity channel below the lithosphere small-scale convection develops along the lithospheric step within the first 100 million years (right). I am in the process of mapping out the parameters necessary for this mode of small-scale convection, addressing the time scale and whether it can generate enough melt to produce the Tharsis volcanic province.

There are several possible explanations for why only part of the dichotomy boundary had extensive volcanism. The mantle may have had an anomalously hot region beneath the area that becomes the Tharsis swell. Alternatively, the geometry of the dichotomy may have favored that region over others. Finally, there may have been anomalous lithospheric structure that favored edge driven convection beneath Tharsis. These ideas will be explored with further computational experiments.

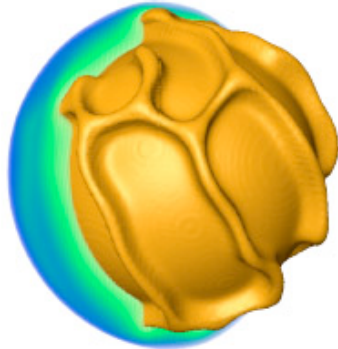
Reference

King, S.D. (2009), Mars Mantle Structure: Results from Calculations with an Imposed Hemispheric Lithosphere Step, *LPSC XL*.

Unusual Pattern of Convection in a Thin Mantle Shell and the Connection to Tectonics on Mercury

Scott D. King, *Dept. of Geosciences, Virginia Tech, Blacksburg, VA*

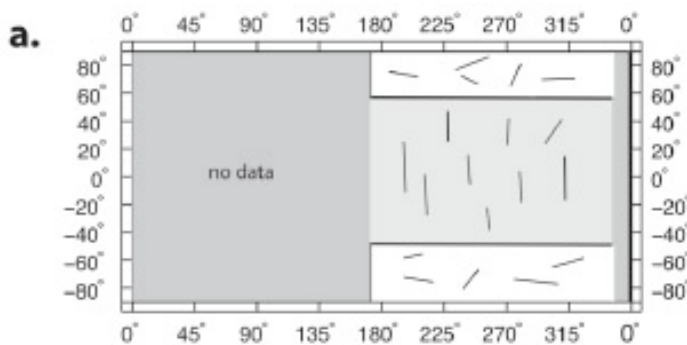
Calculations of convection in a 3D spherical-shell geometry with temperature-dependent rheology and a cooling-core boundary condition applicable to Mercury's silicate mantle using CitcomS show an unusual pattern of convection. Regularly-spaced, linear upwellings are the characteristic planform of mantle convection in a thin spherical shell and, this differs significantly from the cylindrical upwellings seen in similar calculations for Earth, Venus, and Mars mantle geometries (Figure 1).



Linear rolls with a wavelength approximately two to three times the thickness of the shell are observed in the low latitude region. Near the poles the linear roll planform breaks down into a nearly hexagonal pattern, with a wavelength nearly equal to the thickness of the shell. This planform is consistent with the pattern of compressive features observed in the hemisphere imaged by Mariner 10 (Figure 2) suggesting that the compressive features record an ancient pattern of mantle convection. This pattern of convection may be observable in the gravity and topographic data returned from the upcoming MESSENGER mission.

Figure 1: Temperature field after 750 million years of model evolution in a 2400 km radius sphere with an 1800 km radius core. The orange surface represents the 0.9 (1804 K) temperature isosurface. Note the transition between long, two-dimensional roll structures in the low latitudes to a more complicated hexagonal pattern in the high latitude.

The linear roll planform develops over a period of 300-500 million years. The planform of convection explains the orientation and timing of the compressive features, which would be random and continuous throughout the early history of Mercury if they were the result of contraction due to cooling alone. The



stresses due to convection are order 500 MPa and when coupled with a global compressive stress field due to contraction of the same magnitude (necessary to offset the extensional stresses due to convection because extensional features are not observed outside Caloris basin) are sufficient to produce thrust faults that extend to depths of 25 km on Mercury, consistent with modeling of Discovery Rupes.

Figure 2: Schematic diagram of orientation of compressive features on Mercury's surface from Mariner 10 imagery (after Watters et al., 2004).

Reference

King, S. D. (2007), Pattern of Lobate Scarps on Mercury's Surface Reproduced by a Model of Mantle Convection, *Nature Geosciences* 1, 229-232.

Simultaneous inversion of mantle properties and initial conditions using an adjoint of mantle convection

Lijun Liu and Michael Gurnis, *Seismological Laboratory, California Institute of Technology*

Through the assimilation of present day mantle seismic structure, adjoint methods can be used to constrain the structure of the mantle at earlier times. However, the application to geophysical problems is restricted through both the high computational expense from repeated iteration between forward and adjoint models and the need to know mantle properties (such as viscosity and the absolute magnitude of temperature or density) a priori. We propose that an optimal first guess to the initial condition can be obtained through a simple backward integration (SBI) of the governing equations thus lessening the computational expense.

Mantle viscosity and the effective Rayleigh number are crucial for mantle convection models, neither of which is exactly known. We place additional constraints on these basic mantle properties when the convection-induced dynamic topography on Earth's surface is considered within an adjoint inverse method. We considered both one-layer and two-layer viscosity in regional models. For the one layer model, the magnitude of dynamic topography is controlled by the temperature scaling while the rate of change of topography is controlled by the absolute value of viscosity. For the two-layer case, the rate of change of topography constrains upper mantle viscosity, while the magnitude of dynamic topography determines the temperature scaling (lower mantle viscosity) when upper-mantle (lower-mantle) density anomaly dominates the flow field. For both cases, we show that the theory can constrain mantle properties with errors arising through the adjoint recovery of the initial condition. The adjoint algorithm was created by modifying CitcomS Version 2.0, obtained from the Computational Infrastructure for Geodynamics (CIG).

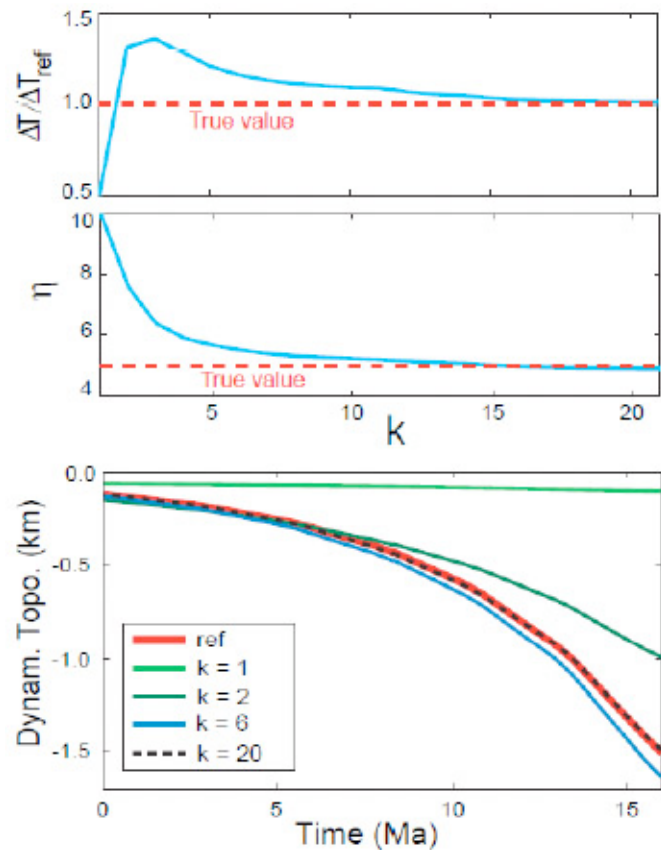


Figure (right) shows the dynamic topography constraints on mantle viscosity and density anomaly for a 1-layer viscosity mantle, where k represents the inverse iteration.

Reference

Liu, L., and M. Gurnis (2008), Simultaneous inversion of mantle properties and initial conditions using an adjoint of mantle convection, *Journal of Geophysical Research*, 113, B08405, doi:10.1029/2008JB005594.

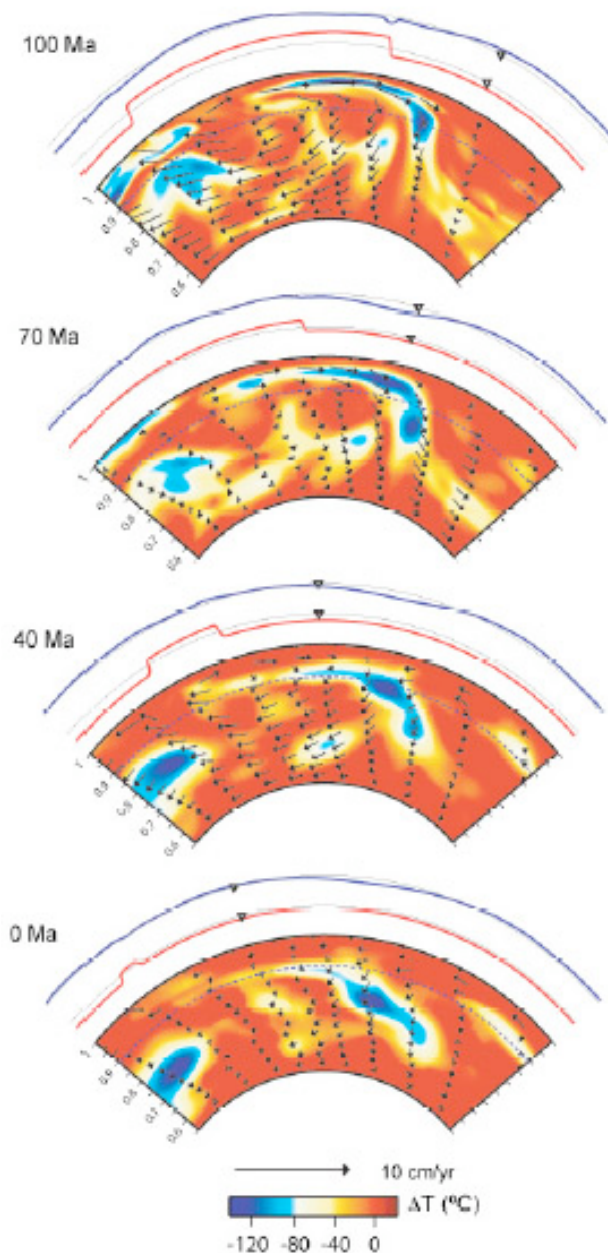
Reconstructing Farallon Plate Subduction beneath North America back to the Late Cretaceous

Lijun Liu, Sonja Spasojević and Michael Gurnis, *Seismological Laboratory, California Institute of Technology*

Using an adjoint mantle convection model (*CitcomS*) that assimilates global seismic tomography and plate motions, we reconstruct the subduction of the Farallon plate beneath North America back to 100 Ma [Liu et al., 2008]. The associated surface dynamic topographies allow reproduction of paleoshorelines, sediment isopachs and tectonic borehole subsidence, whose spatial and temporal evolution constrains the depth dependence of mantle viscosity and buoyancy. Our best model has an upper mantle viscosity of $1 \cdot 10^{21}$ Pa s, a lower mantle $1.5 \cdot 10^{22}$ Pa s and an effective temperature anomaly associated with present day Farallon remnants of 160 °C.

In our preferred model that satisfies stratigraphy, the Farallon slab was flat lying in the Late Cretaceous (Figure). Furthermore, we find an extensive zone of shallow dipping subduction that extends beyond the flat-lying slab further east and much further north (by up to 1000 km) than previously inferred, implying a much broader region of Cretaceous subsidence over the North American craton. Following the demise of flat lying subduction, the models are consistent with the flat lying segment moving vertically in the mantle. The limited, along-strike region of flat lying subduction is consistent with subduction of an oceanic-plateau. The results imply that seismic images of the mantle provide more powerful constraints on tectonic events than previously recognized. For the adjoint models, we modified Version 2.0 of *CitcomS* that we obtained from CIG. Details are in Liu and Gurnis [2008].

Figure (right). Cross section of effective temperature at 41°N with velocity (east-west component) in red and dynamic topography in blue.



References

- Liu, L., and M. Gurnis (2008), Simultaneous inversion of mantle properties and initial conditions using an adjoint of mantle convection, *Journal of Geophysical Research*, 113, B08405, doi:10.1029/2008JB005594.
- Liu, L., S. Spasojević, and M. Gurnis (2008), Reconstructing Farallon plate subduction beneath North America back to the Late Cretaceous, *Science* 322, 934-938, doi:10.1126/science.1162921.

Reconstructing of Flat Slab Subduction and Detachment beneath Central Mexico

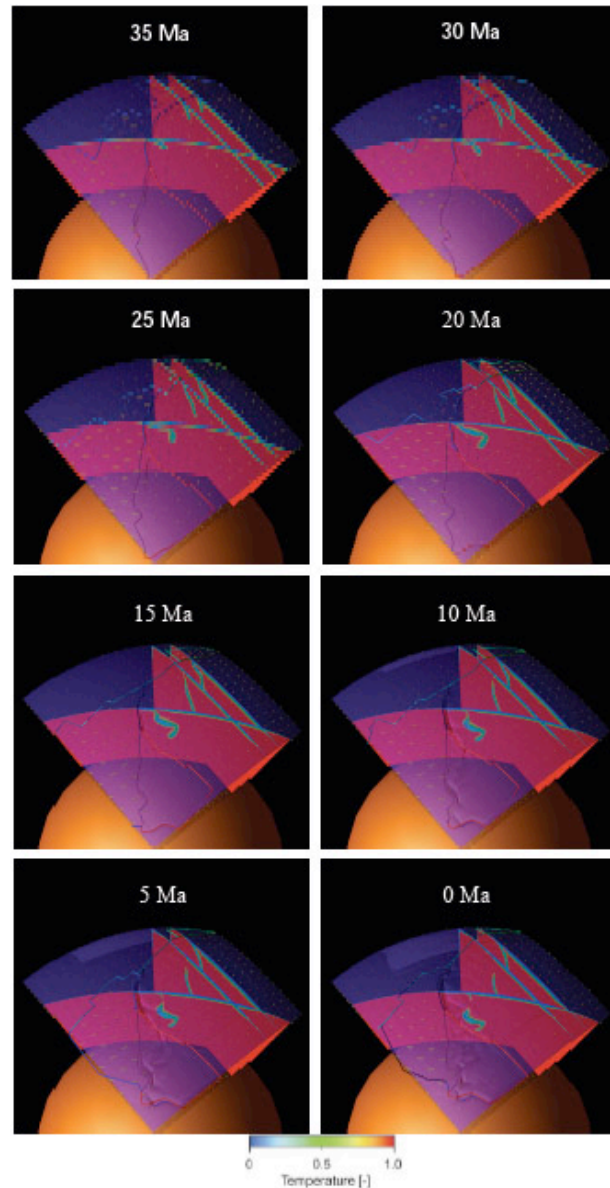
Vlad Manea^{1,2} and Michael Gurnis²

¹ Computational Geodynamics Laboratory, Centro de Geociencias, Juriquilla, UNAM, Mexico

² Seismological Laboratory, California Institute of Technology, Pasadena, CA

Recent tomographic images beneath Central Mexico revealed a perfectly flat slab segment extending several hundreds of km inland [Perez-Campos et al., 2008]. Also, the flat slab is not in direct contact with the overlying crust, and a low velocity layer decouples the two plates. Here we present a 3D geodynamic model tailored to realistic paleo-reconstruction back to 35 Ma. Using a tracer technique described in details by Manea and Gurnis [2007], the models incorporate a low viscosity wedge and channel down to 300 km. Time-dependent dynamic models are solved using the finite element package *CitcomS* from CIG. The computations are performed within a spherical domain ($r=1300$ km, $\theta=57^\circ$, $\varphi=57^\circ$). The position of plate boundaries is imposed and set using the *GPLates* software. The modeling results show that the subduction system in Central Mexico entered into flat slab regime at ~ 15 Ma. Later, at ~ 10 Ma, the slab started to break off and by ~ 5 Ma is completely detached. In Central Mexico the propagation of slab detachment is expressed by a short (2–3 Myr), eastward-migrating pulse of mafic volcanism that took place from ca. 11.5 to ca. 5 Ma to the North of the present Trans-Mexican Volcanic Belt [Ferrari, 2004]. The onset of flat slab (from volcanic rock dating, Ferrari et al., 1999) took place 17–12 Ma. Our models predict both, the onset of flat slab around 15 Ma and the slab detachment at ~ 10 Ma.

Figure. Temperature evolution and the onset of flat slab (~ 15 Ma) and slab detachment (~ 10 Ma) in Central Mexico.



References

- Ferrari, L., López-Martínez, M., Aquirre-Díaz, G., and Carrasco-Núñez, G. (1999), Space-time patterns of Cenozoic arc volcanism in central México: from the Sierra Madre Occidental to the Mexican Volcanic Belt. *Geology* 27(4), 303-306.
- Ferrari, L. (2004), Slab detachment control on mafic volcanic pulse and mantle heterogeneity in central Mexico, *Geology* 32(1), 77-80.
- Manea, V.C., and Gurnis, M. (2007), Subduction zone evolution and low viscosity wedges and channels, *Earth and Planetary Science Letters* 264(1-2), 22-45.
- Pérez-Campos, Xyoli, YoungHee Kim, Allan Husker, Paul M. Davis, Robert W. Clayton, Arturo Iglesias, Javier F. Pacheco, Shri K. Singh, Vlad Manea, and Michael Gurnis (2008), Flat Slab Subduction in the Vicinity of Mexico City, *Geophysical Research Letter*, doi:10.1029/2008GL035127.

Body Tides of a Convecting, Laterally Heterogeneous, and Aspherical Earth

Laurent Métivier, *Institut Géographique National, Paris, France*

Clinton P. Conrad, *University of Hawaii at Manoa, Honolulu, Hawaii*

Precise knowledge of Earth's body tides is crucial for correcting geodetic positioning measurements, satellite gravity surveys, and superconducting gravimeters with nanogal (nGal) precision. With this aim, body tides are generally computed assuming a radially (or elliptically) stratified Earth. However, seismic tomography surveys and fluid dynamic studies show that thermal convection within Earth's mantle produces significant lateral heterogeneity exemplified by superplumes, superswells, and subducting slabs. To determine the influence of this heterogeneity on body tides, we used a tomographic model to constrain lateral variations in mantle density and rigidity. This heterogeneity drives convective flow that deflects Earth's surface and core-mantle boundaries by a few kilometers; we used a viscous flow model (the CIG-supported spherical convection code *CitcomS*) to constrain this dynamically supported asphericity. After verifying this complete Earth model using geoid observations, we used the spectral element method to determine how Earth's body tides are perturbed compared to a spherical Earth. We find maximum radial perturbations of surface and geoid displacements of 0.3 and 0.1 mm, respectively, and tidal gravity variations of 150 nGal. The amplitude of tidal gravity perturbations depends strongly on location and is greatest above large mantle density anomalies: e.g., large dense slabs (South America, Indonesia, Marianas), hot spots (Hawaii, Iceland), and the East African Rift. Predicted gravity perturbations are 100 times larger than the present precision of superconducting gravimeters and are comparable in magnitude to the unexplained residue observed at some gravimeter stations after tidal corrections. While this residue has been attributed to unmodeled loading from ocean tides, body tide perturbations caused by convection-induced mantle heterogeneity may contribute to this observed residue.

Reference

Métivier, L., and C.P. Conrad (2008), Body tides of a convecting, laterally heterogeneous, and aspherical Earth, *J. Geophys. Res.*, *113*, B11405, doi:10.1029/2007JB005448.

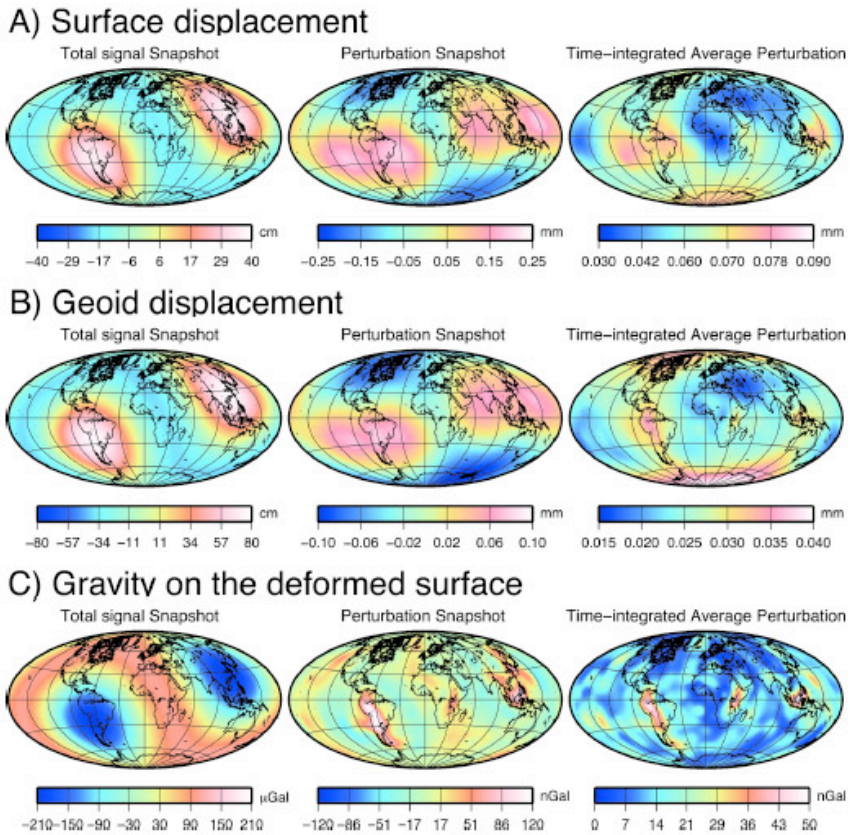


Figure 1. a) Surface displacements, b) geoid displacements, and c) gravity variations induced by the tide-generating potential on a given date or integrated over time. Left: Maps of the tidal responses for the PREM Earth model, on 23 November 2007 at 1800 UTC. Middle: Maps of additional tidal perturbations (on the same date) that are due to lateral heterogeneities in the mantle and to topographies on the surface and on the CMB, as calculated using the CIG-supported *CitcomS* code. Right: Maps of the mean integration of the perturbations over 1 year.

Giant impacts on early Mars and the cessation of the Martian dynamo

James H. Roberts¹, Robert J. Lillis², Michael Manga²

¹Johns Hopkins University Applied Physics Laboratory, ²University of California, Berkeley

Although Mars currently has no global dynamo-driven magnetic field, widespread crustal magnetization provides strong evidence that such a field existed in the past. The absence of magnetization in the younger large Noachian basins suggests that a dynamo operated early in Martian history, but stopped in the mid-Noachian. Within a 100 Ma period, 15 giant impacts occurred coincident with the disappearance of the global magnetic field.

Here we investigate a possible causal link between the giant impacts during the early and mid-Noachian and the cessation of the Martian dynamo at about the same time. We developed three-dimensional spherical mantle convection models including internal heating from giant impacts by modifying CitcomS version 3.0.2, obtained from the Computational Infrastructure for Geodynamics (CIG). We find that impact heating associated with the largest basins (diameters > 2500 km) can cause the global heat flow at the core-mantle boundary to decrease significantly (10-40%; see Fig. 1). We suggest that such a reduction in core heat flow may have led to the cessation of the Martian dynamo.

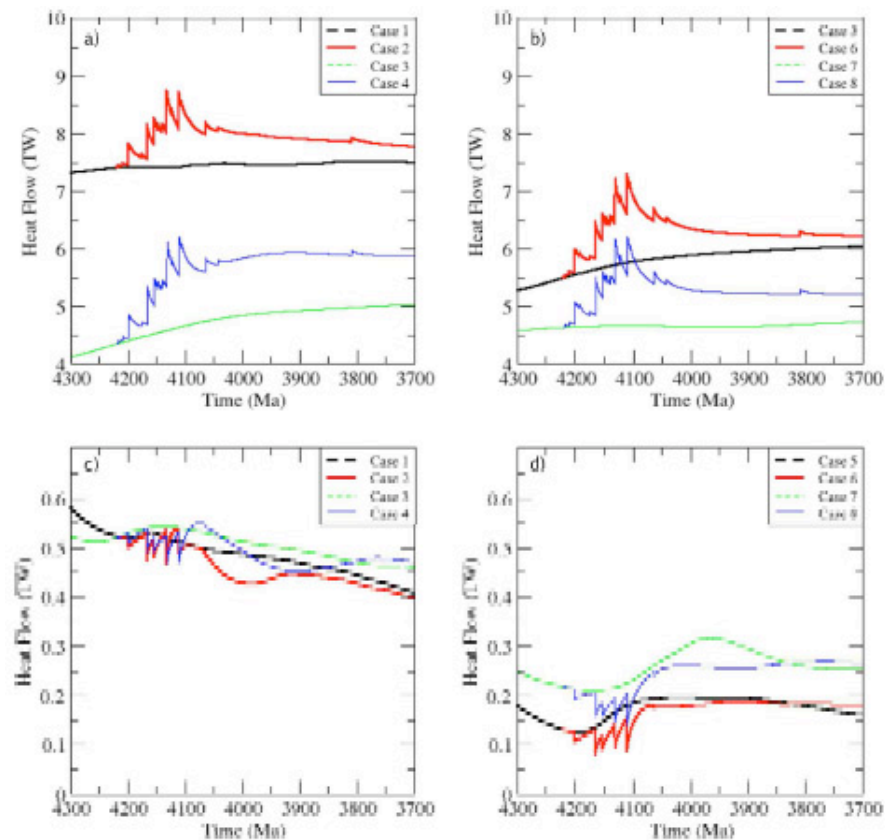


Figure 1: Total global heat flow at the surface (a-b) and CMB (c-d) vs. time for cases 1-4 with $Ra = 3.05 * 10^7$ (a,c) and cases 5-8 with $Ra = 6.1 * 10^6$ (b,d). Each impact causes a strong perturbation to the surface heat flow. Relatively little heat is deposited at large depths. Only impactors forming basins > 2500 km in diameter cause a significant drop in the CMB heat flux, but these drops can be large (>10 - 40%).

Reference

Roberts, J. H., R. J. Lillis, and M. Manga (2009), Giant impacts on early Mars and the cessation of the Martian dynamo, *J. Geophys. Res.* 114, EO4009, doi:10.1029/2008JE003287.

North America regional sea level since the Late Cretaceous from adjoint convection models

Sonja Spasojević, Lijun Liu, and Michael Gurnis, *Seismological Laboratory, California Institute of Technology*

We apply adjoint models of mantle convection to North America since the Late Cretaceous. The present-day mantle structure is constrained by seismic tomography, and the time-dependent evolution by plate motions and stratigraphic data (paleo shorelines, borehole tectonic subsidence and sediment isopachs). We use adjoint algorithm of Liu and Gurnis [2008] that was developed by modifying Version 2.0 of CitcomS that we obtained from CIG.

The dynamic topography low associated with subduction of the Farallon slab is localized in the western North America over Late Cretaceous [Spasojević et al., 2009], representing the primary factor controlling the widespread flooding observed in the Western Interior Seaway (Fig. 1), with eustasy playing a secondary role. As North America moves westward over the Farallon slab downwelling, the dynamic topography low sweeps eastward across the continent, contributing to subsequent uplift of the western U.S., tilting the interior of North America, and dynamic subsidence of the U.S. east coast during the Cenozoic [Spasojević et al., 2008]. The east coast of the United States is not stable, it has been experiencing continuous dynamic subsidence over the Cenozoic, coincident with overall eustatic fall, which explain the discrepancy between sea level derived for New Jersey coastal plain and global sea-level curves.

Imposed stratigraphic constraints require that the Farallon slab was flat during Late Cretaceous, with an extensive zone of shallow dipping subduction extending farther east and north by up to 1000 km than previously suggested.

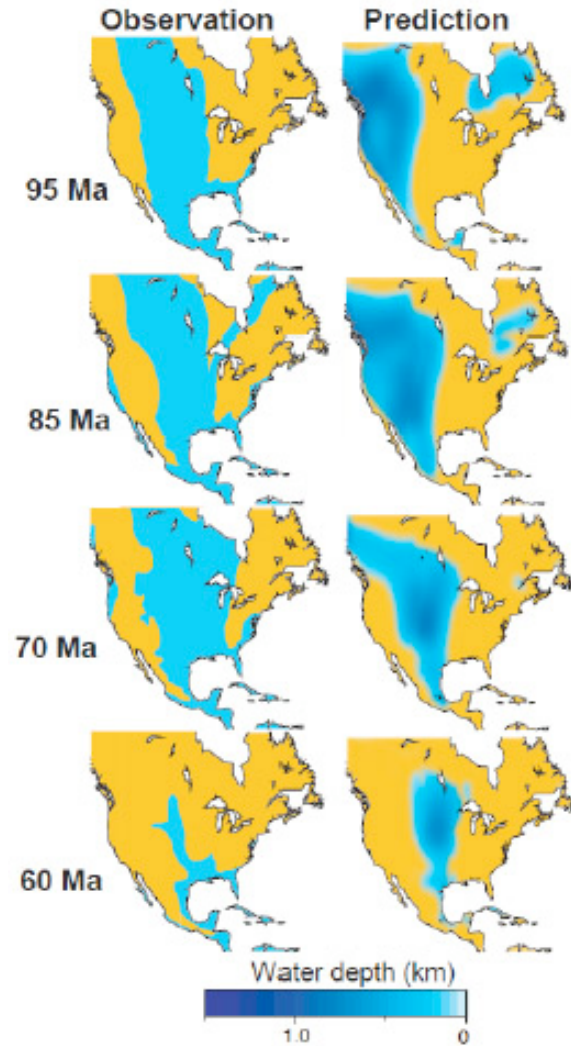


Figure 1. Comparison between observed and predicted flooding [Spasojević et al., 2009]

References

- Liu, L., and M. Gurnis (2008), Simultaneous inversion of mantle properties and initial conditions using an adjoint of mantle convection, *Journal of Geophysical Research*, 113, B08405, doi:10.1029/2008JB005594.
- Spasojević, S., L. Liu, M. Gurnis, and R. D. Müller (2008), The case for dynamic subsidence of the United States east coast since the Eocene, *Geophysical Research Letters*, 35, L08305, doi:10.1029/2008GL033511.
- Spasojević, S., L. Liu, and M. Gurnis (2009), Adjoint models of mantle convection with seismic, plate motion and stratigraphic constraints: North America since the Late Cretaceous, *Geochemistry, Geophysics, Geosystems* 10, Q05W02, doi:10.1029/2008GC002345, 24 pp.

Inference of mantle properties with an evolving dynamic model of the Antarctica-New Zealand region

Sonja Spasojević and Michael Gurnis, *Seismological Laboratory, California Institute of Technology, USA*
 Rupert Sutherland, *GNS Science, New Zealand*

We develop time-dependent mantle convection models of the Antarctica (ANT)-New Zealand (NZ) region constrained by plate motions from 80 Ma to present using global CitcomS Version 3.0. With a convection model, we interpreted anomalous NZ-ANT geophysical observations [Sutherland et al., 2009]: (1) ANT margin being 0.5-1.0 km shallower than the conjugate Campbell plateau; (2) Ross sea region geoid low (-60 m); (3) slow S-wave velocities in the upper and mid mantle and fast S-wave velocities in the lower mantle; (4) Campbell plateau 500-1000 m excess tectonic subsidence. Present day geoid and dynamic topography can be reproduced in a mantle convection model in which an upwelling rises above a cold downwelling, attributed to the last stage of the Gondwanaland subduction [Spasojević et al., 2009]. The mantle upwelling creates a dynamic topography high with maximum amplitude of 1 km, and results in a large present-day geoid low (Fig. 1). Our preferred model has a strong gradient in mantle viscosities with ratio of lower:upper mantle viscosities of 100:1 and with respect to an absolute viscosity of 1021 Pa s (Fig. 2). The excess subsidence of the Campbell plateau occurs as a result of northward drift of NZ away from a long-lived dynamic topography high created by the mantle upwelling.

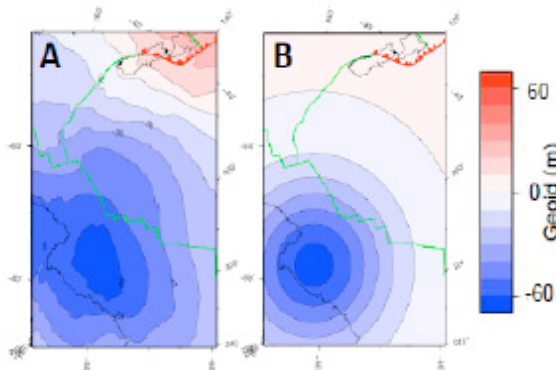


Figure 1. Comparison between observed (A) and predicted geoid at 0 Ma.

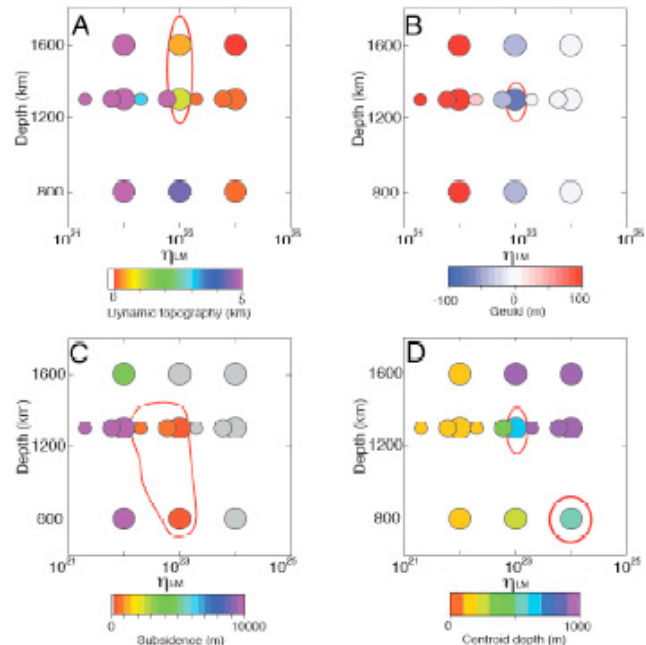


Figure 2. Constraining mantle viscosity (Pa s) and initial upwelling depth based on dynamic topography (A), geoid (B), borehole subsidence (C) and seismic tomography (D) as constraints. Red outlines indicate predictions that match observations.

References

- Spasojević, S., M. Gurnis, and R. Sutherland (2009), Inference of mantle properties with an evolving dynamic model of the Antarctica-New Zealand region, *Journal of Geophysical Research*, to be submitted.
- Sutherland, R., Spasojević, S., and M. Gurnis (2009), Mantle upwelling after Gondwana subduction death may explain anomalous topography of West Antarctica and subsidence history of eastern New Zealand, *Geology*, to be submitted.

The convection planform of a dense chemical layer with higher bulk modulus

Eh Tan¹, Wei Leng², Shijie Zhong², and Mike Gurnis¹

¹ Computational Infrastructure for Geodynamics, California Institute of Technology

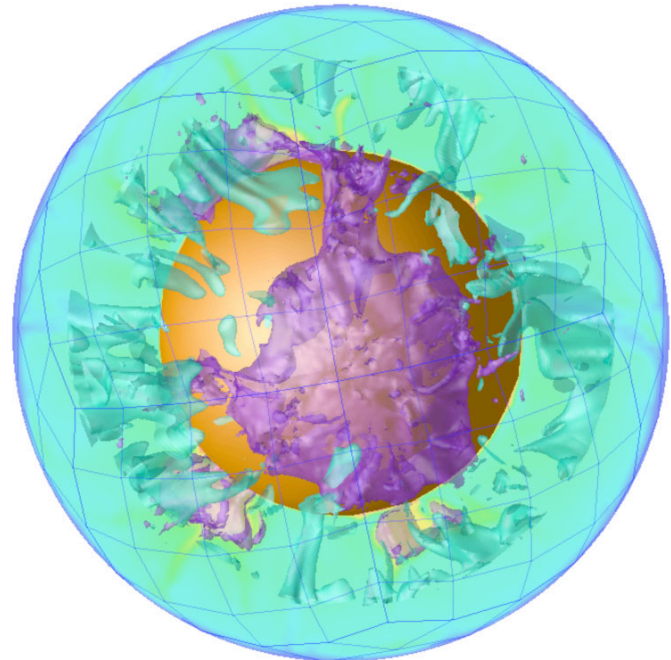
² Department of Physics, University of Colorado at Boulder

The two Large Low Velocity Provinces (LLVPs) in the base of lower mantle are the prominent features in all shear wave tomographic models. Their shear wave speed anomaly and bulk sound speed anomaly are anti-correlated. They form a degree-2 pattern, and their margins spatially coincide with the reconstruction of the eruption sites of Large Igneous Provinces of past 250 Myrs. This suggests that the LLVPs are not short-term transient, but long-term stable, chemical structures. Moreover, it appears that the LLVPs did not significantly shift around laterally over the past 250 Myrs.

The stability of dense chemical structures at the base of the mantle has been well studied. These studies concentrate on the vertical movement of the chemical structures. However, in this project, we will investigate the lateral movement of the chemical structures. We use CIG's CitcomS v3.0.3 with two modifications: a) the mesh is adjusted so that when tracer module is used, the mesh still can be partitioned in azimuthal direction; b) the chemical density anomaly is allowed to change radially to simulate the effect of the bulk modulus anomaly.

We found that with reasonable values of bulk modulus and chemical density anomalies, the chemical structures are dome-like and survive for hundreds of million years. Warm upwellings rise from the top and margins of the structures, while cold downwellings occur near the perimeter of the structures or where the structures are absent. The structures have a degree-2 pattern in most models, and degree-3 in a few models. This is likely controlled by the initial conditions. Nonetheless, the convection planform is always stable, in a sense that the location of upwellings and downwellings do not change much with time.

Figure (right) shows the chemical structures (purple) and the cold downwellings (cyan) in the lower mantle. The chemical structures stay roughly at the same location until gradually entrained.



Reference

Tan, E., W. Leng, S. Zhong, and M. Gurnis, The convection planform of a dense chemical layer with higher bulk modulus, *in preparation*.

Migration of Tharsis volcanism on Mars caused by differential rotation of the lithosphere

S.J. Zhong, *University of Colorado, Boulder*

The Tharsis Rise and crustal dichotomy are the two most important surface features on Mars. The crustal dichotomy is characterized by ~5 km elevation difference between the southern highlands and northern lowlands, and is the oldest geological feature on Mars. The Tharsis Rise is a vast volcanic construct in the equatorial region near the dichotomy boundary. Tharsis volcanism was initiated in the southern highlands and the main volcanic center had subsequently migrated to its current location, suggesting a relative motion between the lithosphere and the underlying mantle. However, Mars, a one-plate planet, cannot have large-scale horizontal motion of lithosphere, in the standard theory of stagnant-lid convection for one-plate planets.

Here I demonstrate that a unique mode of horizontal motion of lithosphere, differential rotation of lithosphere, is readily excited for Mars with an one-plume convection and lithospheric thickness variations. This mechanism explains the temporal and spatial patterns of Tharsis volcanisms and offers a path to a unified model for the Tharsis Rise and crustal dichotomy. This mechanism has implications for volcanisms, tectonics, and true polar wander (TPW) for one-plate planetary bodies. CitcomS is used for this project.

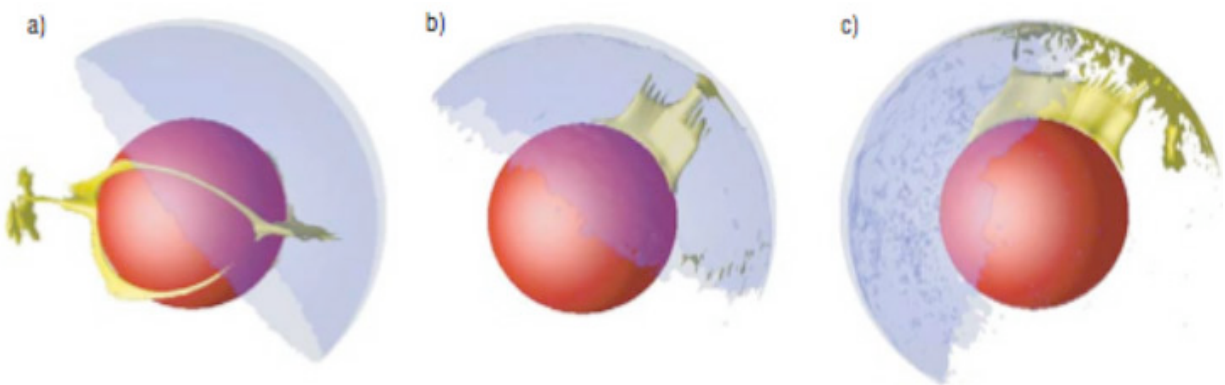


Figure: (a) Convection at an early stage before degree-1 convection is formed (the light blue isosurface represents a high viscosity melt residue cap), (b) one-plume structure forms under the cap, and (c) the lithospheric shell rotates above the one-plume structure such that the plume is finally stabilized near the cap boundary.

References

- Zhong, S.J. (2009), Migration of Tharsis volcanism on Mars caused by differential rotation of lithosphere, *Nature-Geoscience* 2, 19-23, doi:10.1038/NGEO392.
- Roberts, J.H. and S.J. Zhong (2006), Degree-1 convection in the Martian mantle and the origin of the hemispheric dichotomy, *J. Geophys. Res.*, 111, E06013, doi:10.1029/2005JE002668.

Constraints on thermochemical convection of the mantle from plume heat flux, plume excess temperature and upper mantle temperature

S.J. Zhong and W. Leng, *University of Colorado, Boulder*

This study seeks to constrain the layered mantle model from observed plume excess temperature, plume heat flux, and upper mantle temperature. 3-D spherical models of whole-mantle and layered mantle convection are computed for different Rayleigh number, internal heat generation, buoyancy number, and bottom layer thickness for layered mantle models. The model results show that these observations are controlled by internal heating rate in the layer overlying the thermal boundary layer from which mantle plumes are originated. To reproduce the observations, internal heating rate needs $\sim 65\%$ for whole-mantle convection, but for layered mantle models, the internal heating rate for the top layer is $\sim 60\%$ for averaged bottom layer thicknesses $< \sim 1100$ km. The heat flux at the core-mantle boundary (CMB) is constrained to be ~ 12.6 TW for whole-mantle convection. For layered mantle, an upper bound on the CMB heat flux is ~ 14.4 TW. For mantle secular cooling rate of ~ 80 K/Ga, the current study suggests that the top layer of a layered mantle is relatively thick (> 2520 km) and has radiogenic heat generation rate $> 2.82 \times 10^{-12}$ W/kg that is > 3 times of that for the depleted mantle source for MORB (DMM). For the top layer to have the radiogenic heat generation of the DMM, mantle secular cooling rate needs to exceed 145 K/Ga. The current study also shows that plume temperature in the upper mantle is about half of the CMB temperature for whole-mantle convection or ~ 0.6 of temperature at compositional boundary for a layered mantle, independent of internal heating rate and Rayleigh number. Finally, the model calculations confirm that mantle plumes accounts for the majority ($\sim 80\%$) of CMB heat flux in whole-mantle convection models. However, plume heat flux decreases significantly by as much as a factor of three, as plumes ascend through the mantle to the upper mantle, due to the adiabatic and possibly diffusive cooling of the plumes and due to slight (~ 180 K) subadiabaticity in mantle geotherm. *CitcomCU* is used for this project.

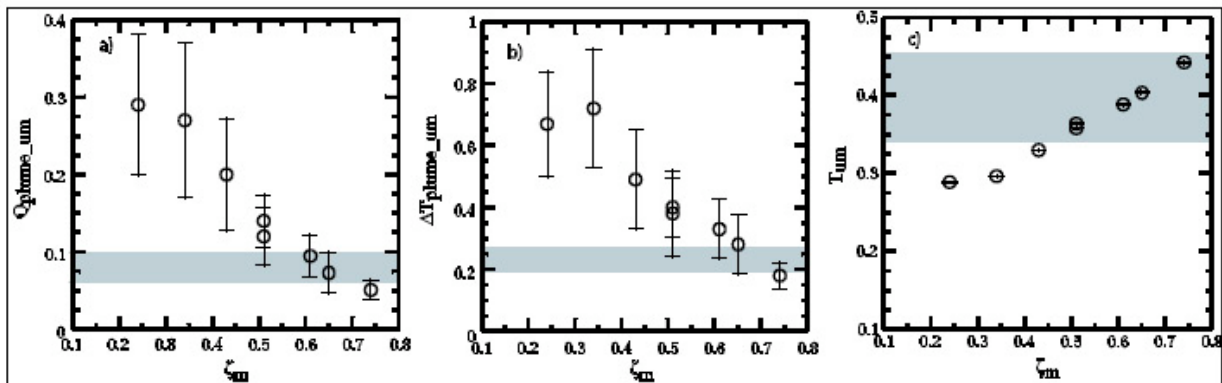


Figure: (a) Normalized plume heat flux, (b) plume excess temperature, and (c) upper mantle temperature versus internal heating rate. Shaded bars are for the ranges of observations.

References

- Zhong, S.J. (2006), Constraints on thermochemical convection of the mantle from plume heat flux, plume excess temperature and upper mantle temperature, *J. Geophys. Res.* *111*, B04409, doi:10.1029/2005JB003972.
- Leng, W. and S.J. Zhong (2008), Controls on plume heat flux and plume excess temperature, *J. Geophys. Res.* *113*, B04408, doi:10.1029/2007JB005155.

Very Long-wavelength Convection, True Polar Wander and Supercontinent Cycles

S.J. Zhong, *University of Colorado, Boulder, USA*

Z.X. Li, *Curtin University of Technology, Australia*

J.H. Roberts, *University of California, Santa Cruz, USA*

We show in this paper that mobile-lid mantle convection in a three-dimensional spherical shell with observationally constrained mantle viscosity structure, and realistic convective vigor and internal heating rate is characterized by either a spherical harmonic degree-1 planform with a major upwelling in one hemisphere and a major downwelling in the other hemisphere when continents are absent, or a degree-2 planform with two antipodal major upwellings when a supercontinent is present. We propose that due to modulation of continents, these two modes of mantle convection alternate within the Earth's mantle, causing the cyclic processes of assembly and breakup of supercontinents including Rodinia and Pangea in the last 1 Ga. Our model suggests that the largely degree-2 structure for the present-day mantle with the Africa and Pacific antipodal superplumes, is a natural consequence of this dynamic process of very long wavelength mantle convection interacting with supercontinent Pangea. Our model explains the basic features of true polar wander (TPW) events for Rodinia and Pangea including their equatorial locations and large variability of TPW inferred from paleomagnetic studies. Our model also suggests that TPW is expected to be more variable and large during supercontinent assembly, but small after a supercontinent acquires its equatorial location and during its subsequent dispersal. *CitcomS* is used in this project.

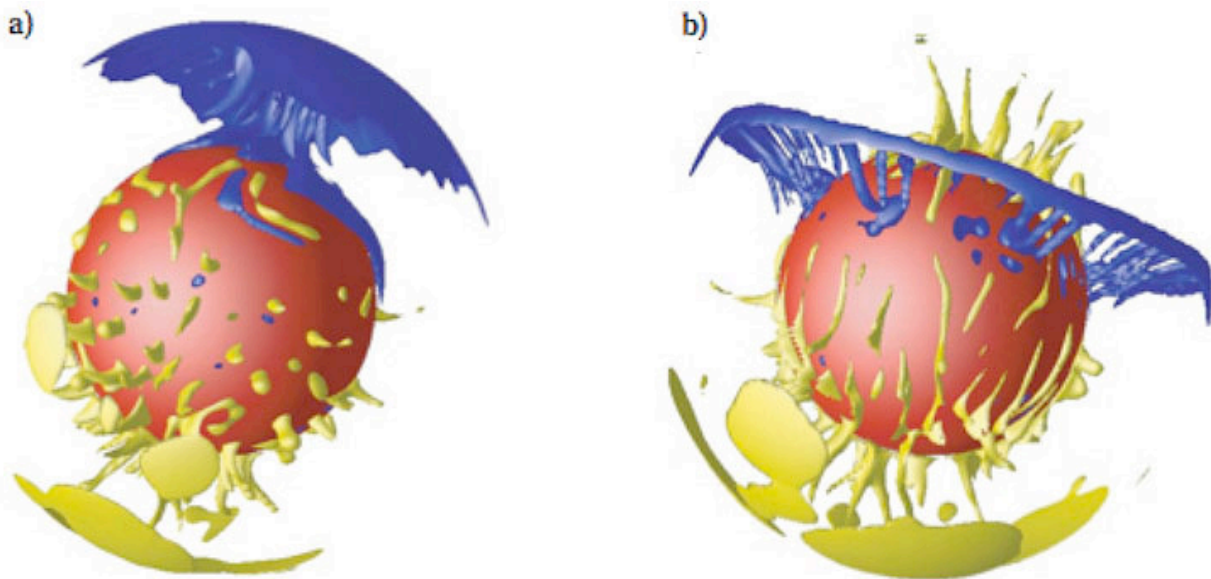


Figure: (a) Degree-1 convection with no continental blocks, and (b) Degree-2 convection with a supercontinent.

References

- Zhong, S.J., N. Zhang, Z.X. Li, and J.H. Roberts (2007), Supercontinent cycles, true polar wander, and very long-wavelength mantle convection, *Earth Planet. Sci. Lett.*, 261, 551-564.
- Zhang, N., S.J. Zhong, and A.K. McNamara, Supercontinent formation from stochastic collision and mantle convection models, *Gondwana Research* 15(3-4), 267-275, doi:10.1016/j.gr.2008.10.002.

Post-rifting relaxation at a subaerial spreading center

W. Roger Buck and Scott Nooner, *Lamont-Doherty Earth Observatory of Columbia University*

Most segments of spreading centers are difficult to study since they are deep under water. Iceland and the Afar are the two places on earth where spreading centers are subaerial. In September of 2005 a sequence of hundreds moderate-sized earthquakes in Afar was detected at Addis Ababa, Ethiopia. This marked the first major subaerial spreading center dike intrusion event of the space geodetic era. InSAR data indicated that the dike opened ~6m along a 60 km long line (Wright et al., 2006). Also, several meters of normal fault offset deepened a graben along the trace of the dike.

The uniqueness of this event has sparked major observational effort that includes deployments of seismometers and continuous GPS receivers. Since the first large event at least 8 more dike intrusion/propagation events have been detected. Results from GPS surveys indicate that the current horizontal surface motions greatly exceed the secular divergence rate of ~1.7 cm/yr.

The modeling of the viscoelastic deformation driven by the opening of dikes within the Dabbahu Segment of the Afar is being done jointly between Lamont-Doherty Earth Observatory and the Purdue University. At Lamont we have used *PyLith* to construct a 3D finite element model of the region to model viscoelastic relaxation of the crust following the on-going diking events.

Our model consists of an elastic layer over a Newtonian viscoelastic layer with an embedded dike made up of five finite length segments. The dike geometry and opening distributions were determined from InSAR by Wright et al. (2006). We varied both the thickness of the elastic layer and the viscosity of the of the viscoelastic layer to obtain the best fit to the observed surface deformation from GPS. Our best model has a 17 km thick elastic layer underlain by a viscoelastic layer with viscosity of 4×10^{18} Pas. The results of this work were presented at the AGU meeting in December 2008

(Bennati et al., 2008) and we have a paper in preparation (Nooner et al., in prep). Without the help of Charles Williams, one of the developers of *PyLith*, our work would have been far more time consuming.

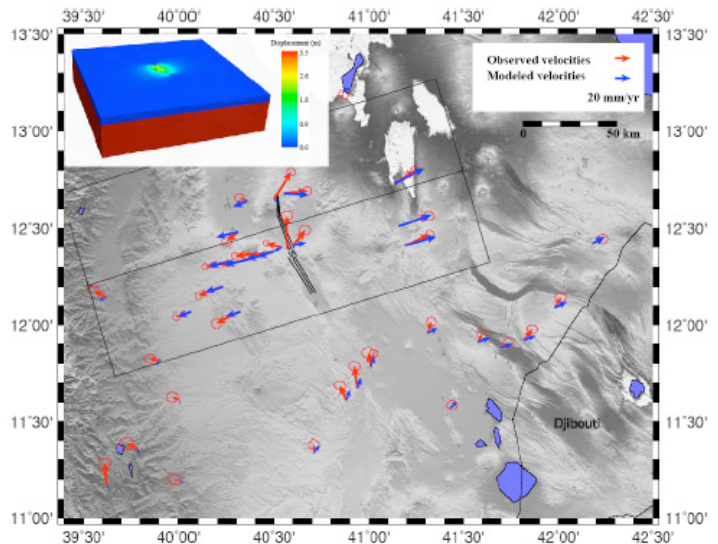


Figure: Insert shows model geometry of a 3D block with an elastic layer (blue) overlaying a visco-elastic lithosphere (red). Surface displacements (m) for the best fitting model to the September 2005 dike are shown on the surface expression of the mesh used to build the model. Map comparing model results and GPS observations.

References

- Bennati, L., Calais, E., Wright, T., Hamling, I., Lewi, E., Nooner, S., Buck, R., and Ebinger, C. (2008), *EosTrans. AGU*, 89 Fall Meet. Suppl., Abstract T43A-1981.
- Nooner, S. L., Bennati, L., Calais, E., Wright, T., Hamling, I., Buck, R., and Ebinger, C., in preparation.
- Wright, T. J., C. Ebinger, J. Biggs, A. Ayele, G. Yirgu, D. Keir, and A. Stork (2006), *Nature*, 442, 291-294.

Modeling of Coulomb Stress Changes During the 2002-2003 Etna Eruption

G. Currenti, C. Del Negro, and G. Ganci, *INGV-CT*
C. A. Williams, *GNS Science*

A fully 3D finite element simulation is performed to study the interaction between the magmatic intrusions and the fault systems that were reactivated during the 2002-2003 Etna eruption. We investigated how the topography and the complex medium heterogeneity can affect the ground deformation and the stress field solutions. The modeling is conducted using the CIG finite element code PyLith [Aagaard et al., 2008]. The computational domain was generated using a digital elevation model of Mt. Etna from the 90 m Shuttle Radar Topography Mission (SRTM) data and a bathymetry model from the GEBCO database (<http://www.gebco.net/>) using LaGriT (<http://lagrit.lanl.gov>). To simulate the magmatic intrusions we assigned tensile dislocation boundary conditions to the nodes lying on the dike surfaces. The elastic parameters were estimated using seismic velocity tomography.

Based on the Coulomb failure criterion, we resolved the stress changes, generated by the magmatic intrusions, onto the mapped structural trends of the Pernicana Fault (PFS, a local volcanic edifice feature on Etna), which was reactivated soon after the eruption onset. The presence of medium heterogeneity and topography strongly alter the amplitudes of the Coulomb stress changes with respect to homogeneous elastic half-space solutions (see Figure). Seismicity matches well the areas of positive increase in the static stress changes caused by the intrusive events along the southern and northeastern flanks [Currenti et al., 2008].

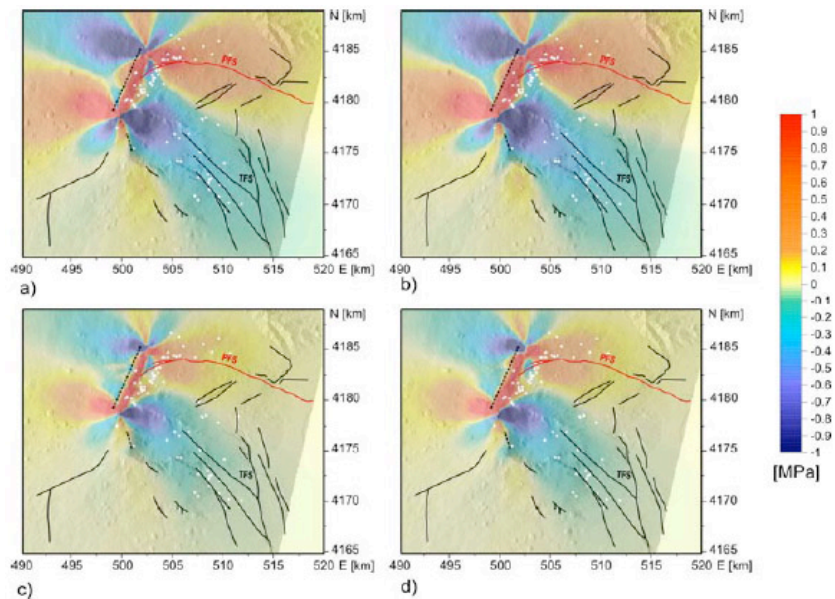


Figure: Map view of Coulomb stress changes generated by the magmatic intrusions (black dashed lines) resolved onto Pernicana Fault (red line). The fault is mapped by a vertical plane oriented 100°N with left lateral motion. For all the models HomFlat (a), HomTopo (b), HetFlat (c), HetTopo (d) a positive stress change area surrounds the Pernicana Fault and well matches the seismicity recorded from 27th to 29th October (white circles, from Barberi et al., 2004).

References

- Aagaard, B., S. Kientz, M. Knepley, L. Strand, and C. Williams (2008), *PyLith User Manual*, Version 1.3, Computational Infrastructure for Geodynamics.
URL:geodynamics.org/cig/software/short/pylith/pylith_book-1.3.pdf.
- Barberi G., Cocina O., Maiolino V., Musumeci C., Privitera E. (2004), Insight into Mt. Etna (Italy) kinematics during the 2002–2003 eruption as inferred from seismic stress and strain tensors. *Geophys. Res. Lett.*, 31, L21614, doi:10.1029/2004GL020918.
- Currenti, G., C. Del Negro, G. Ganci, and C. A. Williams (2008), Static stress changes induced by the magmatic intrusions during the 2002–2003 Etna eruption, *J. Geophys. Res.*, 113, B10206, doi:10.1029/2007JB005301.

Contemporary strain and stressing rates across Alaska from interseismic and postseismic processes

Andy Freed and Tabrez Ali, *Purdue*
Jeff Freymueller, *U. of Alaska, Fairbanks*

We are using a finite element model to calculate the contemporary evolution of stress in Alaska in an effort to identify regions of highest seismic hazard. We are interested in identifying regions with the fastest current stressing rates and regions of highest unrelieved stress accumulated over the past century. To date we have developed a geologically and seismologically constrained 3-D viscoelastic finite element model of the region that incorporates the highly contorted subducting Pacific slab and all active upper plate fault systems (figure below). The mesh was developed using the Cubit mesh generator toolkit [cubit.sandia.gov], while all calculations are performed using the CIG finite element code PyLith [geodynamics.org/cig/software/packages/short/pylith]. We drive the Pacific slab kinematically (i.e. velocity boundary conditions at surface and depth) in accordance with its observed motion relative to North America in a manner that maintains its current convergent geometry. This enables us to study how properties of the plate interface (i.e. locked and/or sliding megathrust) and currents within the mantle wedge influence strain and stressing rates within the North American plate. In addition to interseismic convergence, we are also simulating all of the major earthquakes to have occurred over the past century to incorporate stress changes due to slip as well as the influence of postseismic relaxation of the mobile mantle on strain and stressing rates. We are currently calibrating the model to geodetic (GPS) constraints prior to the 2002 Denali earthquake. Our initial results indicate that significant strain rates occur a few hundred km inboard of the megathrust and must be due to weakness (e.g., lower effective viscosity) in the upper crust (distributed or due to low angle faults at depth we cannot yet say). In addition, we find that currently measured southward velocities (anomalous since the Pacific plate drives northward) that extend more than 500 km inland in some locals, are consistent with continued ongoing postseismic relaxation associated with the great M9.2 1964 Alaska earthquake. That postseismic responses are so long-lived is a testament to their overall importance in the evolution of the stress field through the earthquake cycle.

Our research has benefited greatly by the accessibility of PyLith's developers, who willingly help us work through solver problems (mostly user caused, sometimes code bugs) and are being very responsive to our need for the code to expand its capabilities, especially more complex rheologies, cohesive elements. The accessibility and expertise of the developers has been key to our continual progress on this project and will serve to make PyLith more versatile in the future.

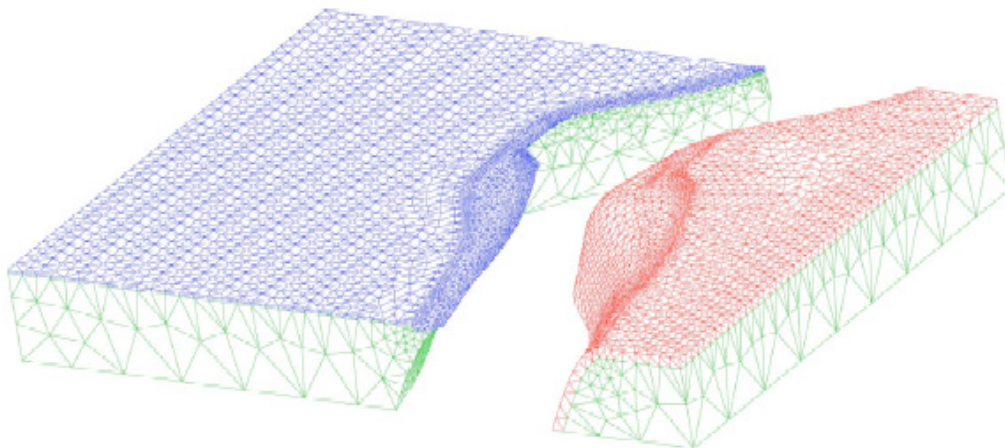


Figure: Finite element mesh of Pacific plate subducting beneath North America

3-D FEM derived elastic Green's functions for the coseismic deformation of the 2005 M_w 8.7 Nias-Simeulue, Sumatra earthquake

Ya-Ju Hsu, *IESAS, Taiwan*; Mark Simons, *Caltech, USA*; Charles Williams, *GNS Science, New Zealand*; Emanuele Casarotti, *INGV, Italy*

We use the finite element code PyLith and a 3-D mesh to evaluate the impact of topography, Poisson's ratio, and 3-D elastic structure on coseismic slip distributions and surface displacements of the 2005 M_w 8.6 Nias-Simeulue, Sumatra earthquake. The effect of topography on surface displacements is significant when the rupture location and the topography are in phase or the rupture occurs at shallow depth. Surface displacements are not very sensitive to perturbations of Poisson's ratio in substrata. The 3-D elastic structure is the most influential parameter in the FEM. We also investigate coseismic slip models of the 2005 earthquake using different combinations of fault geometries and material properties. Deformation zones are narrower in all tested 3-D elastic models compared to those within a half-space model independent of fault geometries. The fit to an elastic half-space model is generally better than a 3-D elastic model. Although the fit to surface observations in our 3-D elastic model is not better than the result from a simple half-space model, the resulting slip distribution may reflect the true fault slip behavior with more fidelity. The remaining misfit may imply that there are other mechanisms taking place during earthquake rupture that have not been well understood at subduction zones.

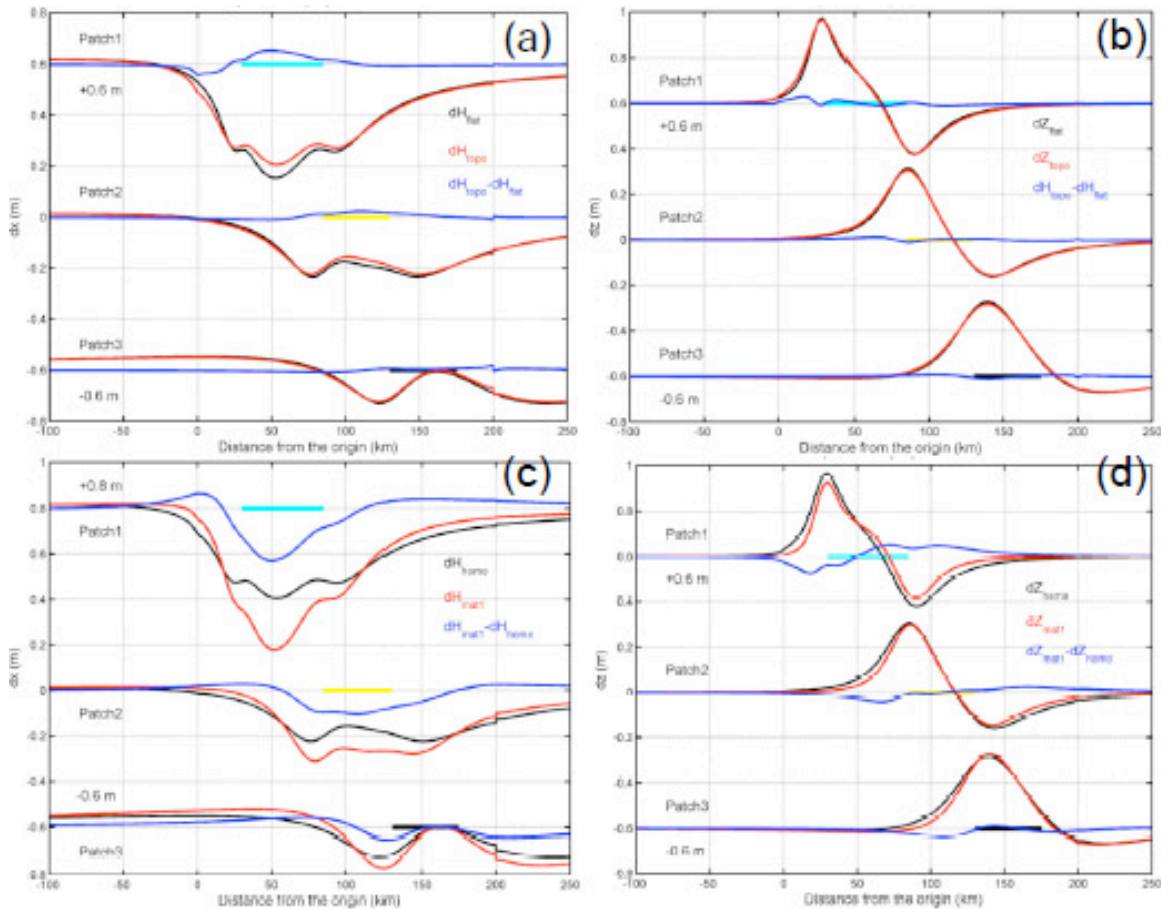


Figure 1: The profiles of surface displacements perpendicular to the trench (the origin) from 3 rupture sources (Cyan, yellow, and black lines indicate rupture locations). The black numbers in the panels show the offsets of displacements. (a) Vertical displacements from a flat earth model (black) and a real surface relief model (red) and the differences (blue) between these two models; (b) Similar to (a) but for vertical displacements; (c) Surface displacements orthogonal to the trench estimated from homogeneous (black) and heterogeneous (red) models and the difference between them (blue); (d) Similar to (c) but for vertical displacements.

Assessing the effects of rigidity contrasts on earthquake source inversions using PyLith

Rowena Lohman, *Cornell University, USA*
 Charles Williams, *GNS Science, New Zealand*

Current methods of inverting geodetic data for coseismic fault slip generally rely on simple elastic half space or layered space models to describe the crustal response to dislocations on a given fault plane. The neglect of the 3D variations in rigidity that exist within the real Earth can bias inversion results, whether the goal is determining the optimal fault plane geometry associated with a particular event or to find the best-fitting co-seismic slip distribution. For many tectonically active areas, such as Southern California, sophisticated models of crustal elastic moduli are available. However, inversions using the full 3D elastic structure are very computationally expensive and not always necessary.

In this project, we are working towards generating quick tests that can identify cases where neglecting elastic structure is appropriate. First order goals in inversions of geodetic data may include determining the location and orientation of the fault plane and the earthquake magnitude, perhaps in near real-time for use in disaster response efforts. Other possible targets include the study of the interaction between seismicity and Coulomb stress changes or earthquake triggering through stress transfer from the lower crust. In all cases, it is essential to know how confident we can be about the conclusions we draw from the data, requiring that we assess not only the contribution from data error, but also from errors in the models we use in inversions.

To assess the effects of rigidity contrasts with various characteristics, we use *PyLith* to generate synthetic data for earthquakes within a range of realistic crustal rigidity structures such as a cross fault contrast. Inversion of these synthetic data sets for the best fitting size and orientation of dislocation within an elastic half space allows us to place bounds on the magnitude of bias introduced when using simple elastic half space models.

In regions where we have limited access to information about elastic structure, the results of this study can aid researchers in placing error bounds on their results, or in determining whether particular problems

are feasible. In areas with existing velocity structure models, the target problem may require the use of sophisticated inversion schemes that ingest all the existing knowledge, instead of relying on simpler, computationally inexpensive inversions within elastic half spaces.

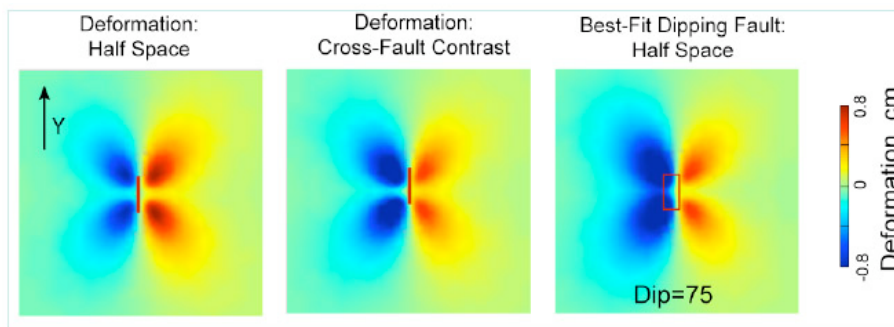
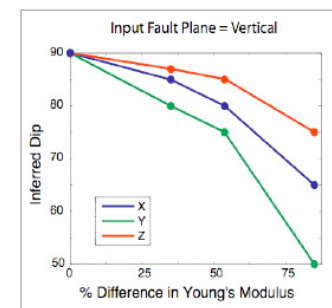


Figure 1 (above): *Y*-component of deformation expected for a vertical strike slip fault in a half space (left), and with the inclusion of a cross-fault contrast (middle, deformation field generated with PyLith). Right panel illustrates how the best-fit fault in a half space must include a dip of 75 degrees in order to match the asymmetric deformation field resulting from the cross-fault contrast.

Figure 2 (right): *Inferred dip vs. cross-fault contrast in Young's modulus, for a vertical input fault plane such as the one described in Figure 1. Lines indicate the result of inversions using the X, Y, or Z component of deformation. As expected, we retrieve the input geometry (dip=90) for all cases where the crossfault contrast is zero.*



Effects of 3-D Variations in Fault Geometry and Elastic Structure on Geodetic Velocities, Ventura Basin Region, California

Jiangning Lü, *MIT*; Carl W. Gable, *Los Alamos National Lab*; Charles A. Williams, *GNS Science, New Zealand*; Bradford H. Hager, *MIT*

Geodetic observations of interseismic elastic strain accumulation and coseismic strain release are sensitive to the heterogeneous rheology of the lithosphere. Even though models assuming simple rheology might fit observed geodetic velocities well, conclusions about fault behavior could be biased if lateral and vertical variations of the lithosphere's mechanical properties are not accounted for. We are developing 3-D Crustal Deformation Models (CDM) of southern California using the Finite Element Method (FEM), accounting for realistic fault geometries provided by the SCEC Community Fault Model (CFM) and 3-D variable elastic properties provided by the SCEC Community Velocity Models (CVM). We are using the mesh generation package LaGriT [meshing.lanl.gov] to create the meshes. To perform the modeling itself, we are using PyLith [Aagaard et al., 2008]. The model we present here encompasses the region around the Ventura Basin, including the San Cayetano, Oak Ridge and Santa Susana faults.

We perform three different calculations of coseismic displacements of the Ventura Basin model: 1) analytic models using the rectangular dislocation based (CFM-R) fault geometry assuming homogeneous elastic properties [Meade and Hager, 2005]; 2) FEM models using our meshing of the T-surf based CFM assuming homogeneous elastic properties; 3) FEM models using our meshing of the CFM including elastic structure from the latest CVM-H. We also explore different boundary conditions by assuming a) fixed, b) free and c) displacements computed from analytical models. By comparing model results, we find that both realistic fault geometry and inhomogeneous elastic structure have significant effects on the surface displacements. The effects of differing fault geometry can reach surprisingly far from the faults in certain places; the CFM-R fault model does not always provide a good representation of the CFM. The effects of the inhomogeneous elastic structure on surface displacements are substantial in a much broader region and the inhomogeneous model shows more concentrated deformation across the basin. Incorporating the variations of elastic properties and fault geometry, coseismic displacements can differ on the order of 30~40% in the near field, and the azimuth can differ by as much as 90 degrees. We conclude that ignoring realistic variations in fault geometry by using rectangular dislocations and ignoring 3-D elastic structure can lead to large errors in calculations of coseismic and interseismic displacements.

References

- Aagaard, B., S. Kientz, M. Knepley, L. Strand, and C. Williams (2008), *PyLith User Manual*, Version 1.3.1, Computational Infrastructure for Geodynamics.
- Meade, B. J., and B. H. Hager (2005), Block models of crustal motion in southern California constrained by GPS measurements, *J. Geophys. Res.*, *110*, B03403, doi:10.1029/2004JB003209.

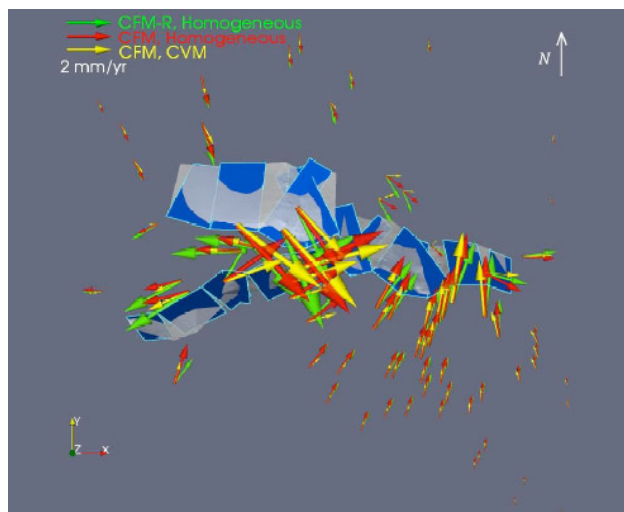


Figure. Map view of Comparison of coseismic surface displacements from models assuming different versions of fault geometry and elastic structure. Green: simplified rectangular fault geometry (CFM-R) and homogeneous elastic structure; Red: realistic fault geometry (CFM) and homogeneous elastic structure; Yellow: realistic fault geometry (CFM) and elastic structure with 3-D variations (CVM).

Viscoelastic Modeling of Ground Deformation During the 1993-97 Inflation Period at Etna Volcano

D. Scandura, *Università di Catania*
 G. Currenti and C. Del Negro, *INGV-CT*

We reviewed the ground deformation observed on Etna volcano during the 1993-1997 inflation period by setting up a 3D viscoelastic model. Since 1993 different geodetic measurements (EDM, GPS, SAR and leveling data) identified an inflationary phase characterized by a uniform and continuous expansion of the overall volcano edifice that was not perturbed by eruptive activity. We used the CIG finite element code *PyLith* for modeling time-dependent ground deformation due to volcanic pressure sources embedded in a viscoelastic medium. Especially in volcanic areas, the presence of heterogeneous materials and high temperatures produce a lower effective viscosity of the Earth's crust that calls for considering the thermal regime of crustal volume surrounding the magmatic sources. We implemented a viscoelastic shell model in which the magmatic source is embedded in an elastic medium and surrounded by a concentric shell of viscoelastic material. It is reasonable to assume that rocks near the inflation source are considerably heated and weakened beyond the brittle-ductile transition temperature, where viscoelastic rheology is more appropriate to describe the mechanical behavior of the surrounding rocks. The computational domain was generated using a digital elevation model of Mt Etna (SRTM data) and a bathymetry model for the off-shore area (GEBCO database from <http://www.gebco.net/>) using LaGriT (<http://lagrit.lanl.gov>). To simulate the magmatic inflation we assigned the pressure value on the magmatic source wall. Non-uniform distributions of the Young's modulus and Poisson ratio were estimated using seismic velocity tomography. A viscosity of 10^{16} Pas was assumed for the viscoelastic shell using the generalized Maxwell model. The model permits to evidence that viscoelastic relaxation is responsible for significant time-dependent variations in long-term deformation. The inclusion of the viscoelastic shell enhances the estimates of the deformation field expected at the ground surface over time (Figure). Therefore, the numerical model, including viscoelastic material around the magmatic source, enables to produce deformation comparable with those obtained from elastic model, requiring a significantly lower pressure (Del Negro et al., 2009).

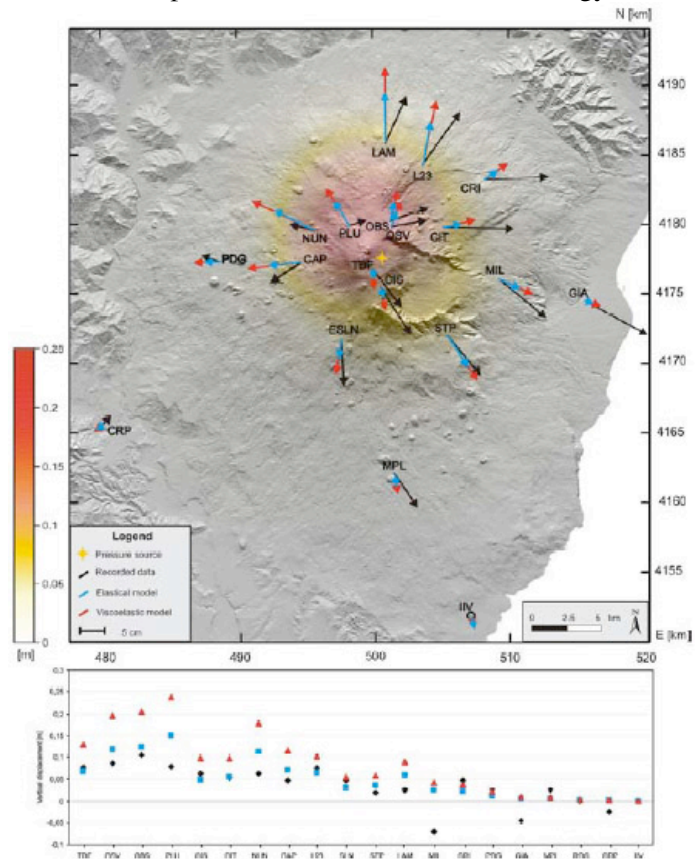


Figure: Comparison between the elastic and viscoelastic solution evaluated 3.5 years later the pressure change occurred.

References

Del Negro, C., G., Currenti, D. Scandura (2009), Temperature-dependent viscoelastic modeling of ground deformation: application to Etna volcano during the 1993-1997 inflation period, *Physics of the Earth and Planetary Interiors*, 172, 3-4, 299-309.

Modeling of Multiple Earthquake Cycles in Southern California Using the SCEC Community Fault Model

Charles A. Williams, *GNS Science, New Zealand*; Carl W. Gable, *Los Alamos National Lab*; Bradford H. Hager, *MIT*; Brendan J. Meade, *Harvard*; Brad Aagaard, *USGS*; Matt Knepley, *Argonne National Lab*

We are using the CIG finite element code *PyLith* [Aagaard et al., 2008] to investigate the effects of various rheologies on the predicted deformation field for models of multiple earthquake cycles in southern California. Our present models include 55 of the faults defined by the SCEC Community Fault Model (CFM). We use the LaGriT meshing package [meshing.lanl.gov] to mesh the complex geometry provided by the CFM, and we then run the models through several thousand years of simulated earthquakes. We use rotation poles determined from the block model of Meade and Hager [2005] to provide coseismic slip

distributions and velocity boundary conditions for the external boundaries of the mesh. In our initial models, we investigate the effects of variations in elastic properties by using the properties defined by the SCEC Community Velocity Model (CVM-H), and we also consider the effects of viscoelastic behavior using both a standard Maxwell model and a generalized Maxwell model (two or more Maxwell models in parallel). All of these effects significantly alter the predicted deformation field compared to a homogeneous elastic model (see Figure).

Our present models use regular recurrence times for each fault segment. We plan to use this same method to ‘spin up’ our models, and then to include known earthquake sequences. This will allow us to determine which set of properties yields results most consistent with geodetic observations.

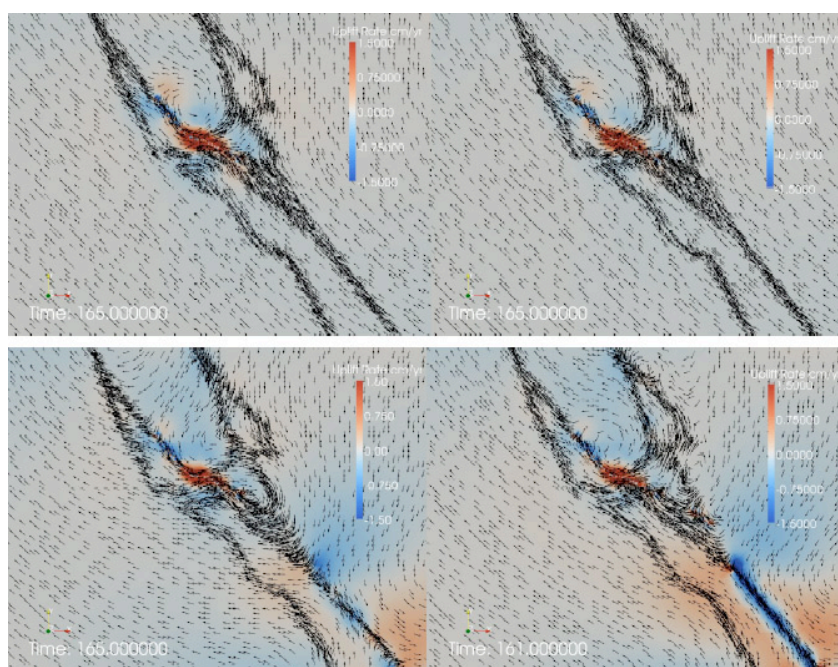


Figure. Predicted surface deformation fields for a 10-year time interval covering a simulated 1857 earthquake. Top left: Homogeneous elastic model. Top right: Elastic model using properties from CVM-H. Bottom left: Maxwell model using CVM-H properties and viscosities of 10^{20} and 10^{19} Pa-s above and below 15 km depth, respectively. Bottom right: Generalized Maxwell model using viscosity pairs of $(10^{20}, 10^{19})$ and $(10^{19}, 10^{18})$ Pa-s above and below 15 km, respectively.

References

- Aagaard, B., S. Kientz, M. Knepley, L. Strand, and C. Williams (2008), *PyLith User Manual*, Version 1.3, Computational Infrastructure for Geodynamics, URL: geodynamics.org/cig/software/short/pylith/pylith_book-1.3.pdf
- Meade, B. J. and B. H. Hager (2005), Block models of crustal motion in southern California constrained by GPS measurements, *J. Geophys. Res.* 110, B03403, doi:10.1029/2004JB003209.